GROWTH AND CHARACTERIZATION OF ZnO NANOWIRES AND THIN FILMS

By

YOUNG-WOO HEO

A DISSERTATION PRESENTED TO THE GRADUATE SCHOOL
OF THE UNIVERSITY OF FLORIDA IN PARTIAL FULFILLMENT
OF THE REQUIREMENTS FOR THE DEGREE OF
DOCTOR OF PHILOSOPHY

UNIVERSITY OF FLORIDA

2003

This dissertation is dedicated to my wife, Sookyung Lee.

Abstract of Dissertation Presented to the Graduate School
of the University of Florida in Partial Fulfillment of the
Requirements for the Degree of Doctor of Philosophy

GROWTH AND CHARACTERIZATION OF ZnO NANOWIRES AND THIN FILMS

By

Young-Woo Heo

December 2003

Chairman: David P. Norton
Major Department: Materials Science and Engineering

ZnO was studied in this dissertation for use in one-dimensional nanoscale devices,

optoelectronics, and electronic applications. The synthesis, structural, and optical

properties of ZnO and MgO nanowires as nanoscale materials were investigated. The

crystallinity, electrical, optical and magnetic properties of undoped and phosphorous

doped ZnO thin films for p-type ZnO were examined.

The ZnO nanowires were fabricated using catalyst-driven molecular beam epitaxy.

Site specific growth of ZnO and MgO nanowires was observed on Ag coated Si and

Al_2O_3 substrates. The structural and compositional studies indicated that the deposition of

Zn and Mg resulted in two different types of radial heterostructured (Zn,Mg)O nanowires.

One consists of a single crystal Zn-rich $Zn_{1-x}Mg_xO$ ($x < 0.02$) core having a hexagonal

wurtzite structure encased by an epitaxial $Zn_{1-y}Mg_yO$ ($y >> 0.02$) sheath having the same

hexagonal wurtzite structure. The other consists of single crystal ZnO with a hexagonal

wurtzite structure surrounded by a MgO sheath with a cubic rock salt structure.

The effect of phosphorus doping on the electrical and optical properties of ZnO grown via pulsed laser beam deposition was studied. Phosphorus doping yields enhanced *n*-type behavior in as-deposited films, indicating the formation of shallow donor states. Annealing in 100 mTorr of oxygen led to the conversion of n-type behavior in as-deposited films to semi-insulating behavior in the annealed films. For the annealed film, these results appear to reflect phosphorus substitution on the O sites.

The characteristics of device structures that employ phosphorus-doped (Zn,Mg)O have been examined in a effort to delineate the carrier type behavior in this material. The capacitance-voltage properties of metal/insulator/P-doped (Zn,Mg)O diode structures were measured and found to exhibit a polarity consistent with the P-doped (Zn,Mg)O layer being p-type. In addition, thin-film junctions comprising n-type ZnO and P-doped (Zn,Mg)O display asymmetric I-V characteristics that are consistent with the formation of a p-n junction at the interface. Although Hall measurements of the P-doped (Zn,Mg)O thin films yielded an indeterminate Hall sign due to a small carrier mobility, these results are consistent with previous reports that phosphorus can yield an acceptor state and p-type behavior in ZnO materials.

The photo-response of ZnO doped with phosphorus was investigated. A correlation between near band-edge emission and carrier density is observed. This is similar to results found for ZnO in which the carrier density is increased via annealing in a reducing ambient. Upon annealing in an oxidizing environment, the near band-edge emission decreased for both the undoped and phosphorus doped ZnO films. This was attributed to radiative transitions involving acceptor levels deep in the gap. The

phosphorus doping, combined with annealing, leads to an enhanced photoconductivity response.

The magnetic properties of phosphorus doped ZnO thin films were examined after high dose Mn implantation. Films show room temperature hysteresis in magnetization loops. The saturation magnetization and coercivity of the implanted single-phase films were both strong functions of the initial annealing temperature.

The ratio of the near band-edge (NBE) emission to the deep-level (DL) emission of the photoluminescence spectra is related to the Zn pressure during the growth of ZnO epitaxial thin films by molecular beam epitaxy. It is suggested that green deep-level emission comes from a donor-deep acceptor (Zn vacancy, V_{Zn}^{-}) transition, and yellow emission from a donor-deep acceptor (oxygen vacancy, O_i^{-}) transition. The shift of deep level emission results from different concentrations of Zn vacancy, V_{Zn}^{-} and oxygen vacancy, O_i^{-}.

CHAPTER 1
INTRODUCTION

Advanced materials and their related fabrication methods are essential steps in many fields of modern technology. The desirable properties of materials can be obtained by the control of dimension, size, morphology, microstructure, and composition of material, often achieved using synthesis methods. Nanowires and nanotubes are attracting considerable attention due to the opportunity to create nanoscale circuits. Conventional fabrication methods for computer chips will struggle to make devices at the nanoscale. Electronic circuits built from nanowires or nanotubes represent one way in which the miniaturization trend could continue. Key issues in nanowire technology for the realization of integration include how to synthesize and assemble. The control of the morphology, structure, composition, and size of nanowires is a basic step for their application, and should be achieved by a robust growth method. Selective growth of nanowires on a specific site can improve the ability to assemble and integrate them in nanoscale devices. The growth of heterostructured nanowires can give additional functionalities.

ZnO, a direct wide bandgap semiconductor, is attracting attention for use in light emitting diodes (LEDs), laser diodes (LDs), light detectors in the blue-UV wavelength region, gas sensors, and window material for flat panel displays and solar cell. Its transparency makes ZnO viable for use in transparent electronic devices [1-5]. However, p-type ZnO is a bottleneck for p-n junction applications with ZnO. ZnO is naturally an n-

type semiconductor because of deviations from stoichiometry due to the presence of intrinsic defects such as O vacancies (V_O) and Zn interstitials (Zn_i). Understanding the relationship between the properties of undoped ZnO and growth condition should help to achieve the growth of p-type ZnO. Recently, research has focused on nitrogen doping in ZnO epitaxial films for p-type. Until now, attempted p-type doping with nitrogen has yielded low hole carrier density with challenges in reproducibility [6-11]. Phosphorus is another possible dopant for the growth of p-type ZnO. Recently, significant interest has emerged in achieving magnetic functionality in semiconducting materials, including ZnO. Transition-metal-doped ZnO has been investigated as a promising dilute magnetic semiconductor for implementing spintronic device concepts.

The purpose of this research is to better understand and exploit the structural, electrical, optical, and magnetic properties of ZnO nanowires and thin films. A review of the literature is presented in Chapter 2 that describes the general properties of ZnO, the growth mechanisms and synthesis methods of nanowires, including ZnO nanowires, and the doping behavior in ZnO. The selective growth of ZnO nanowires via catalysis-driven molecular beam epitaxy is described in Chapter 3. The structural and compositional changes of (Zn,Mg)O nanowires as a function of Zn and Mg flux are discussed in Chapter 4. The effect of phosphorous on the electrical and optical properties of ZnO thin film for p-type is investigated using pulsed laser deposition in Chapter 5. Also, the magnetic properties of phosphorus doped ZnO were examined after high dose Mn implantation. In chapter 6, the relationships between growth condition and structural, electrical and optical properties of undoped ZnO thin film using molecular beam epitaxy with different oxygen sources are explored. Finally, a summary of the dissertation is given in Chapter 7.

CHAPTER 2
LITERATURE REVIEW

2.1 General Properties of ZnO

Zinc oxide (ZnO) exhibits many interesting properties, including anisotropy in crystal structure, nonstoichiometric defect structures, wide bandgap, optical transparency in the visible region, high refractive indices, large piezoelectric constants, and nonlinear optical coefficients [12]. It has been used for acoustic wave devices, varistors, gas sensors, and piezoelectric transducers [13-17]. In recent years, a significant amount of attention has been paid to ZnO as a wide bandgap semiconductor and transparent conducting oxide for LEDs, LDs, transparent electrodes, window material for solar cells, and transparent thin film transistors [3-5].

2.1.1 Wide Bandgap Semiconductors

Figure 2-1 below shows the variation of bandgap energy as a function of the lattice constant for the most common III-V and II-VI compound semiconductors. GaN, AlN, InN, GaAs, InAs, and AlAs are classified as III-V compound semiconductors. ZnO is one of the II-VI semiconductors that includes ZnS, ZnSe, CdSe, ZnTe, and CdTe. The bandgap and lattice constant of ZnO is similar to that of GaN as shown in Figure 2-1. The properties of ZnO are compared to other compound semiconductors in Table 2-1. ZnO is a direct bandgap (3.37eV) semiconductor having a large exciton binding energy of 60 meV. This is potentially useful for efficient UV laser application and low power
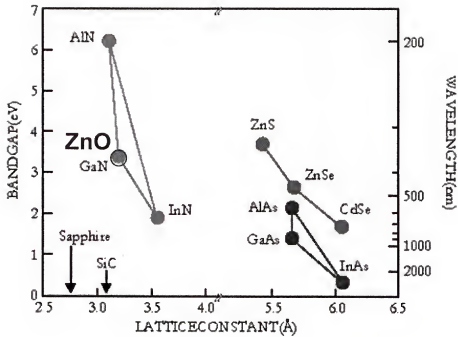
Fig. 2-1 the variation of bandgap energy as a function of the lattice constant for most common III-V and II-VI compound semiconductors.

Table 2-1 properties of compound semiconductors [18]

	ZnO	GaN	GaAs	ZnSe	ZnS
Bandgap (eV)	3.37	3.4	1.4	2.82	3.68
	Direct	Direct	Direct	Direct	Direct
Exciton Binding E (meV)	60	25	7.5	22	40
Electron hall mobility $(cm^2/V \cdot s)$	200	1000	8500	500	165
Hole hall mobility $(cm^2/V \cdot s)$	<5	30	400	30	5
Thermal conductivity (W/cm)	0.6	1.5	0.5	0.18	….
Melting Point (°C)	1975	>1400	1237	1100	1850

thresholds for pumping at room temperature. One promise of wide band-gap materials in electronics is that of enabling high temperature and high power devices. High temperature operation requires a wide bandgap so that the intrinsic carrier concentration remains. Intrinsic carrier concentrations on the order of $10^{15} cm^{-3}$ occur at 500 °C for gallium arsenide (E_g= 1.4 eV) and a 1000 °C for wide band-gap semiconductors such as gallium nitride (E_g= 3.4 eV) and ZnO [19]. High power operation is attractive for the wide bandgap semiconductors due to the one order of magnitude higher breakdown fields as compared to Si or GaAs. In optics, wide band-gap semiconductors are attractive for the development of blue and ultraviolet light emitting diodes and lasers.

2.1.2 Transparent Conducting Oxides

Most oxides, such as Al_2O_3, MgO, and glasses, that are optically transparent in the UV or visible range, are electrically insulating and are used for insulators, dielectrics, and optical materials. However, there are some oxides with a wide bandgap that are electrically conductive and transparent. These transparent conducting oxides(TCO) are used for transparent electrodes for solar cells and flat panel display, transparent thin film field-effect transistors(FETs), transparent p-n junction devices, low-emissivity windows in building, defrosting windows, and touch-panel control panels.[4, 5, 20-22]

Transparent conducting oxides can be classified as n-type and p-type semiconductors. Typical n-type transparent conducting oxides include ZnO, CdO, In_2O_3, SnO_2, Ga_2O_3, and relate ternaries and quaternaries oxides including Cd_2SnO_4, $CdIn_2O_4$, $GaInO_3$, $Zn_2In_2O_5$, $ZnSnO_3$, $Zn_{0.66}In_2O_{2.66}$, $Zn_2In_4Sn_3O_{14}$, $In_{1.88}Ga_{0.12}O_3$, and $In_{30}Ga_{1.5}Sn_{15}O_x$. Figure 2-2 illustrates the solid solution phase space. Their properties

can be controlled by electron doping and fabrication condition. Physical, chemical, and thermal durability, etchability, conductivity, plasma wavelength, work function, deposition temperature, uniformity, toxicity, and cost are important factors when choosing a transparent conducting oxide for any particular application. Indium tin oxide (ITO) is extensively used for transparent electrodes in flat panel displays and solar cells because of its high conductivity (0.9×10^4 S·cm^{-1}) and good optical transparency. However, due to the limitations of ITO, such as cost and degradation in hydrogen plasmas, the development of new n-type TCO materials is needed. A promising alternative is n-type ZnO doped with dopants such as In, Al, and F because of low cost, non-toxicity, high band gap, ease of doping and excellent durability under hydrogen atmosphere. Table 2-2 summarizes the electrical properties of ZnO.
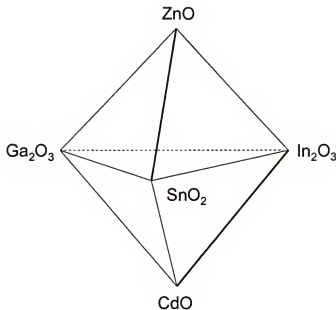
Fig. 2-2 Phase space of transparent conducting oxides.

For transparent p-n junction devices, $CuAlO_2$, $CuGaO_2$, $SrCu_2O_2$, and $AgInO_2$ have been investigated as p-type TCO materials. Near-UV emitting diodes based on a transparent p-n heterojunction composed of p-type $SrCu_2O_2$ and n-type ZnO was reported [20]. Recently, intensive research is focusing on p-type ZnO to achieve transparent p-n homojunction because of the excellent promise for UV optoelectronic devices as discussed in previous section.

2.1.3 Crystal Structure

ZnO has a hexagonal wurtzite structure with a = 3.25 Å and c= 5.12Å. The chemical bonds in ZnO with a wurtzite structure are largely ionic in nature because of a significant difference in the electronegativity between Zn (1.65) and O (3.44). The ionic radius of the Zn^{+2} ion is 0.60 angstroms and that of the oxygen ion is 1.40 angstroms. The ratio of radii for the cation and anion is thus $r_c/r_a = 0.60/1.40 = 0.428$. The Zn^{+2} ions occupy tetrahedral holes. The oxygen ions form a hexagonal closest-packed structure. The
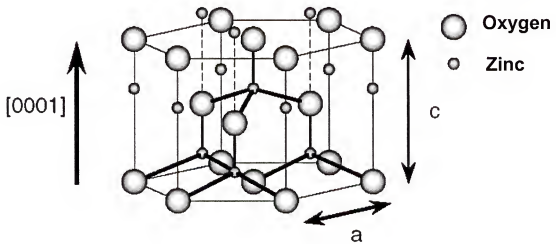
Figure 2-3 Hexagonal wurtzite structure of ZnO.

ionic solid is electrically neutral, and the unit cell itself must also be electrically neutral. With a hexagonal closest-packed structure of oxygen ions, there are two oxygen ions in the unit cell. Consequently there must also be two Zn^{+2} ions in the unit cell. Figure 2-3 shows the ZnO wurtzite structure. The large spheres represent the oxide ions, and the small spheres represent the Zn^{+2} ions.

2.1.4 Epitaxial Thin Film

Epitaxial ZnO films have been grown on c-plane sapphire using a number of techniques. ZnO thin films show intrinsically n-type properties, as native shallow donors are dominant over native acceptors. This will be discussed later. The (0001) surface of ZnO grown on c-plane sapphire is stable at all growth temperatures because of the oxygen sublattice. ZnO has the same six-fold symmetry as sapphire and, hence, there is always a preference of c-axis oriented ZnO film growth [23]. An epitaxially grown ZnO film on c-plane sapphire has a $(0001) \| (0001)$ and $[10\bar{1}0] \| [11\bar{2}0]$ orientational relationship between them. The polar (0001) faces of ZnO are assumed to have the lowest surface free energy and therefore [0001] is the preferred growth orientation. However, polycrystalline ZnO films grown on most substrates are oriented to c-axis, but with no specific in-plane orientation relationship with the substrate [24]. Epitaxially grown films have a higher mobility than polycrystalline films due to a lack of grain boundary scattering. Sapphire is often used for the growth of epitaxial ZnO. However, there is a large in-plane lattice mismatch (18%) between the ZnO ($a = 3.250$Å, $c = 5.213$ Å) and the underlying c-plane sapphire ($a = 4.754$Å, $c = 12.99$ Å). The lattice mismatch

between ZnO and sapphire induces defects, such as dislocations and other interface defects that reduce the carrier mobility.

The total electron mobility, μ_{total}, in ZnO is given by

$$\frac{1}{\mu_{total}} = \sum_i \frac{1}{\mu_i} \approx \frac{1}{\mu_{pop}} + \frac{1}{\mu_{acp}} + \frac{1}{\mu_{iis}}$$

where μ_{pop} is the electron mobility due to polar optical phonon scattering, μ_{acp} is that due to acoustic phonon scattering, and μ_{iis} is that due to ionized impurity scattering as given by the Brooks-Herring approximation [25]. The solid line in Fig.4 indicates the
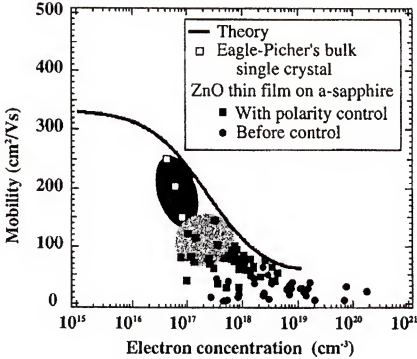
Fig.2-4 Calculated values for electron mobility in ZnO that can serve as a guideline for future improvements in ZnO electrical properties. The electrical properties of Eagle-Picher's bulk single crystals are shown as open squares and K. Iwata's ZnO epitaxial thin film on a- and c-plane sapphire are shown as filled squares and filled circles, respectively [26].

theoretically calculated value for electron scattering in ZnO, which can be used as a guide for improving ZnO electrical properties. Recently, high quality ZnO bulk crystals have been fabricated by the Eagle-Picher Corporation. These bulk crystals have the best-reported electrical properties at present. The mobility and the carrier concentration values of these samples are plotted in Figure 2-4. The room temperature electrical properties of ZnO epitaxial thin films grown on a-plane and c-plane sapphire are reported by K. Iwata [26]. In his work, the mobility of ZnO grown on sapphire is lower than that of the theoretical value due to defects. To reach the theoretical value of mobility, it will be necessary to significantly reduce the defect density in the films.

Table 2-2 resistivities, carrier concentrations, and dopant content for ZnO films doped with various impurities [27]

Dopant	Doping content (at%)	Resistivity (10^{-4} Ω cm)	carrier concentration (10^{20} cm^{-3})
Al	1.2 ~ 3.2	1.3	15.0
Ga	1.7 ~ 6.1	1.2	14.5
B	4.6	2.0	5.4
Y	2.2	7.9	5.8
In	1.2	8.1	3.9
Sc	2.5	3.1	6.7
Si	8.0	4.8	8.8
Ge	1.6	7.4	8.8
Ti	2.0	5.6	6.2
Zr	5.4	5.2	5.5
Hf	4.1	5.5	3.5
F	0.5	4.0	5.0

2.1.5 n-type ZnO Doped with Impurities

N-type ZnO films doped with cation (+3) or anion (-1) substitution have been developed as transparent conducting oxides (TCO) that can be used as electrodes in solar cells and flat panel displays. Table 2-2 summarizes the minimum resistivities and the maximum carrier concentration obtained for ZnO films prepared with optimal doping content for various dopant and deposition methods [27]. The ZnO:F and ZnO:B films were prepared by metal-organic chemical vapor deposition (MOCVD). All other impurity-doped ZnO films were prepared by magnetron sputtering deposition (MSD), pulsed laser deposition (PLD), or arc-discharge ion plating (ADIP). The optimal impurity doping content was dependent on the film deposition method as well as the dopant.

2.1.6 Tunable Bandgap for Heterostructures

In thin-film semiconductor research, the formation of heteroepitaxial interfaces has proven to be enabling in the development of numerous device concepts, as well as in the investigation of low dimensional phenomenon [28]. Heterostructures of thin films generate band offsets and carrier confinement suitable for novel device development and fundamental studies. The bandgap of ZnO films can be changed from 2.8 eV to 4.0 eV by doping with Cd or Mg. ZnO is hexagonal, whereas MgO and Cd are cubic. However, the similarity in ionic radii and valence charge between Mg^{+2} (1.36 Å) and Zn^{+2} (1.25 Å) allows significant metastable substitution into either structure. According to the phase diagram [29], MgO allows a maximum of 56% ZnO substitution at 1600 °C while maintaining the rock salt structure, with the lattice constant staying close to that of pure MgO (4.208 Å). In the case of ZnO, the bulk solid solubility of Mg is

limited to only 2 at% maximum, and the unit cell retains its hexagonal structure. Using pulsed laser deposition, A.K. Sharma *et al.* and A. Ohtomo *et al.* have reported nonequilibrium phase space corresponding to 36 at.% Mg in epitaxial ZnO while maintaining the ZnO hexagonal structure[30]. These films also exhibited favorable optical characteristics of wide band gap materials, including transparency in the visible and high exciton binding energy. The near edge bandgap photoluminescence of $(Mg_xZn_{1-x})O$ films at room temperature (295 K) was changed from 3.36 to 4 eV [30].

S. Choopun *et al.* reported the band gap relations in (Mg,Zn)O alloys for Mg varying from 0% to 100% [28]. Figure 2-5 shows the band gap energy of the (Mg,Zn)O alloys as a function of composition, including a virtual crystal approximation assuming the band gaps for MgO (cubic system) and ZnO (cubic system) to be 7.9 and 3.27 eV, respectively. The band gaps of the (Mg,Zn)O alloys for $x = 0$ to 0.3 were taken from reported data by Ohtomo *et al.* corresponding to hexagonal $(Mg_xZn_{1-x})O$ films [30]. The data for the virtual crystal approximation were derived from

$$E_g(Mg_xZn_{1-x}O) = xE_g(MgO) + (1-x)E_g(ZnO)$$

where E_g is the band gap energy. From the above equation, the band gap energy of cubic $(Mg_xZn_{1-x})O$ films appears to be linearly dependent of Mg content. A discontinuity and the change of slope in the band gap relation near the alloy composition of $Mg_{0.35}Zn_{0.65}O$ corresponds to a structural phase transition from wurtzite to cubic.
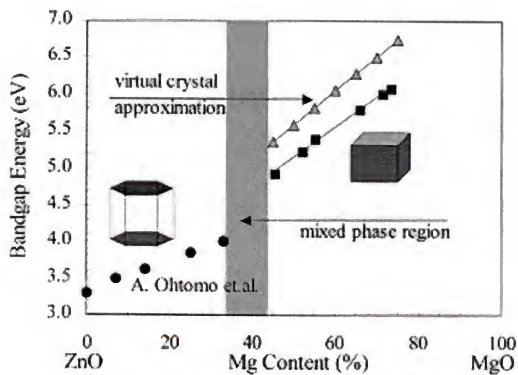
Fig. 2-5 Band gap energy as a function of Mg content. [30, 31]

2.2 One–dimensional Nanoscale Materials

In recent years, there has emerged significant interest in the synthesis of one-dimensional nanoscale materials [32]. One of the most attractive classes of materials for functional nanodevices are nanowires, nanorods, and nanotubes [33-38]. Nanodevice functionality has been demonstrated with these materials in the form of electric field-effect switching [39], single electron transistors [40], biological and chemical sensing [41], and luminescence [42] for 1D semiconducting structures. Various means have been reported for the synthesis of nanowires, nanorods, and nanotubes [43-45]. The understanding of growth mechanism and synthesis method is necessary for the realization of the nanoscale device applications.

2.2.1 Quantum Effect on Transport Properties

As the scale of microelectronic devices continue to decrease, the nature of electron transport through one-dimensional nanoscale channels such as nanowires and carbon nanotubes has become important. As the length of a wire approaches the mean free path of electrons, the transport mechanism changes from diffusive to ballistic as shown in Figure 2-6. When the width of the wire is larger than the Fermi wave length and the length of the wire is larger the mean free path, the electron transport is diffusive and follows the classical scattering mechanisms that include elastic scattering by impurities, phonon-phonon scattering, and electron-electron scattering. As the width of the wire approaches the Fermi wave length, the electrical conductance through the nanowire is theoretically quantized in units of $2e^2/h$ ($= (12.9 \text{ k}\Omega)^{-1}$). The conductance through a narrow constriction is generally described by the Landauer equation [46]:
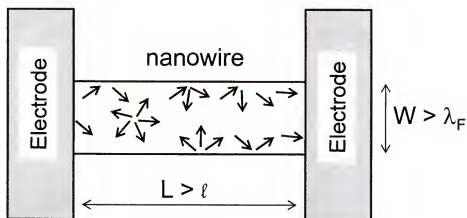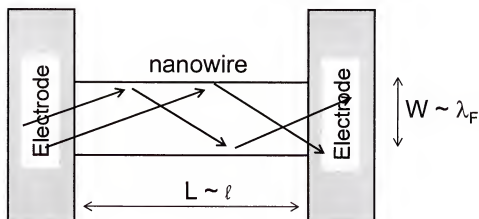
Fig. 2-6 Mechanism of (a) diffusive and (b) ballistic electron transport. W: width of nanowire, L: length of nanowire, ℓ: mean free path of conduction electron, and λ_F: Fermi wave length of conduction electron.

$$G_e = (2e^2/h)\Sigma T_i$$

where T_i is the electron transmission probability for the i-th conductance channel. Since $T_i = 1$ for ballistic transport, the conductance of a nanowire with N conduction channels is expressed:

$$G_e = (2e^2/h)N$$

For a potential difference between the electrodes, electrons having energies from E_f to $E_f + eV$ contribute to the conduction current, where E_f is the Fermi energy. Taking spin degeneracy into account, then, $G_e = 2e^2/h$ is obtained for each conduction channel. The number of conduction channels, ie the number of participating quantum states, depends on the width of the nanowire, so the conductance should decrease stepwise as the nanowire is narrowed [47].

The thermal conductance of phonon waveguides in the ballistic, one-dimensional limit calculated using the Landauer formula is simplified in the limit $k_B{}^2T \leq h/2\pi\omega_m$. For ideal coupling between the ballistic thermal conductor and the reservoirs, yielding modal transmission coefficients, T_m, equal to unity, a fundamental relation holds for each mode [48],

$$G_{th} = \pi^2 k_B{}^2 T/(3h)$$

This quantum of thermal conductance, $G_{th} = (9.456 \times 10^{-13} \ W/K^2)T$, represents the maximum possible value of energy transported per phonon mode. The factor of T, which gives the thermal conductance quantum a linear dependence upon temperature, reflects the fact that the quantity transported is energy (that is, entropy). In the case of electronic conduction, the corresponding quantity is the electron charge, e, and the electrical conduction quantum per spin-degenerate band is temperature independent, $G_e = 2e^2/ h$.

2.2.2 Growth Mechanism

2.2.2.1 Vapor-liquid-solid (VLS) model

The most popular method for producing nanowires involves vapor–liquid–solid (VLS) growth. This mechanism was proposed to explain the growth of large single-crystalline Si whisker by Wagner in the 1960s [49]. The growth of nanowires, nanotubes, and nanorods for numerous materials has been explained by this model and is illustrated in Figure 2-7. Consider a eutectic reaction between a catalyst and a material B. In the first step, catalyst (usually Au metal) is deposited on a substrate as a thin film or as nanoparticles. Material B is introduced on the catalyst surface as a vapor. By increasing above the eutectic temperature, material B and the catalyst form a liquid phase at point II in Figure 2-7. The nanowire (B) starts to nucleate and grow after the liquid phase becomes supersaturated at points III and IV. If the nanowires grow following this VLS mechanism, a catalyst particle should be suspended at the top of the nanowire. The nanowire size is determined by the liquid catalyst size during the growth. Table 2-3 shows a summary of single crystal nanowire material, the synthesis of which can be explained by this model [50].

2.2.2.2 Root-growth model

The root-growth mechanism is usually observed in the growth of carbon nanotubes from a metal nanoparticle on a substrate by the CVD method as shown in Figure 2-8 [38]. First the hydrocarbon decomposes on the metal nanoparticles into hydrogen and carbon, which dissolves in the metal (Fig. 2-8 a). When the carbon becomes super-saturated in the nanoparticle, it starts to precipitate in the form of a graphite sheet. Since the edges of the graphitic sheet are unstable, the emergence of pentagon defects, leading to the formation
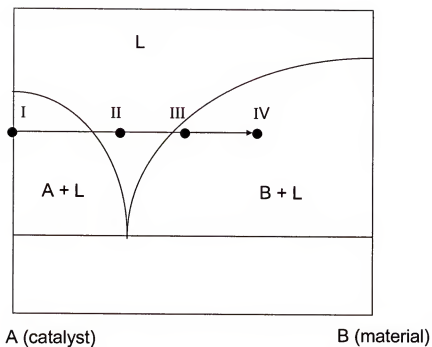
(a)
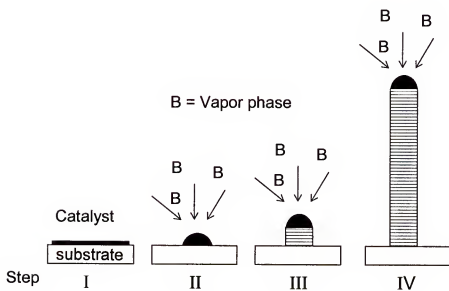
(b)

Fig. 2-7 Schematic diagram of (a) catalyst-material eutectic phase diagram, and (b) a vapor-liquid-solid model.

Table 2-3. Summary of single crystal nanowire synthesized. All of the nanowires were synthesized using Au as the catalyst, except GaAs, for which Ag and Cu were also used [50].

Material	Growth Temperature (°C)	Minimum Diameter (nm)	Average Diameter (nm)	Structure	Growth Direction
GaAs	800 ~ 1030	3	19	Zinc blende	<111>
GaP	870 ~ 900	3-5	26	Zinc blende	<111>
$GaAs_{0.6}P_{0.4}$	800 ~ 900	4	18	Zinc blende	<111>
InP	790 ~ 830	3-5	25	Zinc blende	<111>
InAs	700 ~ 800	3-5	11	Zinc blende	<111>
$InAs_{0.5}P_{0.5}$	780 ~ 900	3-5	20	Zinc blende	<111>
ZnS	990 ~ 1050	4-6	30	Zinc blende	<111>
ZnSe	900 ~ 950	3-5	19	Zinc blende	<111>
CdS	790 ~ 870	3-5	20	Wurtzite	<111>
CdSe	680 ~ 1000	3-5	16	Wurtzite	<100>,<002>
$Si_{1-x}Ge_x$	820 ~ 1150	3-5	18	Diamond	<111>
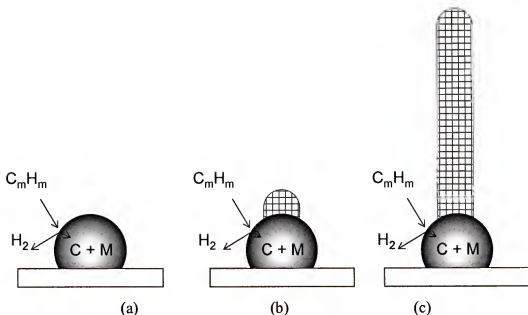
Fig.2-8 Root-growth model for the formation of carbon nanotubes from a metal catalyst nanoparticale.

of a curved fullerene cap (Fig. 2-8 b), becomes energetically favored, as it allows the dangling bonds of this cap to be stabilized by coordination with the metal. The elongation of the nanotubes is achieved by incorporation of further carbon into the metal-carbon bonds at the growing end (Fig. 2-8 c).

2.2.3 Synthesis Method

2.2.3.1 Vapor-phase transport

Vapor that is evaporated from the solid is transported to substrates that are positioned at the reaction zone of a tube furnace. The temperatures of the evaporation zone and reaction zone can be separately manipulated to control the growth of the nanowires. This method is simple and achieves a fast growth rate of nanowire. M.H. Hung *et al.* reported that ZnO nanowires can be grown by this method [51]. In this work,

an equal amount of ZnO powder and graphite powder were ground and put in an alumina boat crucible. Au coated Si was used as the substrate material and placed inside a small quartz tube along with the alumina boat. The substrates were typically placed 0.5±10 cm from the center of the alumina boat positioned at the center of the horizontal furnace with flowing Argon. The temperature of the furnace was ramped to 890 ~ 925 °C at a rate of 50±100 °C/min and typically kept at that temperature for the growth time under a constant flow of argon (20±25 standard cubic cm). Vapor-phase transport can be performed using a vertical tube furnace with the same concept.

2.2.3.2 Chemical vapor deposition

Conventional chemical vapor deposition (CVD) or metal organic chemical vapor deposition (MOCVD) has been used for the growth of nanowires. One difference between CVD and MOCVD is the use of metal catalyst coated substrates. The control of gas sources and gas flow rates is advantageous for controlling the morphology and growth rates. InP nanowire structures of vertical orientation were grown by the metal organic vapor-phase epitaxial technique using colloidal Au nanoparticles as the catalyst [52]. In this work, the nanowires were grown on Fe-doped (111) InP substrates in a vertical MOVPE reactor operating at a low pressure of 76Torr and using hydrogen as the carrier gas. Trimethylindium (TMI) and tertiarybutyl phosphine (TBP) were used as the precursors for group III and V sources, respectively. The substrates, coated with Au, where held at a temperature of 430 °C. The V/III ratio during the growth was kept constant at 120 and the growth time was 1 min. The V/III ratio reported was calculated from the nominal supplies of the TMI and TBP mole fractions to the reactor, the actual

value of which on the sample surface might be significantly smaller due to inadequate cracking of TBP at the relatively low growth temperature of 430 °C. The high temperature anneal was carried out to remove the initial native oxide on the surface as well as for forming an initial Au–In eutectic liquid, necessary for the VLS growth, by consuming In from the substrate by the molten Au particle at high temperature. The vertically aligned nanowires were grown in a <111> direction along the long axis of the nanowires. The distribution in diameter of the nanowires varied in the range of 5–50 nm, with the most probable diameter between 20 and 25 nm.
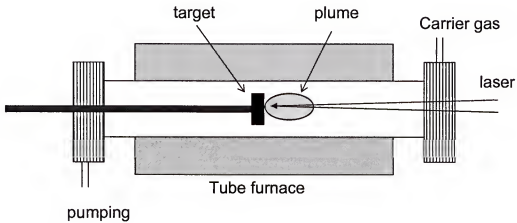

Fig. 2-9 a schematic diagram of laser ablation system

<u>2.2.3.3 Laser ablation</u>

This technique is similar to that used for the growth of thin films using pulsed laser deposition. Figure 2-9 shows a schematic diagram of a laser ablation system for nanowire synthesis. A target containing catalytic metal and the material of interest is

placed in the center of a tube furnace set to a desired growth temperature and under a flow of carrier gas, and hit by a pulsed laser beam. A plume of metal and material of interest is generated from the target. The laser-generated clusters are maintained in the liquid state with temperature control. The nanowires start to grow from the supersaturated clusters. Heterostructured nanowires can be grown by using two targets during the growth. Gallium arsenide (GaAs)/gallium phosphide (GaP) superlattices were grown by this method using GaAs and GaP targets [53]. Single wall carbon nanotubes (SWNTs) were synthesized using a target of graphite and a small amount of Co and Ni powder at 1200°C. Each fiber of this material consists of a rope of 100 to 500 parallel SWNTs, closed packed as a two-dimensional triangular lattice [54].

2.2.3.4 Electrical arc discharge

This method has been used for the growth of carbon nanotubes. It consists of applying a voltage between two graphite electrodes held close together in a chamber filled with an inert gas. The electrical discharge that takes places between the electrodes heats up the region to thousands of degrees, leading to the evaporation of carbon. Carbon nanotubes are grown on the end of the negative electrode by the crystallization of the carbon vapor. Highest et al. reported that SWNTs in the form of highly crystalline bundles were produced by using the positive graphite electrode with 1% Y and 4.2 % Ni [55]. The arc discharge was created by a current of 100 A; a voltage drop of 30 V between the electrodes was maintained by continuously translating the anode to keep a constant distance (~3 mm) between it and the cathode.

2.2.4 Nanowires and Nanobelts of ZnO

ZnO nanowires are attracting attention for the potential application of nanoscale devices. <0001> oriented zinc oxide nanowires, grown on sapphire substrates coated with Au films as a catalyst, has been synthesized using a vapor transport process [42]. The growth of ZnO is initiated on Au nanoclusters. The mechanism of the ZnO growth is described by the vapor-liquid-solid model. Many works efforts have been reported on the growth of ZnO nanowires with different methods, such as vapor-phase transport via a vapor-liquid-solid mechanism[51,56], gas reaction [57], metal-organic chemical vapor deposition[58], and the oxidation of metal in the pores of anodic alumina membranes[59,60]. Anodic alumina membranes(AAM) grown in acid electrolytes possess hexagonally ordered porous structures with pore diameters ranging from 10 to 200 nm, with pore lengths from 1 to over 100 μm, and pore densities in the range of 10^{10} to 10^{12} cm^{-2}. ZnO nanowires have been grown by oxidation treatments of Zn metal electrodeposited in the pores of AAM at 300°C for 35 hrs in air. Diethylzinc (DEZn) and oxygen were employed as the reactants, and argon was used as a carrier gas in metal-organic chemical vapor deposition (MOCVD). The gas reaction method is similar to the vapor transport method that was described earlier. The only difference is the use of Zn metal instead of ZnO powder.

The growth of ZnO nanowires is observed for various catalysts, including Au, Co, Cu, and even without a catalyst [51, 56, 58, 61, 62]. Most reported work uses Au as a catalyst for ZnO growth. The growth direction of ZnO, following a c-axis direction along a long axis of nanowire, does not show any dependence on the crystal orientation of the

catalysts. The typical diameter of ZnO nanowire ranges from 15 nm to around 200 nm, usually dependent on the size of the catalyst.

The vertical alignment of ZnO nanowires in the c-axis growth direction depends on the crystal direction of the substrate. A good epitaxial interface between ZnO epitaxial layers and sapphire yields the ZnO/a-plane sapphire orientational relationship along the surface normal of ZnO [0001] ∥ sapphire [11$\bar{2}$0] and in plane with the ZnO <11$\bar{2}$0> direction lying parallel to the sapphire [0001] direction [63]. Therefore, the <0001> preferential ZnO nanowire growth surface normal to a-plane sapphire is due to the orientational relationship between ZnO and a-plane sapphire as shown in Figure 2-11 a. However, the *m*-plane of sapphire is inclined 30 degrees to its *a* plane and the (0001) plane of ZnO is incommensurate with the (100) plane of sapphire, the [0001] direction of the ZnO nanowires grown on *m*-plane sapphire is achieved by a 30 degree rotation from the *m*-plane normal as shown in Figure 2-10 [64].

ZnO nanobelts were synthesized by simply evaporating the desired commercial metal oxide powders at high temperatures without the presence of catalyst [65]. ZnO nanobelts have a uniform width along their entire length. The typical widths of the nanobelts are in the range of 50 to 300 nm. The typical thickness and width-to-thickness ratios of the ZnO nanobelts are in the range of 10 to 30 nm and ~5 to 10, respectively. Two growth directions have been observed in ZnO nanobelts. The nanobelt, growing along the [0001] and enclosed by the ±(2$\bar{1}$$\bar{1}$0) and ±(01$\bar{1}$0) facets, shows no defect or dislocation. Another, growing along the [01$\bar{1}$0] and enclosed by the ±(0001) and ±(2$\bar{1}$$\bar{1}$0) facets, is also dislocation free but contains a single stacking fault that is parallel to the axis and runs throughout the entire length of the nanobelt.
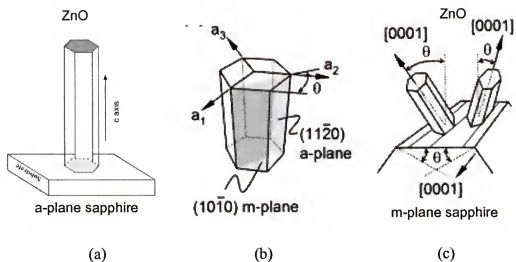
Fig. 2-10 Schematic diagram of (a) ZnO nanowire on a-plane sapphire, (b) the angular relationship between the *m*- and *a*- plane of sapphire, and (c) the growth direction of ZnO nanowire on m-plane sapphire. θ=30° [64].

2.3 Doping for p-type ZnO

2.3.1 Doping Limitation of Compound Semiconductors

The requirement for semiconductor devices using a p-n junction structure is ambipolar (n- and p-type) doping. The limited dopability for both p-type and n-type in one material hinders its application for electronic and optoelectronic devices. For example, ZnTe can be p-doped to extremely high levels with most column V dopants [66], but it is difficult for ZnTe to be doped n-type. In contrast, ZnS and ZnSe are easily n-doped with Al. The explanation for this unipolarity of doping in compound semiconductors has been classified by two different mechanisms, namely pinning of the Fermi level or unstable dopant configurations due to the thermodynamic energy.

In the Fermi level pinning model of a defect, a phenomenological treatment of doping limitations starts from the observation that for many semiconductors the maximum dopability is connected to the energetic position of the band edges. If one tries to introduce donors and raise the Fermi energy above the energetic position of a compensation center, it becomes energetically favorable for the material to form the localized compensating center instead of adding the electron to the Fermi surface [67]. This leads to a pinning of the Fermi level at the energetic position of the compensating center. Figure 2-11 is the n-type pinning energy $E_F^{(n)}$ and p-type pinning energy $E_F^{(p)}$ relative to the absolute band edge energies of III-V and II-VI semiconductors [68]. Zunger proposed that, in ZnO, the $E_F^{(p)}$ level is considerably above the valence band maximum (VBM). Thus, the downwards moving E_F in deliberate p-type doping will encounter $E_F^{(p)}$ before encountering the VBM. At this point the system will generate spontaneous hole-killers (e.g., Zn_i or V_O) before any significant doping commences.

III-V Compounds

AIP GaP InP AIAs GaAs InAs AISb GaSb InSb

II-VI Compounds
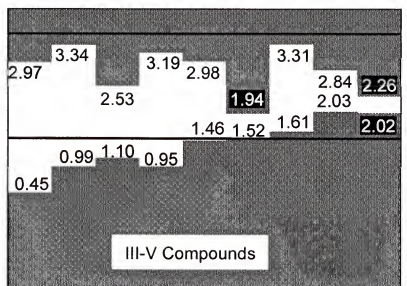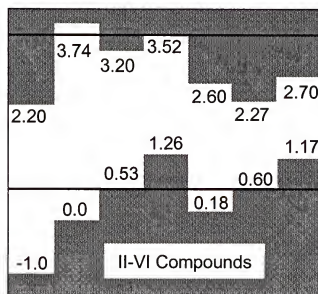
ZnO ZnS ZnSe ZnTe CdS CdSe CdTe

Figure 2-11 the n-type pinning energy $E_F^{(n)}$ and p-type pinning energy $E_F^{(p)}$ relative to the absolute band edge energies of III-V and II-VI semiconductors [68].
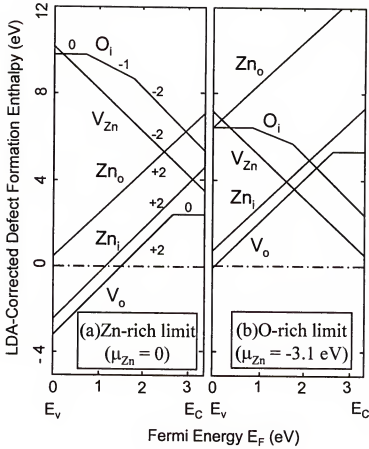
Fig. 2-12 Defect formation enthalpies after LDA correction are shown as lines as a function of the Fermi energy EF at the zinc-rich(μ_{Zn}=0) and oxygen-rich (μ_{Zn}=-3.1eV limits, respectively. The charge states of the defects are shown as -2, -1, 1, and +2. Defect transmission energies are shown as solid dots.

Hence, there is a difficulty in equilibrium p-doping of ZnO. In contrast, in tellurides or antimonides, $E_F^{(p)}$ is at or below the VBM, so a considerable density of holes can be generated before the pinning energy is encountered and killer defects form.

In the thermodynamic approach, T. Yamomoto et al [69,70], using ab initio electronic band structure calculations, reported a substantial decrease in the Madelung energy of n-type ZnO (V_O and Zn_i) compared with that of stoichiometric ZnO, which causes the stabilization of ionic charge distributions in n-type ZnO. S. B. Zhang et al. [71]

studied the microscopic equilibrium mechanism that explains the intrinsic asymmetry in ZnO. ZnO is intrinsically n-type at Zn-rich conditions. This is because the Zn interstitial, Zn_i, is a shallow donor, supplying electrons; its formation enthalpy is low for both Zn-rich and O-rich conditions as shown in Figure 2-12, so this defect is abundant. The native defects (interstitial O, O_i, and Zn vacancy, V_{Zn}) that could compensate the n-type doping effect of Zn_i have high formation enthalpies for Zn-rich conditions, so these "electron killers" are not abundant. They suggest that ZnO cannot be doped p-type via native defects (O_i, V_{Zn}) despite the fact that they are shallow (i.e., supplying holes at room temperature). This is because, at both Zn-rich and O-rich conditions, the defects that could compensate p-type doping (V_O, Zn_i, Zn_O) have low formation enthalpies, so these "hole killers" form readily.

2.3.2 Dominant Donors for an Intrinsic n-type ZnO

ZnO has several types of intrinsic defects, such as Zn_O, Zn_i, V_O, O_i, and V_{Zn}. The oxygen vacancy (V_O) has been identified in electron paramagnetic resonance (EPR) studies as a deep donor [72], although the energy has not been measured. Vanheusden et al. [73] argued that, since the free carrier concentration was much larger than V_O in their samples, there had to be another source of donors, possibly Zn_i. D.C. Look et al. [74] suggested that Zn_i (and not V_O) is the dominant native shallow donor in ZnO by studying the high-energy electron irradiation in ZnO. Hydrogen may be non-intentionally incorporated in wide band gap semiconductors when grown or processed under hydrogen-rich ambient. Hydrogen strongly interacts with dopants (mostly acceptors) in wide band gap semiconductors and passivates them [75]. Chris G. Van de Walle [76] reported,

based on first-principles density functional calculation, that hydrogen is an excellent candidate for a shallow donor. Hydrogen is ubiquitous and very difficult to remove from the crystal growth environment. It also forms a strong bond with oxygen, providing a powerful driving force for its incorporation in the ZnO crystal. This incorporation is accompanied by remarkably large relaxations of the surrounding atoms. The resulting O-H bonding unit can, in fact, be regarded as a new type of dopant atom, the addition of the proton turning the oxygen into an element behaving much like fluorine. In ZnO, hydrogen occurs in the positive charge state; ie, it always acts as a donor. He also showed that H^+ is the stable charge for all Fermi level positions. The formation energy of H^+ is low enough to allow for a large solubility of hydrogen in n-type ZnO. Compensation by hydrogen donors is thus an important concern when acceptor doping of ZnO is attempted. A complex, consisting of an oxygen vacancy and a hydrogen atom, also behaves as a shallow donor. The calculated binding energy, expressed with respect to H^+ and V_O^o, is 0.8eV. Oxygen vacancies are low-energy defects and may form in large concentration. In n-type ZnO, these vacancies would be neutral and electrically inactive, but the addition of hydrogen turns them into shallow donors.

2.3.3 Approach to p-type Doping in ZnO

Recently, many researchers have reported efforts to grow p-type ZnO. Y. R. Ryu et al reported that p-type ZnO is obtained in arsenic-doped ZnO (ZnO : As) films deposited on (0 0 1)-GaAs substrates by pulsed laser ablation [77]. Y. -D. Ko et al. reported that p-type ZnO on Si substrate is obtained using rf magnetron sputtering followed by Zn_3P_2 diffusion process [78]. Minegishi et al. reported realizing p-type ZnO

using simultaneous codoping of NH_3 and excess Zn, obtaining a resistivity of 100 $\Omega\cdot$cm [6], but had difficulty with reproducibility. W. Wang et al did not observe p-type ZnO grown by plasma-assisted metal-organic chemical vapor deposition (MOCVD) on sapphire using N_2 for the dopant source [7]. Recently, nitrogen doped ZnO layers were grown on a sapphire substrate by simultaneously introducing O_2 and N_2 via one RF source.[8,9] The carrier type conversion from n-type to p-type ZnO was not observed. However, D. C. Look et al also reported the homoepitaxial p-type ZnO on a Li-doped semi-insulating ZnO substrate by simultaneously introducing O_2 and N_2 via RF source using molecular beam epitaxy [10]. Joseph also reported that p-type ZnO has been fabricated by passing N_2O gas through an electron cyclotron resonance (ECR) using the pulsed laser deposition technique (PLD) [11]. In spite of promising results showing p-type ZnO achieved by extrinsic dopants, the reproducibility, low carrier concentration, and low mobility of p-type ZnO is still a problem for semiconducting devices. The method and mechanism for achieving ZnO has not been clearly delineated.

Theoretical approaches have addressed the doping problem of the wide –bandgap semiconductor ZnO [68-70]. One suggestion in achieving p-type doping is to eliminate the spontaneous formation of anion vacancy hole-killers. It may prove easier to do p-type doping via cation-site substitution using anion-rich conditions, whereas n-type doping can be done via anion-site substitution using cation-rich conditions. However, in the theoretical calculation of formation energies of N_o and $(N_2)_O$, for gases such as N_2, N_2O, NO, and NO_2 shown in Figure 2-13 [79], the formation energy of an $(N)o$ at an O site, known to act as an acceptor, is lower in the Zn-rich condition than in the oxygen rich condition. K. Nakahara et al. reported that the nitrogen concentration also depended on

the Zn flux. With SIMS results, the Zn-rich condition gives a higher incorporation of Nitrogen in ZnO.

The codoping method using acceptors(A) and donors(D) as the reactive codopant contributes (i) to the enhancement of the incorporation of the acceptors because the strong attractive interactions between the acceptor and donor dopants dominate the repulsive interactions between the acceptors, where the driving force is the electrostatic energy gain associated with partial compensation, and (ii) to lowering of the energy levels of the acceptors and raising those of the donors in the band gap due to the strong attractive
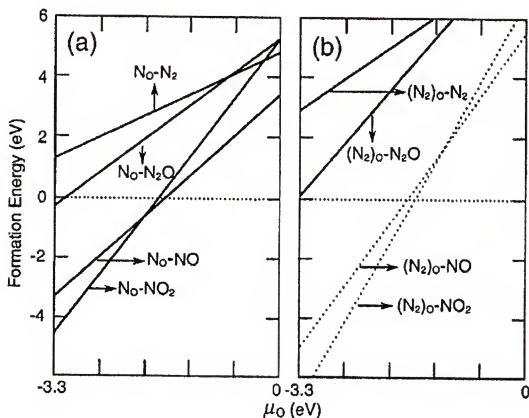
Fig. 2-13 (a) Calculated formation energies of N_O as functions of the O chemical potential formed by atomic N (stripped off an N_2 or an N_2O molecule), NO, or NO_2 molecule. $\mu_O = -3.3$ is the Zn-rich limit condition and $\mu_O = 0$ is the O-rich limit condition. (b) Calculated formation energies of $(N_2)_O$ as functions of the O chemical potential for the defects formed by N_2, N_2O, NO, or NO_2 molecules [79].

interactions between the acceptor and donor as reactive codopants, as shown in Figure 2-14. A non-random configuration, such as A–D–A trimers which occupy nearest-neighbor sites or trimer-like complexes, is postulated to produce the required reduction ionization energy of the acceptor impurities for materials doped with acceptors alone [70]. The formation of complexes, including the III (=Al, Ga and In) — N pair, which occupy nearest-neighbor sites, and a more distant N, located at the next-nearest-neighbor site in a layer closest to the layer, including the III---N pair, is due to the strong repulsive interaction between the N acceptors. Holes are localized by repulsion effects due to narrow N- impurity bands for ZnO:N without codoping [70]. When the codopant is
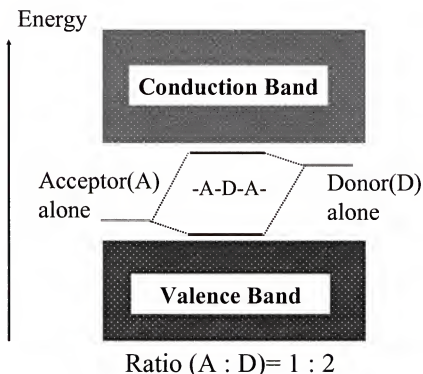

Fig. 2-14. Schematic energy diagram for p-type codoped semiconductors. The acceptor (A) level is lowered and the donor (D) level is raised with the formation of acceptor–donor–acceptor complexes upon codoping [70].

introduced to N-doped ZnO, hybridization between p states at acceptor sites and s states at the sites of codopant donor, such as Al and Ga, with a larger Bohr radius and high solubility is very effective for the enhancement of the Bohr radius of N acceptor. In p-type codoped materials, therefore, acceptor orbitals can overlap sufficiently for good conduction to occur. The change from localized impurity states in ZnO doped with N alone to delocalized states in p-type codoped materials can make a shallow acceptor of N. Therefore, the codoping of donors with acceptors is essential for the enhancement of acceptor incorporation, with a decrease in the lattice energy and a decrease in the binding energy of the acceptor impurity in highly doped p-type ZnO. The donor may be not the p-type killer, but instead activate acceptors.

Zugger suggested that the local chemical bonding energy around the dopant could be enhanced via decorating the dopant by strongly bonding ligands which do not disrupt the host bonds [68]. For example, whereas the four Zn–N bonds, formed when N dopes the O site in ZnO, are weak, replacing one Zn by Al (a donor) in otherwise pure ZnO and replacing the four oxygen neighbors by four nitrogen atoms (acceptors), creates a total of four very strong Al–N bonds around Al_{Zn}, followed by 12 weak Zn–N bonds around each of the four N sites. Since AlN is extremely stable, $\Delta E_b = 4E_{Al-N} + 12E_{Zn-N} < 0$. Such cluster-doping ideas, with a ratio of 4:1 between acceptors and donors, could facilitate stable local dopant bonding and enhanced solubility. Interestingly, this cluster-doping is predicted to be more stable than codoping between acceptors and donor (a ratio of 2:1).

CHAPTER 3
SITE-SPECIFIC GROWTH OF ZnO NANOWIRES USING CATALYSIS-DRIVEN MOLECULAR BEAM EPITAXY

3.1 Introduction

While ZnO nanowires provide interesting systems for investigating fundamental properties or for exploring device concepts via single prototype device construction, the ability to synthesize nanorods at arbitrary locations at moderate temperatures is needed for nanodevice integration. This requires site-specific nucleation of nanorods, as well as a growth process that remains site specific and is compatible with the device platform of interest. It would be advantageous to achieve nanorod growth from a flux source that could be controlled at the atomic level, thus enabling compositional modulation along the rod length.

In this chapter, the site-selective growth of ZnO nanowires using a catalysis-driven molecular beam epitaxy (MBE) method is reported. Low temperature MBE conditions are identified so that ZnO nucleation and growth occurs only on the deposited metal catalyst. With this approach, site specific, single crystal ZnO nanowire growth is achieved with nanowire diameters as small as 15 nm.

3.2 Experimental

The growth experiments were performed using a conventional MBE system. The background base pressure of the growth chamber was $\sim 5 \times 10^{-8}$ mbar. An ozone/oxygen mixture was used as the oxidizing source. The nitrogen-free plasma discharge ozone

36

generator yielded an O_3/O_2 ratio on the order of 1%–3%. No effort was made to separate the molecular oxygen from the ozone. The cation flux was provided by a Knudsen effusion cell using high purity (99.9999%) Zn metal as the source. Cation and O_2/O_3 partial pressures were determined via a nude ionization gauge that was placed at the substrate position prior to growth. The beam pressure of O_3/O_2 mixture was varied between 5×10^{-6} and 5×10^{-4} mbar, controlled by a leak valve between the ozone generator and the chamber. The Zn pressure was varied between 5×10^{-7} and 4×10^{-6} mbar. The substrates were Si wafers with native SiO_2 layer terminating the surface. Site-selective nucleation and growth of ZnO was achieved by coating Si substrates with Ag islands. For thick Ag, a continuous ZnO film could be deposited. For nominal Ag film thickness of 20–200 Å, discontinuous Ag islands are realized. On these small metal islands, ZnO nanowires were observed to grow. Efforts to deposit ZnO on Ag-free SiO_2/Si surface area under a variety of growth conditions proved unsuccessful. Zn metal deposition could be achieved at substrate temperatures of 25–100 °C, but with no ZnO formation for a wide range of O_2/O_3 partial pressure. Higher substrate temperatures yield no deposition as the Zn metal vapor pressure rises quickly at moderate temperatures. Typical growth times for ZnO on the Ag-coated silicon was 2 hrs with growth temperatures ranging from $T_g = 300$ to 500 °C. After growth, the samples were evaluated by x-ray diffraction, scanning electron microscopy (SEM), transmission electron microscopy (TEM), and photoluminescence.

3.3 Results and Discussion

3.3.1 Growth Condition of ZnO Nanowires

The growth of ZnO depends on the thickness of Ag that is used as catalysis. Figure 3-1 shows SEM images of ZnO grown on a Ag-coated Si wafer with Ag thickness of (a) 20 nm and (b) 100 nm. Zn pressure was 2×10^{-6} mbar. O_3/O_2 pressure was 5×10^{-5} mbar. The growth temperature was 400°C. Growth of ZnO nanowires was not observed on bare Si regions. On thick and continuous Ag thin films, ZnO nucleated on Ag, but did not grow as nanowires. Only on discontinuous Ag islands did ZnO nanowires grow.

Figure 3-2 shows scanning electron microscopy images of ZnO nanowires grown on a Si wafer that was coated with a nominally 10 nm thick layer of Ag. The Ag was deposited using e-beam evaporation. The images are for ZnO nanowires grown at 400 °C and 500 °C with a Zn pressure of 2×10^{-6} mbar and an oxygen/ozone pressure of 5×10^{-4} mbar. Under these conditions, ZnO deposition was observed only on the Ag with no growth on regions of the SiO_2-terminated Si surface that was devoid of Ag. A dense entangled collection of ZnO nanowires is observed to grow from the surface. Both cylindrical nanowires and faceted whiskers can be observed in the forest of ZnO nanostructures grown at 400 °C. At higher temperatures such as 500°C, only nanowires are observed as shown in Figure 3-2 (b). In many cases of 400°C growth temperature, the length of ZnO nanowires is in excess of 2 μm. Note also that multiple nanowires are observed to nucleate from the relatively large Ag islands. As such, it does not appear that the diameter of the nanowires is determined by the initial radii of the Ag islands.

X-ray diffraction of the deposited materials confirms that the material is ZnO. Figure 3-3 shows X-ray diffraction patterns taken along the surface normal, indicating only ZnO peaks. The diffraction pattern for the material grown at 400 °C is consistent
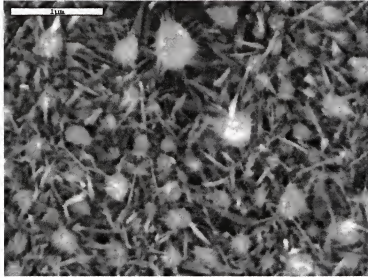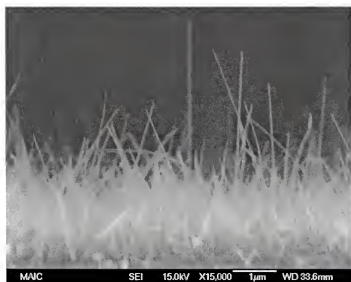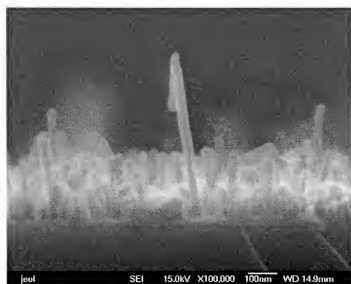
(a)
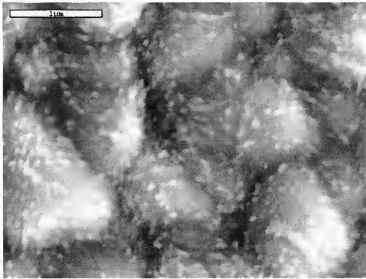
(b)

Fig. 3-1 SEM image of ZnO grown on Ag-coated Si wafer as a function of coating thickness of silver (a) 20 nm and (b) 100 nm with Zn pressure of 2×10^{-6} mbar and O_3/O_2 pressures of 5×10^{-5} mbar at 400°C of growth temperature.

(a)

(b)

Fig. 3-2 Scanning electron microscopy image of ZnO nanowires grown at (a) 400 °C and (b) 500 °C.

with randomly oriented polycrystalline material, although selected area electron diffraction (discussed below) indicates a preferred c-axis orientation of individual nanowires along the long axis. A preferred (002) orientation seen for nanowires obtained at 500 °C indicates a more vertically aligned growth at this temperature.
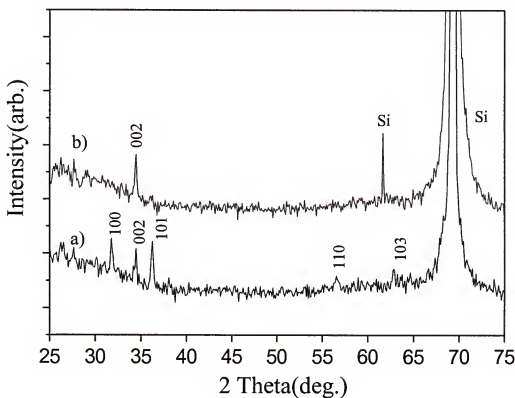

Fig. 3-3 XRD pattern of ZnO grown on 2nm Ag coated SiO2/Si substrate as a function of growth temperature a) 400°C, and b) 500°C.

3.3.2 Site-selective Growth of ZnO Nanowires

The most intriguing structures are those that result from isolated Ag nanoparticles. In depositing the Ag catalyst films, certain regions of the SiO_2/Si surface were shadowed from deposition, leading to a gradient in Ag thickness, Ag nanoparticle coverage, and

average nanoparticle diameter. Within these areas, isolated Ag nanoparticles could be located, thus allowing direct imaging of nanowire formation from individual Ag islands. Clusters of ZnO nanowires were observed to nucleate from these isolated Ag islands. Figure 3-4 shows field-emission SEM images of ZnO nanowire clusters, including a high resolution image of a single nanowire grown at 400 °C. Energy-dispersive spectrometry was used to determine the nanowire composition (ZnO) in addition to confirming the absence of ZnO on regions of the substrate surface that are devoid of Ag. In order to acquire these images, the sample was coated with a thin layer of carbon to avoid charging effects. From the high-resolution image, the nanowire cross section appears to be cylindrical, although any faceting of the side walls might be obscured by the carbon coating. The thickness of the nanowire shown in Figure 3-4 is on the order of 30 nm, although the carbon coating may exaggerate this thickness.

The potential for growing single nanowires on selected locations is exemplified in Figure 3-5 that shows field-emission SEM images of ZnO nanowire grown on Ag nano-particles dispersed on a Si substrate with Zn pressure of 2×10^{-6} mbar and O_3/O_2 pressure of 5×10^{-4} mbar at growth temperature of 500°C. ZnO nanowires selectively nucleate and grow only on Ag nano-particles dispersed on Si substrate. Therefore, ZnO nanowires grow on Ag particles that act as catalysts.

3.3.3 Optical Properties

The optical properties of the nanowires were examined using photoluminescence. A He–Cd (325 nm) laser was used as the excitation source. The room-temperature luminescence reveals a robust near band-edge emission peak located at 375 nm indicating
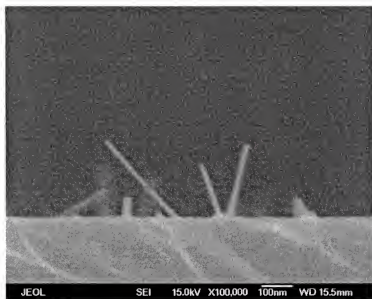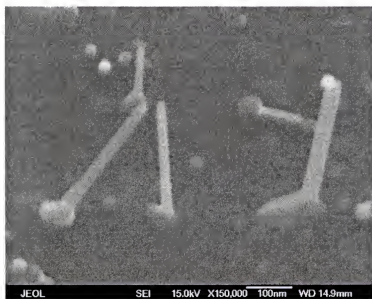
(a)

(b)

Fig. 3-4 Scanning electron microscopy image of ZnO nanowires grown at (a) 400 °C and (b) 500 °C.

(a)

(b)

Fig. 3-5 Field-emission SEM images of ZnO nanowire grown on Ag nano-particles dispersed on Si at 500°C growth temperature.

that nanowires are highly crystalline. This is consistent with luminescence reported for near-band-edge emission in epitaxial films [80,81] and larger diameter ZnO nanowires [82]. Figure 3-6 shows the photoluminescence spectra for nanowires grown at 400 °C and 500 °C. Note also that the broadband emission due to defect levels also differs. A broad, but weak, green emission peak is observed at ~2.8 eV for rods grown at 400 °C. This is typically associated with trap-state emission attributed to singly ionized oxygen vacancies in ZnO [83]. The emission is the result of the radiative recombination of photo-generated holes with electrons occupying the oxygen vacancy.
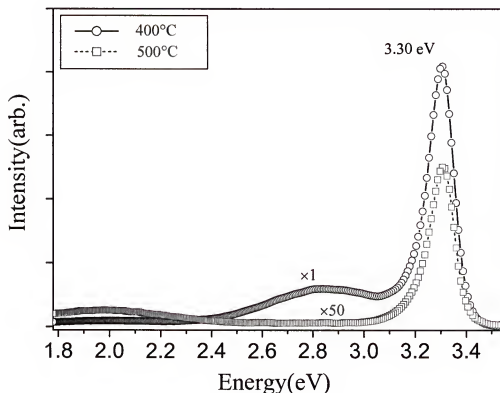

Fig. 3-6 Photoluminescence spectra for nanowires grown at 400 °C and 500 °C.

Similar results have been observed for ZnO nanorods formed via vapor transport. However, the nanorods grown at 500° C exhibit a broad emission center at ~2.0 eV.

3.3.4 Growth Mechanism

In addition to SEM, the nanowires were examined using transmission electron microscopy. Figure 3-7 shows a transmission electron microscopy image of an individual ZnO nanowire. The nanowire shown in Figure 3-7 was not carbon coated. An estimate of the wire thickness is 20 nm. The high resolution TEM image and selected area diffraction of nanowire specimens indicate that the wires are single crystal ZnO, with the *c*-axis oriented along the long axis of the wire. Also evident in the image is a small particle embedded at the tip of the wire. This is similar to what is observed for other nanowire synthesis that is driven by a catalytic reaction, where catalyst particles become suspended on the nanowire tip [84,85]. Figure 3-8 shows the presence and compositional distribution of Ag, Zn, and oxygen in the single nanowire by energy-dispersive spectrometry measurement carried out in the STEM. This compositional line-scan, profiled from the body to the tip of the nanowire, indicates that the catalyst, Ag, exists at the tip of nanowire.

The mechanism for nanowire growth is catalysis driven, and appears to be related to the vapor–liquid–solid (v–l–s) model reported for the nanowire synthesis of other materials. Zn addition to Ag significantly suppresses the melting point of Ag/Zn alloy to that of Zn that is rather low (420 °C). The melting temperature of the nanosacle alloy will be lower than 400°C because a melting point of a nano material is lower than that of bulk material. ZnO nanoparticle formation via the internal oxidation of Zn in Ag/Zn
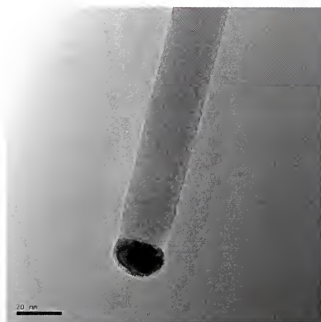
(a)
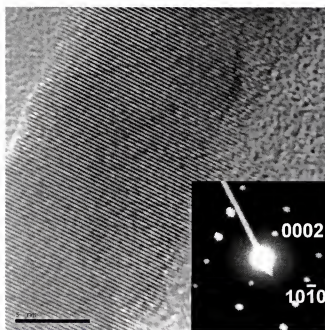
(b)

Fig. 3-7 TEM (a) image and (b) high resolution image and selected area diffraction of a single crystal ZnO nanowire.
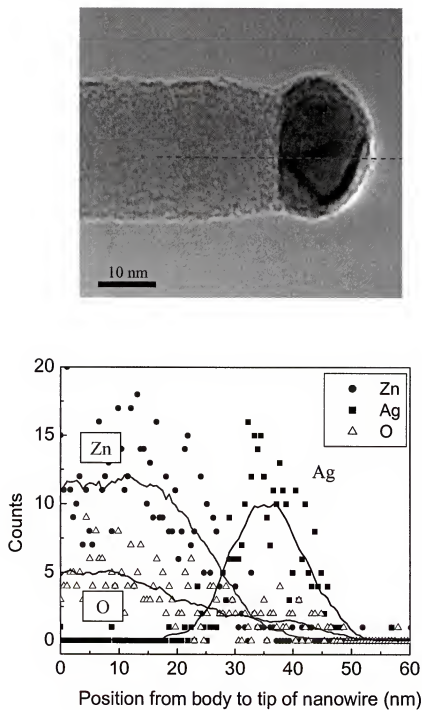
Fig. 3-8 Compositional line-scan from the body to tip of the nanowire probe by STEM EDS spectroscopy.

alloys has previously been reported [86]. In these studies, oxygen is diffused into an Ag/Zn alloy, with nanoscale ZnO precipitates forming in the bulk of the sample. For the present case of nanowire formation, the reaction between ozone/oxygen flux and the Ag islands appears to result in surface and subsurface oxygen diffusion in the metal island, perhaps involving the intermediate formation of Ag_2O. Zn atoms impinging on the Ag island surface then diffuse either on the surface or in the bulk of the island, where they react with the Ag_2O to form ZnO. One might anticipate rather high diffusion rates for Zn in Ag for the temperatures considered. The reactions at 400°C are as follows;

$$4Ag + O_2 = 2Ag_2O \quad \Delta G = +6 \text{ kJ/mole}$$

$$2Zn + O_2 = 2ZnO \quad \Delta G = -570 \text{ kJ/mole}$$

$$2Ag_2O + 2Zn = 2ZnO + 4Ag \quad \Delta G = -576 \text{ kJ/mole}$$

The existence of oxygen in the tip of nanowire as shown in Figure 3-8 supports the intermediate formation of Ag_2O. The formation enthalpy of ZnO at growth temperature is much lower than that of Ag_2O. The ZnO start to grow by catalytic reaction. The growth of ZnO nanowires follows the top growth mode.

CHAPTER 4
BIMODAL GROWTH OF CORED $(Zn_{1-x}Mg_x)O$ HETEROEPITAXIAL NANOWIRES

4.1 Introduction

The formation of complex, multicomponent structures and interfaces is needed for low-dimensional structures and electronic devices. In thin-film semiconductor research, the formation of heteroepitaxial interfaces has proven to be enabling in the development of numerous device concepts, as well as in the investigation of low dimensional phenomenon [28]. Unfortunately, such heterostructures have rarely been realized outside of the conventional 2-D planar thin-film geometry [87]. Nevertheless, the synthesis of 1-D linear heterostructures is scientifically interesting and potentially useful, particularly if a technique is employed that allows for spatial selectivity in nanowire placement. Addressing these challenges could prove enabling in realizing integrated device functionality.

In this chapter, the site-specific, spontaneous formation of 1-D heteroepitaxial structures is described. Three different types of structures will be described. First, the structures of nanowires consist of a single crystal, Zn-rich $Zn_{1-x}Mg_xO$ (x < 0.02) core encased by an epitaxial wurtzite $Zn_{1-y}Mg_yO$ (y >>0.02) sheath. Second, the nanowire is composed of a ZnO core surrounded by a cubic (Mg,Zn)O. Finally, (Mg,Zn)O nanowire having cubic rock salt structure will be described. The crystal structure, microstructure, and composition of the nanowire were identified by TEM, SEM, and photoluminescence measurements.

4.2 Experimental

The heteroepitaxial cored nanostructures reported here are based on the (Zn,Mg)O alloy system, and were synthesized using the catalysis-driven molecular beam epitaxy method. The growth experiments were performed using a conventional MBE system. The background base pressure of the growth chamber was approximately 5×10^{-8} mbar. An ozone/oxygen mixture was used as the oxidizing source. The nitrogen-free plasma discharge ozone generator yielded an O_3/O_2 ratio on the order of 1-3%. No effort was made to separate the molecular oxygen from the ozone. The cation flux was provided by Knudsen effusion cells using high purity (99.9999%) Zn metal and Mg (99.95%) as the source materials. Cation and O_2/O_3 partial pressures were determined via a nude ionization gauge that was placed at the substrate position prior to growth. The beam pressure of O_3/O_2 mixture was varied between 5×10^{-6} and 5×10^{-4} mbar, controlled by a leak valve between the ozone generator and the chamber. The Zn and Mg pressure was varied between 5×10^{-7} and 4×10^{-6} mbar. The substrates were Si wafers with native SiO_2 terminating the surface. No effort was made to remove the native oxide or to terminate the surface with hydrogen. Site-selective nucleation and growth of ZnO was achieved by coating Si substrates with Ag islands. For thick Ag, a continuous ZnO film could be deposited. For nominal Ag film thickness of 20–200 Å, discontinuous Ag islands are realized. Typical growth times for ZnO on the Ag-coated silicon was 2 hrs with growth temperatures ranging from $T_g = 300$ to $500 \,°C$. After growth, the samples were evaluated by x-ray diffraction, scanning electron microscopy (SEM), transmission electron microscopy (TEM), and photoluminescence.

4.3 Results and Discussion

4.3.1 Bimodal Growth of Cored ZnO/$Zn_{1-x}Mg_xO$ Heterostructured Nanowires

Site-selective nucleation and growth of cored nanowires were achieved by coating Si substrates with Ag islands. For a nominal Ag film thickness of 20 Å, discontinuous Ag islands are realized. On these small metal catalyst islands, (Zn,Mg)O nanowires were observed to grow. Figure 4-1 shows FE-SEM images of (Zn,Mg)O nanowires on a Ag-patterned substrate grown in a Zn pressure of 3×10^{-6} mbar, a Mg pressure of 4×10^{-7} mbar, and an O_2/O_3 pressure of 5×10^{-4} mbar. The growth temperature was 400˚C. The Mg flux was, in fact, cyclically shuttered with a 60 sec. open, 60 sec. closed cycle throughout the 2 hr growth process. The net effect was to reduce the average Mg flux pressure during growth to 2×10^{-7} mbar, given that the Mg flux pressure in the open-shutter condition was 4×10^{-7} mbar. In this condition, the shape of ZnO is only cylindrical nanowire without flat whisker. Energy-dispersive spectrometry (EDS) measurement was performed on a single nanowire under the Transmission Electron Microscopy (TEM). In Figure 4-2, EDS confirmed the presence of Mg in the nanowire.

The formation of the (Zn,Mg)O nanowires includes the v-l-s mechanism described earlier, although heteroepitaxial growth occurs as well as will be seen later. Figure 4-3 shows a Z-contrast scanning transmission electron microscopy (Z-STEM) image of an individual (Zn,Mg)O nanowire grown at 400˚C, with a Zn pressure of 3×10^{-6} mbar, a Mg pressure of 2×10^{-7} mbar, and an O_2/O_3 pressure of 5×10^{-4} mbar. Evident in the image is a small particle embedded at the tip of the rod. This is similar to what is observed for other nanowire synthesis that is driven by a catalytic reaction, where catalyst particles become suspended on the nanowire tip. The diameter of the catalyst particle is ~ 6 nm.
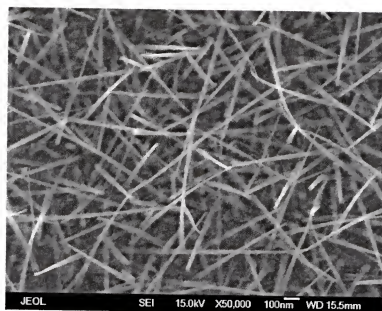
(a)

Fig. 4-1 Field-emission scanning electron microscopy of (Zn,Mg)O nanowires on Ag-coated Si with a Zn pressure of 3×10^{-6} mbar, a Mg pressure of 2×10^{-7} mbar, and an O_2/O_3 pressure of 5×10^{-4} mbar at 400°C growth temperature.
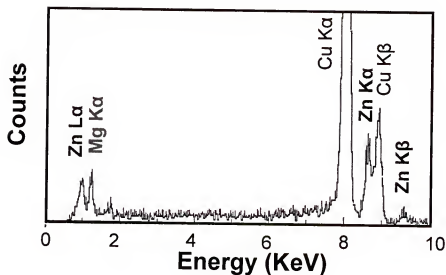

Fig. 4-2 Energy-dispersive spectrometry (EDS) measurement of a single nanowire under the Transmission Electron Microscopy (TEM).
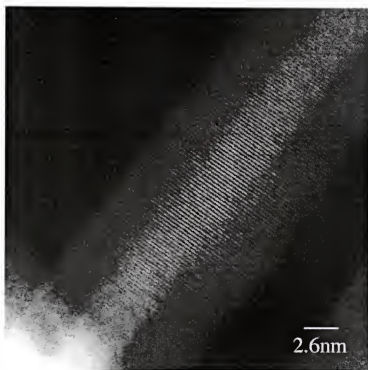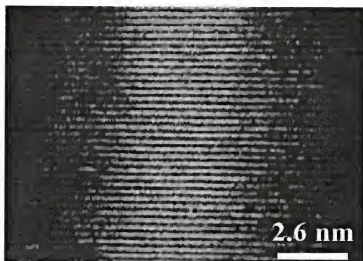
(a)

(b)

Fig. 4-3 Z-contrast scanning transmission electron microscopy (Z-STEM) image of an individual (Zn,Mg)O nanowire grown at 400˚C, with a Zn pressure of 3×10^{-6} mbar, a Mg pressure of 2×10^{-7} mbar, and an O_2/O_3 pressure of 5×10^{-4} mbar.

(a)

(b)

Fig. 4-4 High resolution Z-contrast Z-STEM image of an individual (Zn,Mg)O nanowire grown at 400˚C, with a Zn pressure of 3×10^{-6} mbar, a Mg pressure of 2×10^{-7} mbar, and an O_2/O_3 pressure of 5×10^{-4} mbar.

Note that, at the nanowire tip, the contrast in the Z-STEM image is relatively uniform, indicating uniform cation distribution. However, the wire diameter is also tapered along the length, being thicker at the base than on the tip, with an average diameter on the order of 10 nm.

Under continuous Zn, Mg, and O flux, nanowire material nucleates on the catalyst particles. However, close inspection of the nanowire structure indicates that the Zn and Mg concentrations are not uniformly distributed in the wires. Instead, there is a radial segregation from Zn-rich to Mg-rich regions, apparently reflecting differences in the solubility limits of bulk ZnO-MgO or Zn-Mg-Ag-O versus epitaxial solid solutions. In bulk material, the solubility of Mg in ZnO is relatively low, on the order of 4 at.% [88]. In contrast, Mg content as high as $Zn_{0.67}Mg_{0.33}O$ has been reported to be metastable in the wurtzite structure for epitaxial thin films. For this composition, the bandgap of ZnO can be increased to ~ 3.8 eV. For (Zn,Mg)O nanowire growth, it appears that both (hence bimodal) growth modes are relevant, but for different regions in the rod. Under low temperature MBE growth conditions, a solubility-driven segregation occurs during the catalyst-driven core formation, with the core composition determined by bulk solid solubility. Subsequently, an epitaxial sheath grows with Mg content and crystal structure determined by epitaxial stabilization. The net result is the growth of (Zn,Mg)O nanowires that are not uniform in composition across the diameter, but distinctly cored. Figure 4-4 shows a high resolution Z-STEM image of a nanowire grown under the conditions described. The lattice image for the nanowire specimen indicates that the nanowire is crystalline with the wurtzite crystal structure maintained throughout the cross-section. The c axis is oriented along the long axis of the rod. The higher contrast

for the center core region clearly indicates a higher cation atomic mass. The structures consist of a zinc-rich $Zn_{1-x}Mg_xO$ core (small x) surrounded by a $Zn_{1-y}Mg_yO$ (large y) sheath containing higher Mg content.

In an effort to further delineate the mechanisms responsible for cored nanowire growth, material was deposited with either continuous Mg flux, or under conditions where the Mg flux was cycled on and off during growth. If the sheath formation occurred simultaneously with core formation at the catalyst particle, longitudinal modulation of Mg content along the rod length would be evident for the sheath due to interrupted Mg flux. However, if the mechanisms for core and sheath growth were decoupled, with the sheath growing continuously on the core walls after core formation occurs, then the sheath composition would show no longitudinal modulation of Mg content. It might show radial multi-layer modulation of cation content, given an open shutter time that is at least sufficient for the deposition of a single monolayer on the nanowire wall. For the nanowires shown in Figures 4-3 and 4-4, the Mg flux was, in fact, cyclically shuttered with a 60 sec. open, 60 sec. closed cycle throughout the 2 hr growth process. The shuttering of Mg flux for the 60 sec interval produced no measurable longitudinal or radial modulation of Mg content. The net effect was to reduce the average Mg flux pressure during growth to 2.5×10^{-7} mbar, given that the Mg flux pressure in the open-shutter condition was 4×10^{-7} mbar. The radial segregation of cations that is observed occurs regardless of whether the Mg flux is delivered continuously or in a 60 sec pulsed mode. Obviously, a much longer cycle time should yield additional radial segregation within the sheath. It should be noted that, for higher Mg fluxes, the sheath reverts to the

(Zn,Mg)O rock-salt structure as is reported for epitaxial (Zn,Mg)O film growth. Details of cored nanowires with higher Mg content will be reported later.

In order to delineate the core composition, assess crystalline quality, and investigate possible quantization effects, the optical properties of the cored nanowires were examined using photoluminescence. Spectra were taken over the temperature range 6 K – 300 K. A He-Cd (325 nm) laser was used as the excitation source. For the low temperature measurements, the sample was cooled using either a helium flow or closed cycle cryostat. Figure 4-5 shows the photoluminescence spectra taken at various temperatures for the cored nanowire specimens shown in Figure 4-4. For ZnO nanowires (no Mg), the photoluminescence results are consistent with luminescence reported for near band edge emission in crystals [89], epitaxial films [90] and larger diameter ZnO nanowires [58]. The free exciton emission dominates luminescence, with a room temperature peak at 3.30 eV. At room temperature, the spectra for the cored (Zn,Mg)O nanowires is also dominated by the free exciton luminescence. However, the peak in luminescence at room temperature is at 3.35 eV, which is blue shifted relative to that seen in pure ZnO (peak at 3.30 eV). As the temperature is decreased, the free exciton emission shifts to higher energy due to the temperature dependence of the bandgap. At the lower temperatures, the donor-bound exciton (D^0,X) dominates luminescence [90]. Also seen at low temperatures is a peak at 3.35 eV, which is assigned to the corresponding longitudinal optical phonon replica (D^0,X)-LO. At lower energies, at least four relatively weak peaks are also observed in the visible spectrum, indicated by arrows in the figure. Similar peaks have been reported elsewhere for bulk and thin-film ZnO materials [89,90]
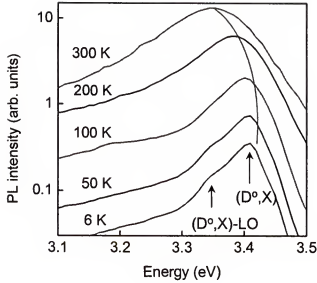
(a)
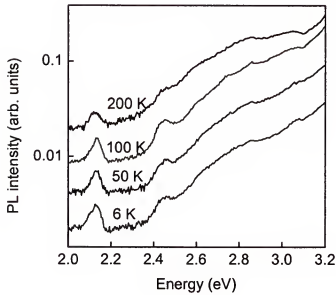
(b)

Figure 4-5 Photoluminescence spectra taken at various temperatures for the cored nanowires grown at 400˚C, with a Zn pressure of 3×10^{-6} mbar, a Mg pressure of 2×10^{-7} mbar, and an O_2/O_3 pressure of 5×10^{-4} mbar.

Blue shifts in the near band edge luminescence for nanoscale semiconducting structures can reflect quantum confinement effects. With a bandgap range of 3.2 to 3.8 eV, the ZnO/(Zn,Mg)O heterostructure system affords the opportunity to realize electron confinement due to band offsets. In semiconductors, the onset of reduced dimensionality effects should be observable for structures with dimensions below the relevant length scales. Ballistic transport becomes relevant in structures with dimensions on the order of the carrier mean free path. For ZnO, with an effective mass of ~ $0.24m_e$, the mean free path is on the order of 35 Å. Quantization of the electron states should be observable for low dimensional structures with length scales on the order of the exciton Bohr diameter [91,92]. A significant blue shift in the near-band edge emission was previously observed for InP nanorods with diameters approaching that of the exciton diameter [93]. For ZnO, the exciton Bohr diameter is 34 Å, which is approximately equal to the core diameters considered. In previous work on ZnO, shifts in the near-band edge photoluminescence peak energy have been observed for 0-D nanoparticles with diameters on the order of 2-6 nm [94]. For 2-D confinement in ZnO/(Zn,Mg)O superlattices, quantum confinement effects are predicted for well widths less than ~ 5 nm, and are reported for ZnO layer thicknesses less than ~ 4 nm [92]. For example, ZnO/(Zn,Mg)O superlattices with a ZnO well width of 3.1 nm show a 50 meV blue shift in near-band edge luminescent peak energy [91]. In the present work, a 50 meV shift is observed for the 1-D nanowire cored structure, the core diameter (4 nm) being roughly equivalent to the bulk exciton diameter (3.4 nm). While a blue shift in near-edge emission is consistent with expected quantum confinement in 4 nm diameter ZnO cores, one cannot easily differentiate this from a similar blue shift that would result from a few percent doping of Mg in the core regions.

In an attempt to address this, we have also examined the dependence of photoluminescence on Mg flux used during growth. The room temperature photoluminescence spectra for the (Zn,Mg)O nanowire samples grown at 500˚C in different Mg fluxes were measured. Figure 4-6 shows the near-band edge peak energy as a function of Mg pressure. At the higher Mg flux, the outer sheath grows as the rock-salt cubic phase as noted earlier. Nevertheless, for a wide range of Mg flux rates, the emission peak saturates at a value corresponding to that of $Zn_{0.98}Mg_{0.02}$ based on the behavior of epitaxial (Zn,Mg)O films.
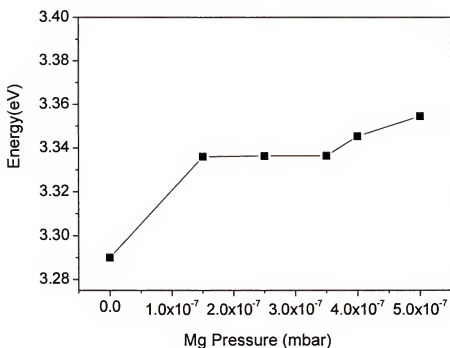

Fig. 4-6 Dependence of near band emission energy peak from cored (Zn,Mg)O nanowires versus Mg pressure.

4.3.2   Radial Heterostructure of a Core ZnO Nanowire surrounded by a (Mg,Zn)O Sheath

Under continuous Zn, Mg, and O_3/O_2 flux, the ZnO/(Mg,Zn)O nanowires

nucleated uniformly on the catalyst-coated substrate. Figure 4-7 shows a SEM image of

ZnO/MgO nanowires grown on a Si wafer that was coated with a nominally 2nm thick

layer of Ag. The Ag was deposited using e-beam evaporation. The image is from radial

heterostructured ZnO/(Mg,Zn)O nanowires grown with a Zn pressure of 3×10^{-6} mbar, a

Mg pressure of 4×10^{-7} mbar, and an O_2/O_3 pressure of 5×10^{-4} mbar. The growth

temperature was 400 °C.   Under these conditions, nanowires were observed only on the

Ag. No growth occurred on the regions of the SiO_2-terminated Si surface that was devoid

of Ag. The length of the ZnO/(Mg,Zn)O nanowire is in excess of 2 μm.

A schematic diagram of a radial heterostructured ZnO/(Mg,Zn)O nanowire is

drawn in Figure 4-8. It consists of a ZnO core and a (Mg,Zn)O sheath. The morphology

and microstructure of ZnO/(Mg,Zn)O nanowires were analyzed by TEM. Figure 4-9 (a) is

a TEM image of a nanowire, showing a difference in brightness intensity between core

and sheath regions.   This image was obtained without the objective aperture to minimize

any diffraction contrast. The contrast across the diameter of the nanowire is

predominantly mass contrast, reflecting a difference in average atomic number (Z) of the

core and sheath region. The darker core region contains more Zn than the lighter sheath

region. Selected-area diffraction (SAD) taken from this single nanowire in Figure 4-9 (b)

shows that the nanowire consists of two different crystal structures. The single crystal

diffraction pattern corresponds to the hexagonal wurtzite structure. Based on the mass

contrast discussed earlier, this is the ZnO-rich core. The ring diffraction pattern that is

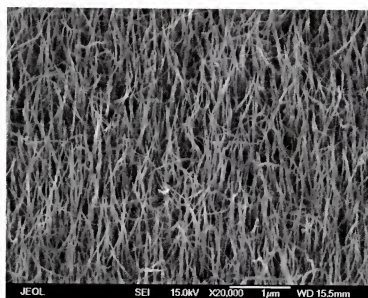observed corresponds to a cubic rock salt structure with a d-spacing similar to that for

Fig. 4-7 Field-emission scanning electron microscopy of (Zn,Mg)O nanowires on Ag-coated Si with a Zn pressure of 3×10^{-6} mbar, a Mg pressure of 4×10^{-7} mbar, and an O_2/O_3 pressure of 5×10^{-4} mbar at 400°C growth temperature.
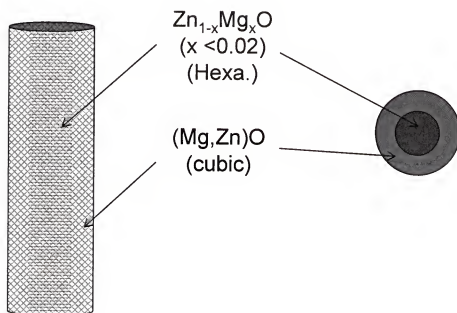

$Zn_{1-x}Mg_xO$
(x <0.02)
(Hexa.)

(Mg,Zn)O
(cubic)

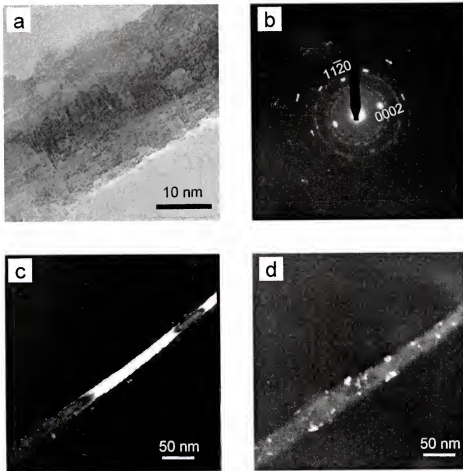Figure 4-8. A schematic diagram of a radial heterostructured (Zn,Mg)O/(Mg,Zn)O nanowire.

Fig.4-9 Radial heterostructure of ZnO/MgO nanowire, (a) TEM image of nanowire showing a difference in brightness intensity between core and sheath region. (b) Selected-area diffraction(SAD) from the nanowire that consists of two different crystal structures, (c) Dark field image taken from the diffraction spot of the wurzite structure showing core ZnO of nanowire. (d) a DF image from the ring diffraction pattern of the rock salt structure showing the MgO sheath.

MgO. The first, second, and third ring correspond to the {111}, {200}, and {220} d-spacing of the rock salt (Mg,Zn)O structure, respectively. A dark field (DF) image shown Figure 4-9 (c), formed from the (0 0 0 2) diffraction spot of the wurtzite structure, yields intensity corresponding only to the core part of the nanowire. The discontinuous brightness of the core ZnO along the nanowire results from bending of the nanowire. Clearly, the center core of the nanowire is hexagonal wurtzite ZnO, with the sheath material not exhibiting this structure. Figure 4-9 (d) shows a DF image formed from the {111} ring of the rock salt structure. The image includes the entire volume of the nanowire, indicating that it comes from the nanowire sheath.
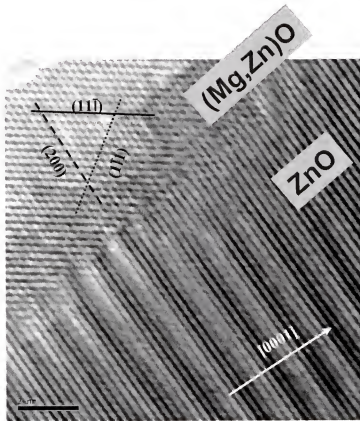

Fig. 4-10 High resolution transmission electron microscopy of ZnO and (Mg,Zn)O interface; (Mg,Zn)O sheath in upper-left region, ZnO core in lower-right region.
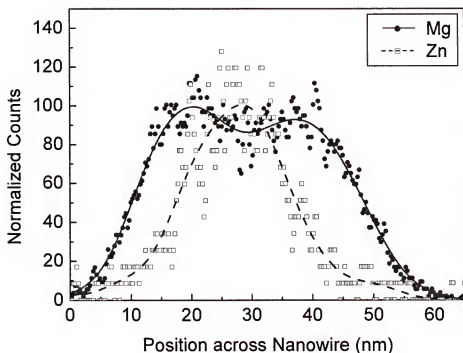
Figure 4-11 Compositional line-scan across the ZnO/(Mg,Zn)O nanowire probed by STEM EDS spectroscopy.

Therefore, the core of this wire is ZnO having the wurtzite structure. The surrounding sheath is (Mg,Zn)O having the rock salt structure.

High resolution transmission electron microscopy was also performed on the interface region between the ZnO core and (Mg,Zn)O sheath. The image shown in Figure 4-10 indicates a radial heterostructured nanowire in which the interface between the sheath and core is epitaxial despite the discontinuity in the crystal structure and symmetry. The lower-right region of the image is the core, while the upper-left region is the sheath. Growth of the core yields the rod axis along the c-axis direction of the hexagonal ZnO. For the (Mg,Zn)O sheath, the (2 0 0), (1 $\bar{1}$ 1), and (1 1 $\bar{1}$) planes match those of the rock

salt structure, according to the lattice spacing and angle between planes. Note that the lattice mismatch between the (Mg,Zn)O (2 0 0) plane and the ZnO (0 0 0 2) plane produces regularly-spaced interfacial edge dislocations.

In order to further delineate the structure of these nanowire heterostructures, the compositional distribution of Mg and Zn in a single ZnO/(Mg,Zn)O nanowire was examined by energy-dispersive spectrometry using the electron beam in the STEM. Figure 4-11 plots the intensity of the Mg $K_{\alpha 1}$, Zn $K_{\alpha 1}$, and O $K_{\alpha 1}$ peaks across the nanowire. The compositional line-scan clearly shows a radial segregation of the Zn and Mg cation. Note that the spatially-varying spectra always include irradiation of the sheath region. Hence, the Mg intensity does not drop to zero when irradiating the center. However, in the core region, there is a clear drop in Mg intensity along with a corresponding increase in Zn intensity. This result unambiguously supports the radial segregation of Zn and Mg, forming a ZnO core and a (Mg,Zn)O sheath.

The growth of the ZnO/(Mg,Zn)O nanowires is a catalysis-driven reaction similar to ZnO nanowire growth using catalysis-driven molecular beam epitaxy reported earlier [95]. Initially, the core ZnO was nucleated on Ag with the reaction of Zn and Oxygen source. It should be noted that uncored Mg nanowires with rock-salt structure throughout the wire were not observed for growth on the Ag coated Si wafer when only Mg and O_3/O_2 is used. At the selected growth conditions, Ag could not act as effective catalyst for growth of cubic MgO nanowire. According to the phase diagram between ZnO and MgO, MgO allows a maximum of 56% ZnO at 1600°C and maintains its rock salt structure with a lattice constant close to that of pure MgO [29]. In the case of ZnO, the solid solubility of Mg is limited to only 2% maximum while keeping its hexagonal structure. In thin film
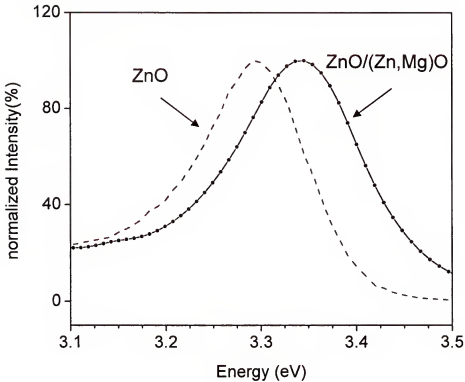
Figure 4-12 Comparison of band-edge photoluminescence for ZnO and (Zn,Mg)O nanowires.

growth, a nonequilibrium phase can be obtained up to 36% Mg solubility in ZnO using pulsed laser deposition [96]. However, ZnO/(Mg,Zn)O heterostuctured nanowire synthesis appears to follow equilibrium growth according to the phase diagram.

In order to further elucidate the optical properties, photoluminescence of the cored ZnO nanowires were measured. This measurement was performed at room temperature with a He-Cd laser as the excitation source. The comparison of band-edge photoluminescence between pure ZnO nanowires and cored ZnO nanowires shows a 50 meV blue shift in Figure 4-12. As previously reported, a 50 meV blue shift in the near-band luminescent peak energy of cored ZnO compared to that of ZnO nanowires could indicate approximately 2 at % Mg solubility in core-ZnO nanowire[97]. However, this

radial heterostructured nanowire could also produce quantum confinement, as the bandgap of (Mg,Zn)O is much larger than that of ZnO. The size variation in the diameter of the ZnO core is currently being explored to investigate the quantum confinement effect of the cored ZnO/(Mg,Zn)O nanowire structure.

4.3.3 (Mg,Zn)O Nanowires

Homostructured (Mg,Zn)O nanowires are observed at a higher Mg pressure than that for heterostructural ZnO/(Mg,Zn)O nanowires. Figure 4-13 shows SEM images of (Mg,Zn)O nanowires grown on both Si and Al_2O_3 substrates that were coated with a nominally 2nm thick layer of Ag. (Mg,Zn)O nanowires were grown with a Zn pressure of 3×10^{-6} mbar, a Mg pressure of 8×10^{-7} mbar, and an O_2/O_3 pressure of 5×10^{-4} mbar. The growth temperature was 400 °C. Under these conditions, nanowires were observed only on the Ag sites. No growth of nanowires occurred on the regions of the SiO_2-terminated Si surface and Al_2O_3 that was devoid of Ag. The length of the (Mg,Zn)O nanowires were in excess of 2 µm. The shape and length of (Mg,Zn)O nanowires does not show any dependence on substrate type. Figure 4-13 (a) and (b) show the preferred growth orientation of (Mg,Zn)O grown on Al_2O_3 substrates coated with 2nm Ag. (Mg,Zn)O nanowires make an angle of approximately 60° each other. This indicates that epitaxial [100] oriented (Mg,Zn)O is obtained on (0001) c-plane Al_2O_3. The growth direction of (Mg,Zn)O is confirmed by TEM analysis that will be discussed later.

X-ray diffraction of the deposited materials confirms that the nanowires are MgO of a rock salt structure. Figure 4-14 shows X-ray diffraction patterns taken along the surface normal, indicating only MgO peaks on both Si and Al_2O_3 substrates. The

diffraction pattern of the nanowires is consistent with randomly oriented polycrystalline material of MgO, although selected area electron diffraction (discussed below) indicates a preferred <100> orientation of individual nanowires along the long axis. No second phase or segregation are observed in Figure 4-14.

The composition of nanowire is investigated by energy-dispersive spectrometry (EDS) with TEM. In the Figure 4-15, a compositional line-scan, profiled across the nanowire, by EDS with STEM shows the presence and compositional distribution of Mg and Zn in the single nanowire. The Mg $K_{\alpha 1}$, Zn $K_{\alpha 1}$, and O $K_{\alpha 1}$ peaks are used to identify the nanowire composition. This analysis indicates that Mg, Zn, and O are uniformly distributed through out the nanowire. The content of Mg in the nanowire is much higher than that of Zn. According to the phase diagram between ZnO and MgO, MgO allows a maximum of 56 wt% ZnO at 1600°C and maintains its rock salt structure with a lattice constant close to that of pure MgO [29]. Therefore, Zn will exist in MgO nanowire as a solid solution keeping the cubic rock salt structure.

The (Mg,Zn)O nanowires have two different shapes, mainly squire cylinders and needles. Figure 4-16 shows a transmission electron microscopy image and selected area diffraction of squire cylinder of (Mg,Zn)O nanowire indicating a single crystal structure. An estimate of the rod thickness is 90 nm. The length of the (Mg,Zn)O nanowire is in excess of 2 μm. A selected area diffraction pattern of a nanowire specimen, taken from [001] zone axis shown in Figure 4-16 (d), clearly shows that the nanowire has a cubic rock salt crystal structure. Also, the high resolution TEM image in Figure 4-16 (d) confirms the single-phase cubic rock salt structure of (Mg,Zn)O and the growth direction of [100]. High resolution transmission electron microscopy and selected area diffraction

as shown in Figure 4-17 prove that the needle shaped (Mg,Zn)O nanowires have the same

cubic rock salt structure as the square cylinder (Mg,Zn)O nanowires having a [100]
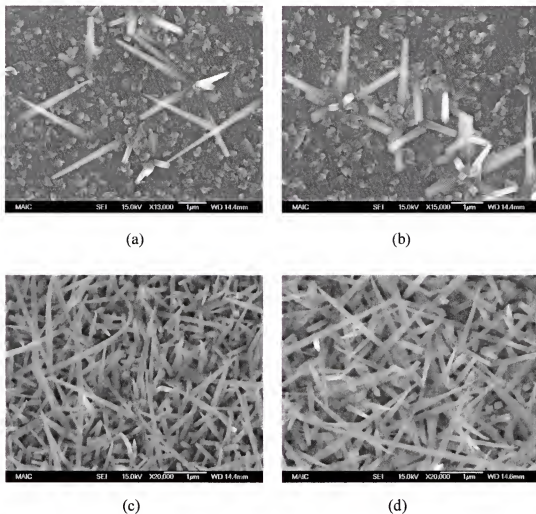
growth direction.

(a)   (b)

(c)   (d)

Figure 4-13 SEM images of (Mg,Zn)O nanowires grown on (a), (b), (c) Al$_2$O$_3$ and
(d) Si substrates that were coated with 2nm thickness of Ag. (Mg,Zn)O nanowires
were grown with a Zn pressure of 3×10^{-6} mbar, a Mg pressure of 8×10^{-7} mbar,
and an O$_2$/O$_3$ pressure of 5×10^{-4} mbar.
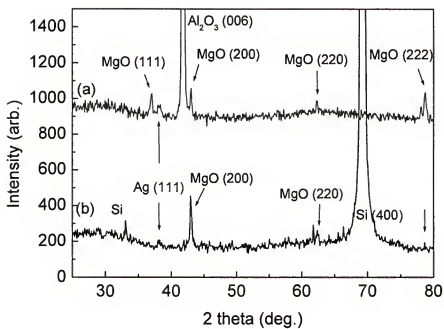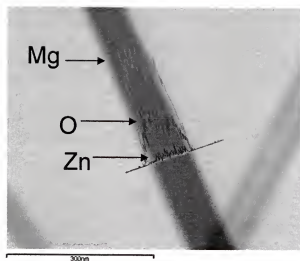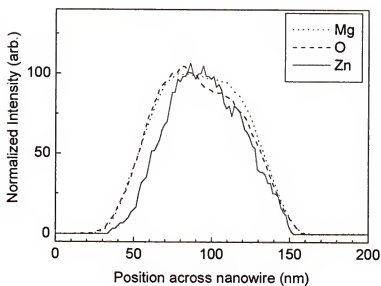
Figure 4-14 X-ray diffraction patterns taken along the surface normal, indicating only MgO peaks on both Si and Al$_2$O$_3$ substrates.

(a)

(b)

Figure 4-15 Compositional line-scan across the MgO nanowire probed by STEM EDS.

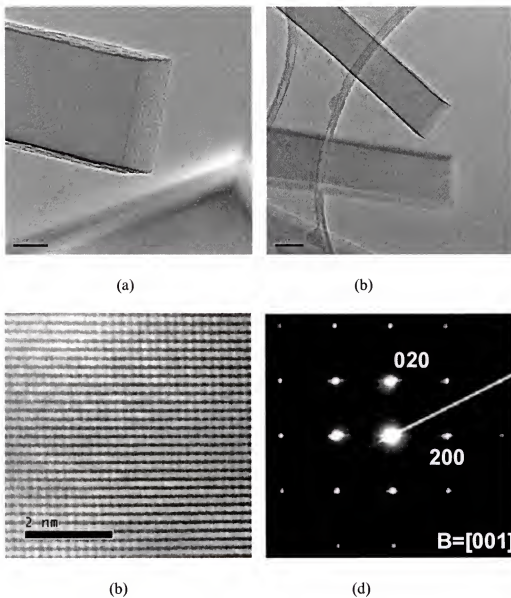(a)   (b)

(b)   (d)

Figure 4-16 (a) and (b)Transmission electron microscopy images of (Mg,Zn)O nanowire. (c) High resolution TEM image and (d) selected area diffraction of (Mg,Zn)O nanowire specimens taken from [001] zone axis.

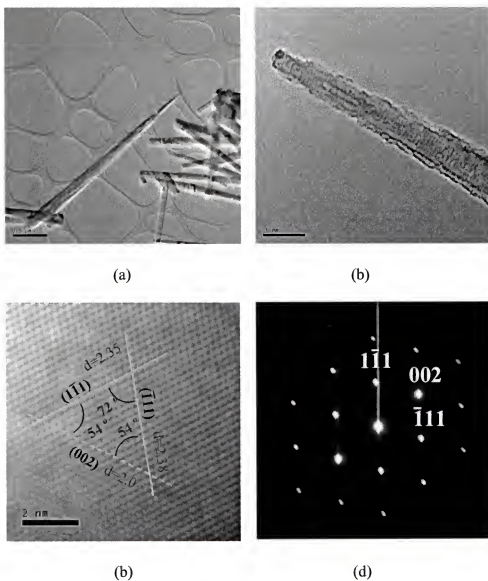(a)　　　　　　　　　　　　(b)

(b)　　　　　　　　　　　　(d)

Figure 4-17 (a), (b) Transmission electron microscopy images of (Mg,Zn)O nanowire. (c) HR TEM image and (d) selected area diffraction of (Mg,Zn)O nanowire specimens taken from [110] zone axis.

CHAPTER 5

EFFECT OF PHOSPHORUS DOPING ON ZnO THIN FILM GROWN BY PULSD LASER DEPOSITION

5.1 Introduction

Relative to the work on nitrogen doping, very few studies have considered other group V ions for substitutional doping on the O site. There is a large ionic radii mismatch for P (2.12 Å), As (2.22 Å), and Sb (2.45 Å) on the O (1.38 Å) site, suggesting limited solid solubility for these anions. Nevertheless, p–n junction-like behavior has been reported between an n-type ZnO substrate and a surface layer that was heavily doped with phosphorus [98]. Activation of the P dopant was achieved via laser annealing of a zinc phosphide-coated ZnO single crystal. A related result was reported for epitaxial ZnO films on GaAs subjected to annealing [99]. In this case, a p-type layer was reportedly produced at the GaAs/ZnO interface. Further understanding of group V substitution in ZnO requires the study of doped materials that are free from complications of reactive substrates or interfacial layers.

In this chapter, the doping behavior of phosphorus in ZnO epitaxial film was investigated. The effects of annealing on doping and optical properties of epitaxial phosphorus doped ZnO were studied. The magnetic properties of phosphorus doped ZnO were examined after high dose Mn implantation. The characteristics of metal-insulator-semiconductor (MIS) and junction thin-film device structures utilizing phosphorus-doped ZnO materials are examined to delineate the carrier type in this material.

5.2 Experimental

Pulsed laser deposition was used for film growth. Phosphorus-doped ZnO targets were fabricated using high-purity ZnO (99.9995%), with P_2O_5 (99.998%) serving as the doping agent. The targets were pressed and sintered at 1000 °C for 12 h in air. Targets were fabricated with phosphorus doping levels of 0, 1, 2, and 5 at. %. Figure 5-1 is a schematic diagram of the pulsed laser deposition system. A KrF excimer laser was used as the ablation source. A laser repetition rate of 1 Hz was used, with a target to substrate distance of 4 cm and a laser pulse energy density of 1–3 J/cm^2. The ZnO growth chamber exhibits a base pressure of 10^{-6} Torr. Single crystal (0001) Al_2O_3 (sapphire) was used as the substrate material in this study. The substrates were attached to the heater platen using Ag paint. Film thickness ranged from 300 to 1000 nm. Film growth was performed over a temperature range of 300–500 °C in an oxygen pressure of 20 mTorr. The transport
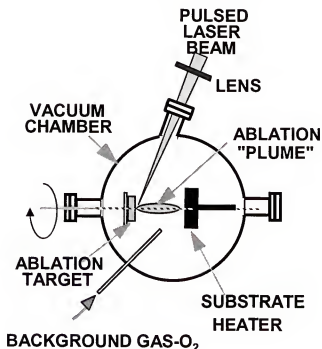

Fig. 5-1 A schematic diagram of pulsed laser deposition chamber.

properties of annealed P-doped ZnO epitaxial films were compared with undoped films grown and annealed under the same conditions. Annealing was carried out at temperatures ranging from 400 to 700 °C in a 100 Torr O_2 ambient for 60 min. Four-point van der Pauw Hall measurements were performed to determine transport properties.

5.3 Result and discussion

5.3.1 Transport Properties of Phosphorus Doped ZnO

5.3.1.1 Shallow Donor Formation

The technique used for film synthesis, namely pulsed-laser deposition, possesses several favorable characteristics for growth of multicomponent materials, including stoichiometric transfer of target material to the substrate, compatibility with a background gas, and atomic level control of the deposition rate. In this film-growth technique, a
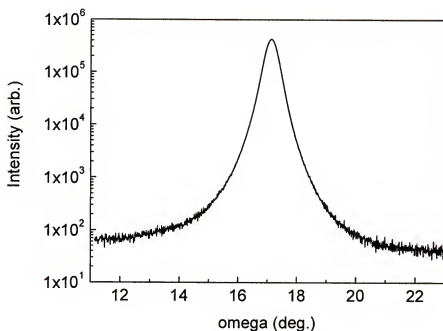

Fig. 5-2 Rocking Curve through (0002) plane of ZnO grown on c-plane Al_2O_3 with an O_2 pressure of 20 mTorr at 400°C.
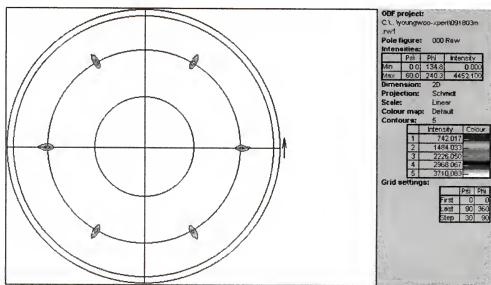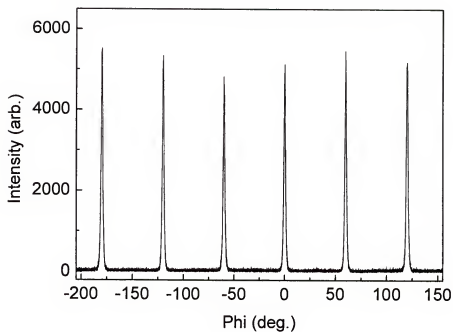
Fig. 5-3 φ scan through (0002) plane (top) and pole figure (bottom) of ZnO grown on c-plane Al_2O_3 with an O_2 pressure of 20 mTorr at 400°C.

focused laser pulse is directed onto a target of material in a vacuum chamber. The laser pulse locally heats and vaporizes the target surface, producing an ejected plasma or plume of atoms, ions, and molecules. The plume of material is deposited onto an adjacent substrate to produce a crystalline film. The crystallinity of the ZnO film grown with an O_2 pressure of 20mTorr at 400°C growth temperature on c-plane Al_2O_3 was investigated by four-circle x-ray diffraction. The rocking curve through the (0002) plane of ZnO shown in Figure 5-2 has a full with half maximum (FWHM) of 0.429°. Only the c-axis ZnO peaks are evident in the plot of θ-2θ scan along the surface normal for the ZnO film. ϕ scans and Pole figure through the ZnO ($10\bar{1}1$) plane in Figure 5-3 show in-plane alignment with $\Delta\phi = 1.93°$ and a sixfold symmetry of the plane.
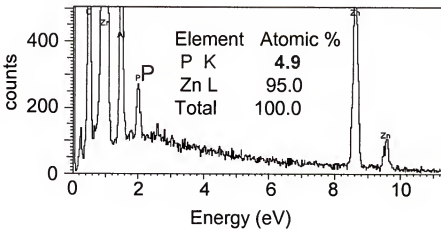

Fig. 5-4 Energy dispersive spectrometry spectrum for an as-deposited ZnO film grown from an ablation target containing 5 at.% phosphorus.

Despite the anticipated stoichiometric transfer of doped material from the target to the substrates, measurements were needed to verify the phosphorus content in the films.

Both P and P_2O_5 sublime at relatively low temperatures (416°C and 360°C, respectively), making it unclear that the films deposited at elevated temperatures would retain the phosphorus content of the ablation targets. To examine this issue, the phosphorus content of the films was measured using energy-dispersive spectrometry (EDS). Figure 5-4 shows an EDS spectrum for a film grown from an ablation target with a nominal phosphorus content of 5 at.%. The film was deposited at 400°C in oxygen ambient of 20 mTorr. Despite the relatively high growth temperature, the phosphorus content was, in fact, replicated in the film within the experimental accuracy of EDS. The EDS spectrum of the film shows a phosphorus content of 4.9 at.% for growth from a 5 at.% phosphorus-doped target. Similar results were obtained for the 1 and 2 at.% doped targets.

X-ray diffraction was used to examine the crystallinity of the phosphorus-doped ZnO films relative to undoped ZnO films. Based on the bulk phase diagram for ZnO–P_2O_5, the solid solubility of phosphorus in ZnO should be limited. Indications that the solid solubility has been exceeded in the films would be the appearance of impurity phases or a saturation of the lattice parameter with increasing doping. Figure 5-5 (a) shows the X-ray-diffraction data for films grown on (0001) Al_2O_3 at 400°C in oxygen ambient of 20 mTorr with various phosphorus concentrations. The diffraction data shows only ZnO and substrate peaks. The films are oriented in-plane and out of-plane, with the (0001) ZnO direction parallel to the surface normal. A decrease in diffraction intensity is observed as the phosphorus content increases from 1 to 5 at%. In particular, the diffraction intensity of the ZnO (0002) peak for the 2 and 5 at% P-doped films is measurably lower than that for the 1 at% doped sample. This degradation in crystallinity may indicate that the phosphorus-doping levels are exceeding the solid solubility limit.
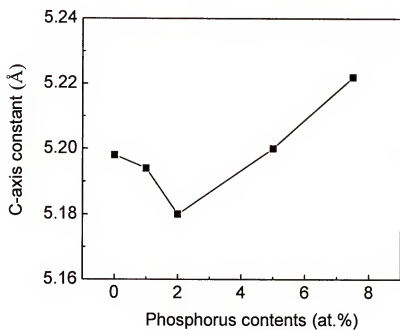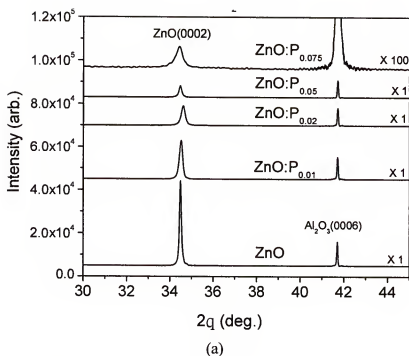
(a)

(b)

Fig. 5-5 X-ray diffraction scans through the surface normal for ZnO films grown with various phosphorus contents. The figure includes (a) data over wide range of angle showing no apparent impurity peaks, and (b) c-axis constant as a function of phosphorus content using the ZnO (0002) peaks, indicating a shift in lattice spacing with increasing phosphorus content.
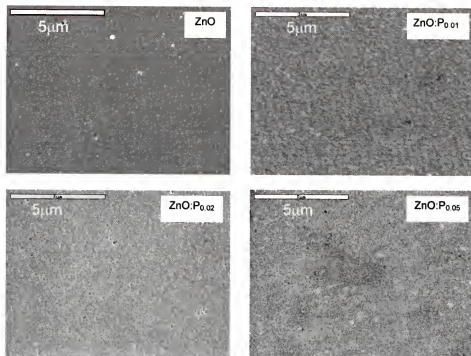
Fig. 5-6 Scanning electron microscope image of ZnO films with varying P content.

However, no secondary phases are observed in the diffraction patterns. In addition, the diffraction data show a continuous shift in lattice spacing with increasing phosphorus content up to 2 at%, although the dependence on P content is not monotonic. As seen in Figure 5-5 (b), the *c*-axis parameters for the ZnO: $P_{0.01}$ and ZnO: $P_{0.02}$ films are smaller than that for the undoped film. Based on comparison of ionic radii for P^{-3} and O^{-2}, one would expect an increase in lattice spacing with substitution on the group-VI site. However, as phosphorus is increased to 5 at%, the c axis increases. The initial decrease in *c* axis with P doping suggests substitution on the Zn site and/or a complex formation involving interstitials. The systematic near-linear increase in lattice spacing in going from 2 at% to 5 at% is consistent with a competing substitution of P on the oxygen site at the

higher doping levels. Note, however, that strain can also result in lattice-spacing shifts for thin films. In order to further address the possibility that secondary phases result from P substitution, the surface morphology of the deposited films was investigated using scanning electron microscopy (SEM). Figure 5-6 shows the SEM micrographs of films grown with various phosphorus contents. Little change in morphology is observed with no evidence of secondary phase precipitates. The micrographs are for films grown at 400°C in 20 mTorr of O_2.

Hall measurements were performed on the as-deposited films in order to delineate the doping behavior of phosphorus in ZnO. In all cases, the inclusion of phosphorus in the ZnO films yields a significant increase in electron density, resulting in as-deposited films that are highly conductive and *n*-type. Figure 5-7 shows the resistivity as a function of deposition temperature for ZnO : $P_{0.01}$ films grown at 20 mTorr and 200 mTorr O_2. The resistivity increases from $\sim 1.5 \times 10^{-3}$ Ω-cm to 10^{-2} Ω-cm as the deposition temperature increases from 300°C to 500°C. No discernable shift in lattice spacing is observed as the growth temperature increases based on X-ray-diffraction scans through the surface normal. Yet, the film resistivity increases with increasing deposition temperature. Four-point Van der Pauw Hall measurements indicate that the increased resistivity with growth temperature is due to a reduction in carrier density with little change in mobility. Figure 5-8 shows the Hall mobility and carrier density for ZnO: $P_{0.01}$ films grown over a temperature range of 300°C to 500°C. Note that the open symbols are for films grown at 200 mTorr O_2, with the closed symbols representing film growth at 20 mTorr. The Hall coefficients are negative in sign, indicating *n*-type material. The Hall mobility of 18–20 cm^2/V-s is comparable to that for undoped ZnO films grown by pulsed-laser deposition
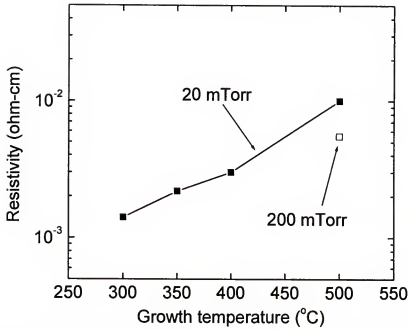
Fig. 5-7 Room temperature resistivity as a function of growth temperature for ZnO: $P_{0.01}$ films grown at 20 mTorr or 200 mTorr.
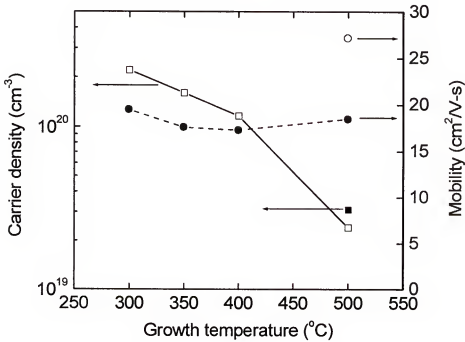

Fig. 5-8 Carrier density and Hall mobility for ZnO:$P_{0.01}$ films grown at 20 mTorr (closed symbols) or 200mTorr (open circle).
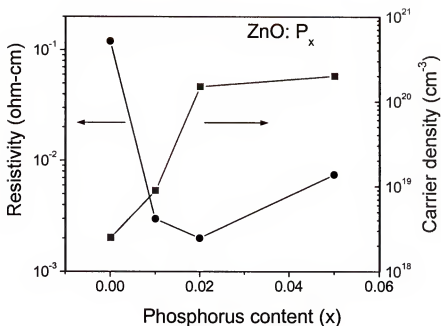
Fig. 5-9 Resistivity and carrier density for as-deposited ZnO: P films with various phosphorus contents. The films were grown at 400°C.

under similar conditions. The decrease in the carrier density as the growth temperature increases suggests that the donor defect may be relatively unstable. In all cases considered, the electron carrier density for the as-deposited phosphorus-doped films is significantly higher than that for the undoped ZnO film grown under the same conditions. This is clearly evident in Figure 5-9, showing the resistivity and carrier density as a function of phosphorus content for films grown at 400°C in 20 mTorrO$_2$. In particular, the carrier density increases from 2×10^{18} cm^{-3} for undoped films to 2×10^{20} cm^{-3} for 5 at% P doping. Note that the resistivity drops by nearly two orders of magnitude for the same variation in phosphorus content. Simple arguments for ionic substitution of P (group V) on the oxygen site (group VI) would predict *p*-type doping. Yet, an increase in *n*-type conductivity with phosphorus doping is observed. Clearly, the doping behavior of
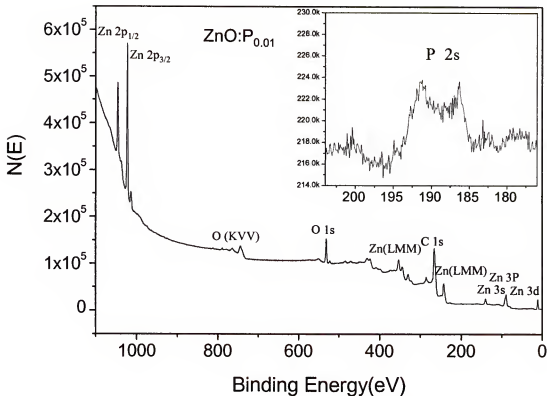
Fig. 5-10 X-ray photoelectron spectrum for as-deposited ZnO: $P_{0.01}$ film.

phosphorus in ZnO is more complex than this simple model. It is interesting to note that first-principles total-energy calculations by Park et al. [100] suggest that the formation of anti-site defects is likely for P in ZnO. Phosphorus substitution on the Zn site could introduce a donor state, assuming a formal oxidation state of +3 for P on the Zn^{+2} site. It is also possible that the compensating *n*-type defect originates from a P^{+3}-, P^{+5}-, or P^{-3} -related complex. In order to investigate the local chemical bonding environment of the phosphorus in the ZnO matrix, X-ray photoelectron spectroscopy (XPS) was performed. Differentiating between P^{+5} and P^{-3} oxidation states is possible by observing the binding energy of the P $2s$ peak. A difference of approximately 6 eV in binding energy is

observed in the two valence states, as represented by Zn_3P_2 (P^{-3} with binding energy of 186.25 eV) [101] and P_2O_5 (P^{+5} with $2s$ binding energy of 192.8 eV) [102]. Figure 5-10 shows the XPS spectrum for a ZnO film doped with 1 at% P. The phosphorus $2s$ peak is clearly split, indicating a mixture of local bonding. The binding energy locations are at 192 eV and 187 eV. The peak at 187 eV is consistent with the P^{-3} $2s$ spectrum, suggesting phosphorus bonding directly to the Zn cations. However, the peak at 192 eV is indicative of a P^{-5} oxidation state as seen in P_2O_5. This indicates competing phosphorus environments and may explain the n-type behavior. Future activities will explore the stability of the phosphorus-related defect structures via annealing studies.

5.3.1.2 Deep Level Acceptor Formation

Both P and P_2O_5 sublime at relatively low temperatures (416 and 360 °C, respectively), making it possible that the films deposited and/or annealed at elevated temperatures would not retain the phosphorus content of the ablation targets. To examine this issue, the phosphorus content of the films was measured using energy dispersive spectrometry (EDS) and x-ray photoelectron spectroscopy. Figure 5-11 shows the EDS spectra for a ZnO film doped with 2 at.% phosphorus both as-deposited and after annealing at 700°C. Despite the relatively high growth and annealing temperature, the phosphorus content in the ablation target was, in fact, replicated in the film within the experimental accuracy of the two techniques.

Hall measurements were performed on both the as-deposited and annealed films in order to delineate the doping behavior of phosphorus in ZnO. For the as-deposited films, the inclusion of phosphorus yields a significant increase in electron density, resulting in

ZnO that is highly conductive and *n* type. The shallow donor behavior in the as-deposited films is inconsistent with P substitution on the O site, and presumably originates from either substitution on the Zn site or the formation of a phosphorus-bearing complex. Previous work has shown that the defect-related carrier density in nominally undoped ZnO can be reduced via high temperature annealing in oxygen or air. In the case of undoped material, the reduction in donor density is presumed due to either a reduction in
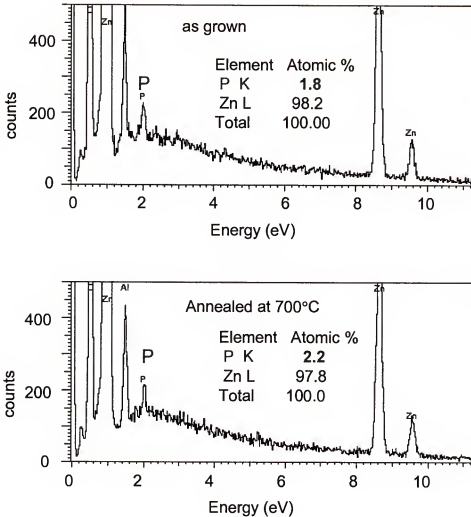

Fig. 5-11 Energy dispersive spectrometry spectrum for as-deposited and annealed ZnO film grown an ablation target containing 2 at.% phosphorus.
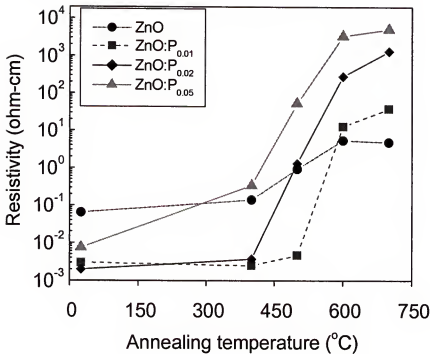
Fig. 5-12 Resistivity ZnO: P films with various phosphorus contents annealed at temperatures ranging from 400 to 700 °C. The films were grown at 400 °C.

oxygen vacancies, Zn interstitials, or perhaps outdiffusion of hydrogen that is incorporated in the ZnO lattice during synthesis [103]. In an effort to reduce electron density and elucidate the electronic nature of phosphorus doping in ZnO, annealing studies were performed. Anneals were performed on films with a nominal phosphorus content of 0, 1, 2, and 5 at. %. Figure 5-12 shows the resistivity of films annealed at various temperatures. First, note that the resistivity of the as-deposited phosphorus doped films is significantly lower than that for the nominally undoped film. The as-deposited film data is signified in Figs. 5-12 and 5-13 as samples subjected to an annealing temperature of 25 °C. For as-deposited films, a shallow donor state dominates transport. As the films are annealed at increasing temperatures, the resistivity of the phosphorus-

doped films increases rapidly. This is particularly evident for films subjected to annealing temperatures of 600 °C or higher. Note also that the increase in resistivity with annealing is more rapid in the films with higher phosphorus content. When annealed at 700 °C, the phosphorus doped ZnO films become semi-insulating with a resistivity approaching 10^4 Ωcm. The conversion of transport behavior from highly conducting to semi-insulting with annealing should be attributed to at least two factors. First, the defect associated with the shallow donor state in as-deposited films appears to be relatively unstable. This would explain the increase in resistivity, but would alone predict a saturation of resistivity at the value given by the undoped material. This does not explain why the phosphorus-doped films become significantly more resistive than undoped films subjected to the same annealing treatment. The dependence of postannealed resistivity on phosphorus content suggests that a deep level associated with phosphorus dopant is present. This is, in fact, consistent with the expected results that P substitution on the oxygen site yields a deep acceptor.

In addition to resistivity, the Hall coefficients were measured at room temperature for both the unannealed and annealed films. A Van der Pauw geometry was used for extracting Hall mobility and carrier concentration. An 8000 G magnet was utilized. Figure 5-13 shows the Hall mobility and carrier concentration for the films. Measurement data are indicated only for those cases where the Hall voltage magnitude and sign was unambiguous. For the experimental Hall measurement system used, the lower limit sensitivity for Hall mobility magnitude was on the order of 1 cm^2/V s. For all of the data shown in Figure 5-13, the Hall sign was negative, indicating n-type material. For phosphorus-doped films with resistivity greater than approximately 50 Ωcm, an
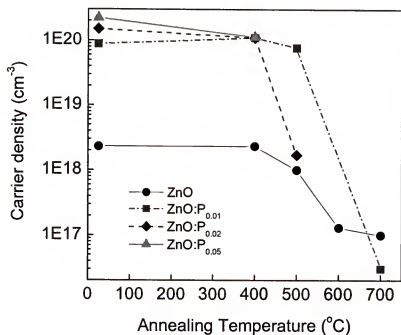
(a)
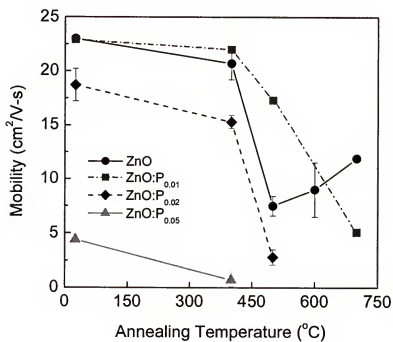
(b)

Fig. 5-13. Plots of (a) carrier density and (b) Hall mobility for phosphorus-doped ZnO films annealed at various temperatures.

unambiguous Hall voltage could not be measured. For this reason, both carrier density and Hall mobility data for some annealed samples are absent in the plots. From the measurements yielding unambiguous Hall voltage, both the carrier density and mobility in phosphorus-doped films are observed to decrease with annealing. This is consistent with a reduction in the shallow donor state density and activation of a deep (acceptor) level in the gap. Note that in all cases where an unambiguous Hall voltage was determined, the sign was negative indicating *n*-type conduction.

5.3.2 p-type behavior in phosphorus-doped (Zn,Mg)O device structures

The characteristics of metal-insulator-semiconductor (MIS) and junction thin-film device structures utilizing phosphorus-doped ZnO materials are examined to delineate the carrier type in this material. Phosphorus-doped $(Zn_{1-x}Mg_x)O$: $P_{0.02}$ (x=0, 0.05, 0.10, 0.15) targets were fabricated using high-purity ZnO (99.9995%) and MgO (99.998%), with P_2O_5 (99.998%) serving as the doping agent. Thin films were grown at 400°C with an oxygen pressure of 20 mTorr. In order to verify the Mg contents in the thin films, energy-dispersive spectrometry (EDS) was used. Figure 5-14 shows the Mg and Phosphorus contents as a function of target contents. The phosphorus content in the thin films becomes larger than that in the targets with increasing Mg content. The Mg content in thin films is similar to that in the targets below 10 at. %. At 15at.% Mg content in the target, about 30 at.% Mg content is observed in the thin films. The difference in thin film composition versus the target results from different sticking coefficients for Zn and Mg.

Figure 5-15 shows the c-axis parameter as a function of Mg content for undoped ZnO and phosphorus doped ZnO thin films. In the X-ray diffraction pattern, only

hexagonal wurtzite ZnO peaks were observed. The decrease of c-axis parameter with the increase of Mg content while keeping hexagonal structure indicates that the solid solubility of Mg can be higher than the equilibrium value from the phase diagram between ZnO and MgO [29]. The c-axis length of 2% phosphorus doped (Zn,Mg)O is smaller than that of undoped (Zn,Mg)O when Mg content is small. As Mg content increases, the c-axis length of 2% phosphorus doped (Zn,Mg)O becomes larger than that of undoped (Zn,Mg)O. As discussed earlier, the initial decrease in the *c* axis lattice spacing with P doping suggests that substitution of phosphorus on the Zn site and/or a
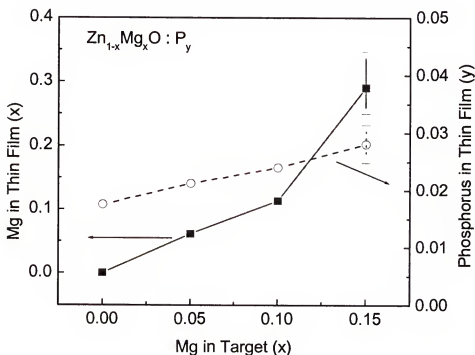

Figure 5-14 Mg and Phosphorus contents in the films grown at 400°C with oxygen pressure of 20 mTorr as a function of target contents.
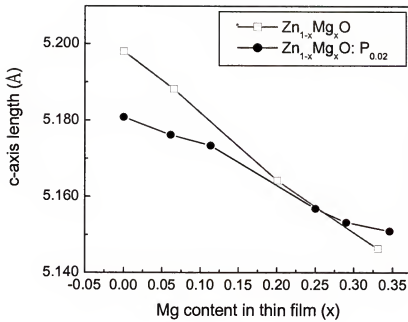
Figure 5-15 c-axis parameters as a function of Mg contents for undoped ZnO and phosphorus doped ZnO thin films grown at 400°C with oxygen pressure of 20 mTorr.

complex formation involving interstitials is occurring. However, based on comparison of ionic radii for P^{-3} and O^{-2}, the larger c-axis of 2% phosphorus doped (Zn,Mg)O in high Mg content regions indicate that the substitution rate of phosphorus on the oxygen site increases with the increase of Mg. Figure 5-16 shows that the carrier concentration of 2% phosphorus doped (Zn,Mg)O decreases and the resistivity decreases with the increase of Mg in films. However, the variation of the carrier concentration and resistivity of undoped (Zn,Mg)O is small. The mobility of both doped and undoped films, shown in Figure 5-17, decreases due to the scattering by the Mg. It suggests that the substitution of phosphorus on the oxygen site is increased by the addition of Mg, which decreases the substitution of phosphorus on the Zn-site.

For the device structures, platinum-coated Si was used as the substrate, with Pt serving as the bottom electrode. Although Pt is known to form a Schottky contact with n-type ZnO, its behavior in contact with P-doped (Zn,Mg)O is unknown. However, assuming p-type conduction in the P-doped (Zn,Mg)O material, the work function of Pt makes it a viable candidate as an ohmic contact. This geometry also minimizes the series resistance of the bottom contact, thus permitting a reasonably accurate measurement of the device properties. The substrates were attached to the heater platen using Ag paint. The P-doped (Zn,Mg)O layer thickness was on the order of 130 nm. The Mg, Zn, and P composition were measured and determined to be close to that of the ablation targets. Film growth was performed at 400 ˚C in an oxygen pressure of 20 mTorr. Previous work has shown that as-deposited phosphorus doped ZnO films are heavily n-type due to an apparent compensating donor defect. However, a moderate temperature anneal was shown to suppress that n-type behavior considerably. The samples were annealed in situ
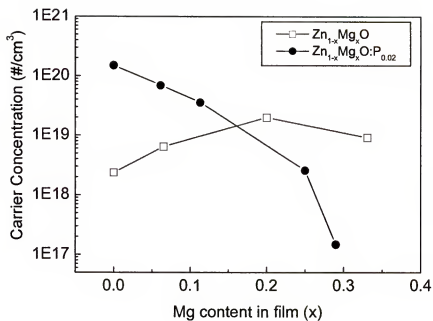
(a)
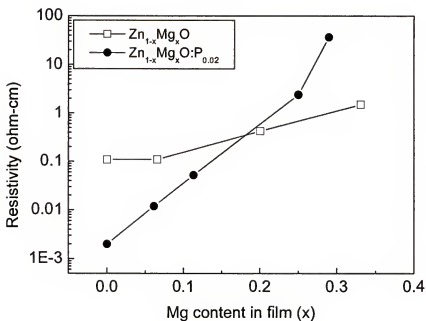
(b)

Figure 5-16 (a) Carrier concentration and (b) resistivity of 2% phosphorus doped and undoped $(Zn_{1-x}Mg_x)O$ as a function of Mg contents in thin films. Films are grown at 400°C with oxygen pressure of 20 mTorr.
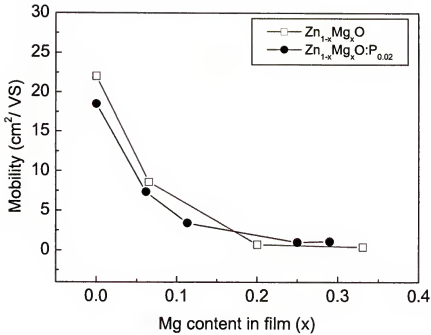
Figure 5-17 Mobility of 2% phosphorus doped and undoped $(Zn_{1-x}Mg_x)O$ as a function of Mg contents in thin films. Films are grown at 400°C with oxygen pressure of 20 mTorr.

at a temperature of 500˚C to 600˚C in a 100 Torr O_2 ambient for 60 min. For the M-I-S diode structures, the P-doped (Zn,Mg)O annealing step is followed by the deposition of a gate oxide. In this case, the gate oxide selected was $(Ce,Tb)MgAl_{11}O_{19}$, which is a wide bandgap insulator that can be deposited as an amorphous dielectric using pulsed-laser deposition. For the p-n junction devices, an undoped ZnO film was deposited on the P-doped (Zn,Mg)O film at a temperature of 400 ˚C in an oxygen ambient of 20 mTorr. Previous studies have shown that this condition yields n-type ZnO with a carrier density on the order of 10^{18}-10^{19}/cm^3. The top metallization contacts for both the p-n junction and M-I-S device structures were 0.2 mm diameter Al or In dots that were deposited by sputter deposition through a shadow mask.

In order to delineate the carrier type in the (Zn,Mg)O:P film, capacitance-voltage characteristics of the metal-insulator-semiconductor diode structures were measured, in which the (Zn,Mg)O:P film served as the semiconductor. Capacitance-voltage behavior for Schottky barrier or metal-insulator-semiconductor diodes provide an indirect means of determining the majority carrier type in a semiconductor material [104,105]. First, the symmetry of the capacitance-voltage behavior in MIS diodes is directly dependent on the carrier type underneath the gate. The total capacitance of the MIS diodes consists of two capacitances in series, one due to the insulator, as second due to the width of the depletion region underneath the gate dielectric. Depending on the majority carrier type, the M-I-S capacitance is maximized when the capacitor is biased such that the majority carriers accumulate at the semiconductor/insulator interface. For n-type material, a positive voltage relative to the semiconductor will attract majority carrier electrons to the interface, reduce the depletion width to near zero, and maximize capacitance. For p-type, a negative voltage is needed to accumulate majority carrier holes. In order to carefully delineate the carrier type behavior, MIS structures were fabricated with both n-type ZnO and phosphorus-doped (Zn,Mg)O thin films. Figure 5-18 shows the capacitance-voltage characteristics of a structure using undoped n-type ZnO as the semiconductor. In this case, a heavily doped n-type indium-tim-oxide layer served as the bottom electrode. The polarity of the capacitance-voltage characteristic for the device employing nominally undoped ZnO is clearly n-type, with capacitance decreasing with an applied negative voltage. For a MIS diode, the net ionized dopant density, N_A-N_D, can be estimated from the capacitance-voltage behavior, where N_A is the ionized acceptor density and N_D is the

donor density. In particular, for a uniformly doped semiconductor, the high frequency

capacitance/area in the depletion region is given by

$$N_A - N_D = \frac{2}{q\varepsilon_s}\left[\frac{d}{dV}\left(\frac{1}{C^2}\right)\right]^{-1}$$

where q is the electron charge and ε_s is the permittivity of the semiconductor. Figure 5-19

b) shows a plot of $1/C^2$ as a function of V for the diode employing n-type ZnO. From the

slope, the ionized donor density is estimated to be $1.8 \times 10^{19}/cm^3$, which is in agreement

with Hall measurements for similar polycrystalline ZnO films.

Similar device structures were then fabricated that employed phosphorus-doped

(Zn,Mg)O as the semiconductor material. Figure 5-19 shows the capacitance-voltage

behavior for these devices. The symmetry of the C-V curve indicates that the

(Zn,Mg)O:P film is p-type. Figure 5-25 b) shows a plot of $1/C^2$ for this device. From the

slope, the net acceptor concentration is calculated to be on the order of $2 \times 10^{18}/cm^3$. If

one assumes that all of the phosphorus dopant atoms are substitutional on an oxygen site,

one can estimate the activation energy based on a simple hydrogenic model. With this,

the activation energy is estimated to be 180-200 meV. In addition, given that the

resistivity of similar thin film material is on the order of 100-1000 Ω-cm, one can

estimate the magnitude of the hole mobility to be on the order of 0.01 to 0.001 cm^2/V-s.

This should not be taken as an intrinsic value of hole mobility for P-doped (Zn,Mg)O,

given that the films are polycrystalline with little optimization with respect to transport

properties. Nevertheless, this does explain why Hall measurements of carrier type is

difficult in many samples.
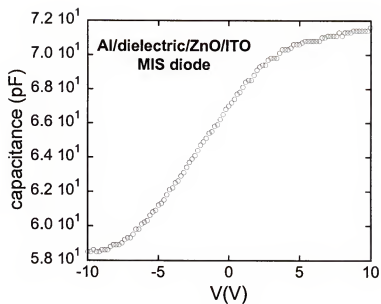
(a)
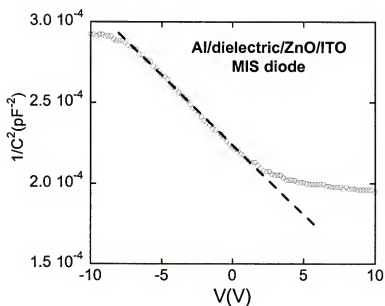
(b)

Fig. 5-18 Capacitance-voltage characteristics of n-type ZnO MIS diode. Plots of (a) C and (b) C^{-2} are included.
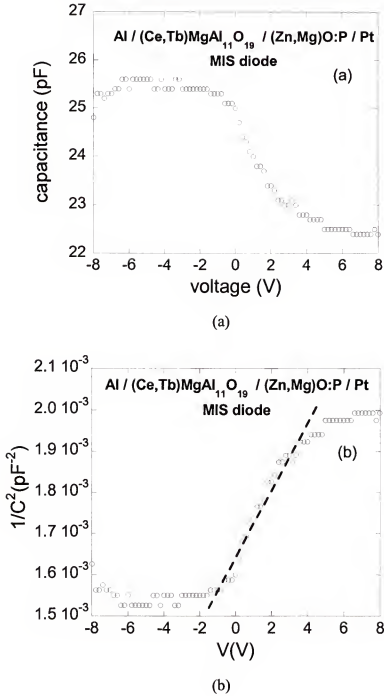
(a)

(b)

Fig. 5-19 Capacitance-voltage characteristics of P-doped (Zn,Mg)O MIS diode. Plots of (a) C and (b) C^{-2} are included.

For a pn junction, the total current I is the diffusion current minus the absolute value of the generation current, I_o

$$I = I_o(e^{qV/nkT} - 1)$$

where q is the elementary charge, k is the Boltzman constant, T is the absolute temperature, and n is the ideality factor. The ideality factor is 1 when the forward current in a p-n junction is dominated by recombination of excess minority carriers injected into the neutral regions of the junctions. The ideality factor is 2 when the recombination of carriers takes pace in the transition region.

In order to further delineate the carrier dynamics in P-doped (Zn,Mg)O thin films, n-ZnO/P-doped (Zn,Mg)O structures were fabricated to investigate whether pn junction characteristics could be observed. Figure 5-20 shows a schematic diagram of diode and equivalent circuit for n-ZnO/P-doped (Zn,Mg)O structures. The I-V measurements were performed at room temperature. Figure 5-21 shows the I-V curves for a $Pt/(Zn_{0.9}Mg_{0.1})O:P_{0.02}/n-ZnO/In$ junction. The I-V curve is clearly asymmetric, with a forward bias turn-on voltage on the order of 1 V. The reverse bias breakdown voltage is on the order of 4.5 V for this particular device. Similar characteristics were also observed for other devices fabricated with Al as the top contact. The I-V curves for reverse bias and strong forward bias are nearly linear functions, suggesting the presence of a series resistance and reverse bias leakage conductance that should be taken into account when modeling the junction transport measurements. Extracting estimates for these parasitic elements from the high forward and reverse biased conditions, a junction I-V curve is extracted and shown in Figure 5-27 b). A reasonable fit to a p-n junction diode equation is then achieved and shown as the solid line. However, the ideality factor extracted from
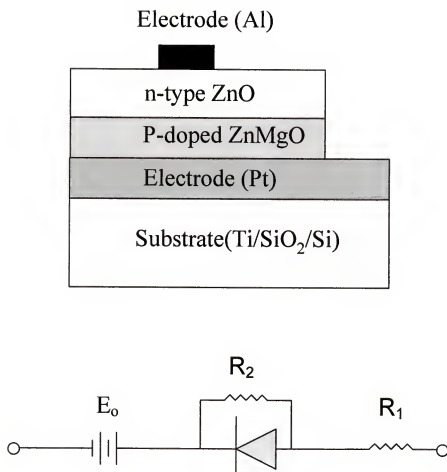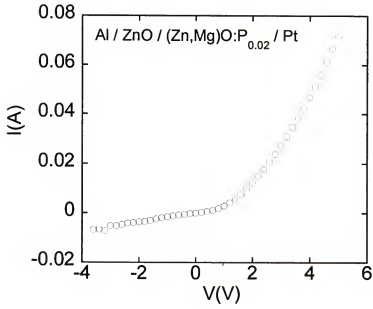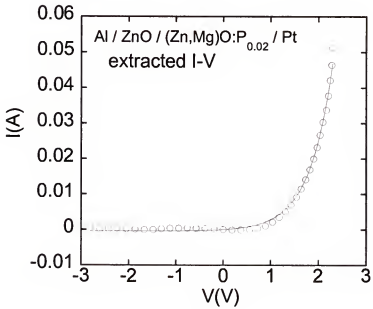
Figure 5-20 Schematic diagram of p-n junction diode and equivalent circuit for n-ZnO/P-doped (Zn,Mg)O structures.

Fig. 5-21 I-V curves for n-ZnO/P-doped (Zn,Mg)O junction. Both the raw I-V (a) and extracted I-V (b) are given. The latter assumes a parasitic leakage conductance and series resistance.

the junction equation is unphysically high, estimated to be between 10-20 for multiple devices that were measured. High ideality factors have been observed in other non-ideal wide bandgap pn junctions [106], and have been attributed to space-charge limited conduction [107], deep-level-assisted tunneling [108-110], or parasitic rectifying junctions within the device [106]. Nevertheless, the I-V characteristics are similar to those observed for other oxide p-n heterojunctions reported elsewhere [111-115], and strongly suggests that the low carrier density, low mobility (Zn,Mg)O:P films are p-type. Attempts to observe band edge emission from the junction bias in the forward direction were unsuccessful. However, given that the carrier mobility in the (Zn,Mg)O:P layer was low, efficient light-emitting diode operation was not expected.

Taking both the I-V and C-V characteristics of simple devices employing (Zn,Mg)O:P, we conclude that these films are low mobility p-type semiconductors.

5.3.3 Optical Properties of Phosphorus Doped ZnO

The optical properties of the phosphorus-doped ZnO films were examined both as-doped and after annealing treatments. The optical response was correlated to the transport properties. The photoluminescence properties of the films were measured at room temperature using a He-Cd laser (325 nm) and taken over a wavelength range of 350 to 800 nm. The power density was 1 W/cm^2. A 0.3 m scanning grating monochromator with a Peltier-cooled GaAs photomultiplier was utilized. Figure 5-22 shows the photoluminescence spectra taken for the as-deposited ZnO films with various phosphorus doping levels. The undoped epitaxial ZnO film shows a robust peak centered at 3.27eV, indicative of the near band edge emission. Note also the existence of the
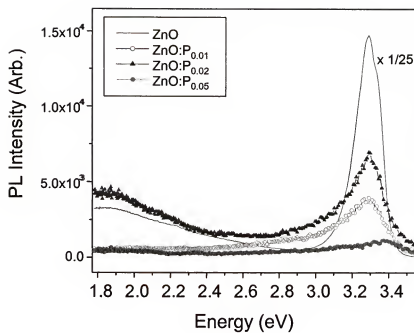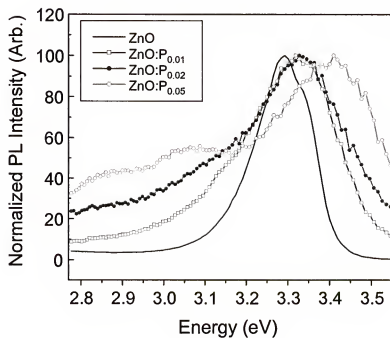
Fig. 5-22 Photoluminescence spectra for as-deposited ZnO epitaxial films with various phosphorus contents.

broadband orange-red emission. The addition of phosphorus to the ZnO films significantly reduces the near band-edge PL intensity, but does not quench it entirely. A similar reduction in the UV photoluminescence has been observed for doping with other acceptors, including Ag and Cu [116]. The reduction is consistent with the introduction of defect states leading to non-radiative decay of excited carrier. Note that the decrease in luminescence for the as-deposited films as the phosphorus content increase holds true for both the near band-edge UV and broadband visible emission that peaks at ~1.9 eV. The latter broadband emission is assumed due to radiative recombination involving point defects as will be discussed later interestingly, the peak in the near band-edge emission shifts to higher energy with phosphorus doping. For the 5 at.% P doping, the PL peak shifts to an energy of 3.41 eV. This shift in PL may reflect a Moss-Burstein type effect on the optical gap, in which a high carrier density of electron in the conduction band increases the optical gap [117]. This is seen in heavily doped degenerate oxide semiconductors in which the Fermi level moves above the conduction band edge, yielding occupied states well above the intrinsic conduction band edge. In the present case, doping with phosphorus drives the electron (n-type) carrier density to above 10^{20} cm^{-3}.

The photoluminescence behavior of the doped and undoped films was then examined as a function of annealing. The annealing treatments were performed in 100 Torr of oxygen for 1hour. Figure 5-23 shows the results for the undoped films. Previous annealing studies of ZnO have shown a strong dependence of PL on the annealing ambient, with a decrease in near-edge emission and an increase in visible defect-mediated luminescence as ZnO is annealed in an oxidizing environment [118-120]. It has also been shown that annealing in the hydrogen ambient increase the band edge emission while
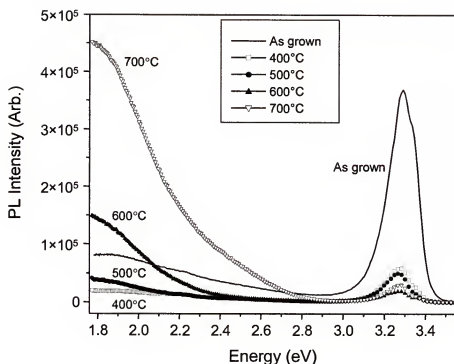
Fig. 5-23 Photoluminescence spectra for undoped ZnO film subjected to various annealing temperature.

subsequently decreasing the visible emission. Annealing in a reduced atmosphere also increase the electron density. It has been suggested that electron transfer to defects in high electron density materials passivates the deep states in the gap. In the present study, the undoped ZnO film shows a significant decrease in the near-edge UV emission with annealing, subsequent increase in the visible 1.9 eV luminescence for annealing temperature of 600°C or higher. Note that the broadband emission is not the green photoluminescence that has been attributed to the Zn interstitials and/or oxygen vacancies [121,122]. Annealing at a relatively high O_2 pressure should, in fact, decrease the density of defects related to oxygen deficiency.

For the P-doped ZnO films, annealing in 100 Torr of O_2 significantly reduces the near band-edge emission and enhances the visible orange-red broadband emission. Correlating the near band-edge emission with electron carrier density must take into account additional P-related defects for non-radiative recombination. The photoluminescence spectra of 2 at.% phosphorus-doped ZnO films subjected to annealing at various temperatures are shown in Figure 5-24. First, note that annealing at 400°C in 100 mTorr O_2 significantly suppresses the near band-edge emission without significantly
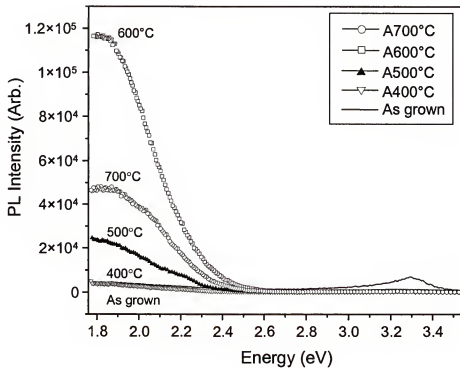

Fig. 5-24 Photoluminescence spectra for 2 at.% P-doped ZnO film annealed various temperature.

impacting the carrier density as seen in the figure. Though diminished, the peak location of the near edge emission shifts to lower energies. With annealing at higher temperature, the 1.9 eV broadband emission increase in intensity. For ZnO annealed in H_2, Previous work has been shown a direct correlation between carrier density and green luminescence [123]. For both the P-doped and undoped annealed ZnO films, there is an inverse correlation between the intensity of the 1.9 eV broadband emission and the carrier density. The orange-red luminescence increase as the conductivity is decrease due to high temperature anneals in 100 Torr O_2. This behavior is consistent with radiative recombination involving a deep acceptor level. With high electron density, the Fermi energy will be near the conduction band. As a result, deep states within the gap will be filled. Under these conditions, the probability of a radiative transition into a deep acceptor state will be low. As the electron carrier density reduced via annealing, the Fermi energy decrease and the density of empty states within the gap will increase. Thus, if the 1.9 eV luminescence is associated with radiative recombination involving deep acceptors, the intensity of the luminescence would increase with decreasing electron density, as is observed. This depopulation of gap states also explain the dependence of the near band-edge emission on electron carrier density, as a downward shift in the Fermi energy would enhance completing 1.9 eV radiative and non-radiative recombination of electrons in the conduction band due to an increase in unoccupied trap states. This model is consistent with result from other steady state and time-resolved luminescence studies for ZnO [119,124]. Note that similar effects also are observed for the photoluminescence spectra of Li-doped ZnO films [125,126].

In addition to photoluminescence, the photoconductivity response of doped and undoped ZnO films was examined. The steady-state resistivity was measured for films exposed to a Hg lamp emitting at 254nm at a power density of 3mW/cm^2. Previous results have demonstrated a significant photoconductivity response for ZnO exposed to UV radiation [127-130]. Figure 5-25, 5-26, and 5-27 shows that resistivity of the films both with and without UV illumination. The photoconductivity response of the as-deposited films is negligible due to the high dark current conductivity in both doped and undoped films. The annealed films show substantial photoconductive response, particularly for materials annealed at 600°C or higher. Most notably, the annealed films with phosphorous doping show the highest conductivity change, due in part to the high
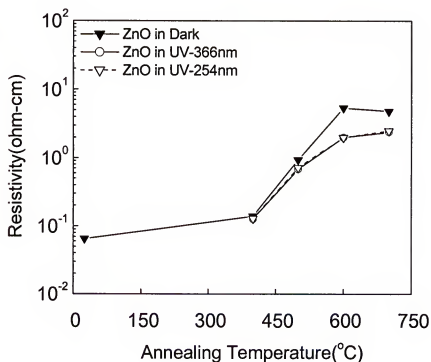

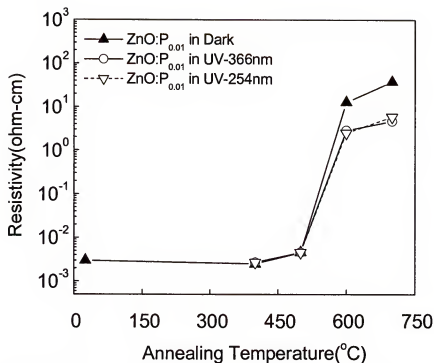Fig. 5-25 Photoconductivity response for undoped ZnO.

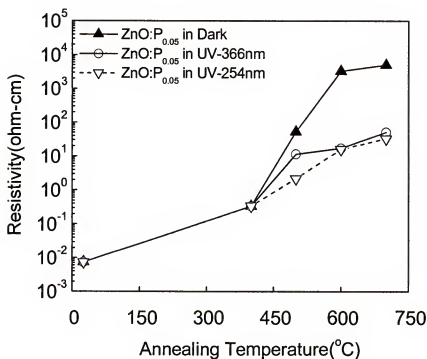Fig. 5-26 Photoconductivity response for 1 at.% P-doped ZnO.

Fig. 5-27 Photoconductivity response for 5 at.% P-doped ZnO.

resistivity in the dark state. For films annealed at 600°C, the ratio of resistivity with and without UV illumination varied from $\rho_{uv}/\rho_{dark} = 2.5$ for undoped to $\rho_{uv}/\rho_{dark} = 300$ for 5 at.% P-doped films. Interestingly, for the films considered in the figure, the dark resistivity n the undoped (2 Ω-cm) and 1 at.% P-doped (2.3 Ω-cm) films are comparable. Yet, the resistivity ratios with and without illumination differ by a factor of 2. Clearly the UV photoconductivity response in ZnO is enhanced in the P-doped annealed films.

5.3.4 Magnetic Properties of phosphorus doped ZnO after Mn implantation

The effects of initial carrier concentration in thin films of ZnO deposited on sapphire on the resulting transport and magnetic properties after high dose Mn implantation and annealing were examined.

The phosphorus-doped ZnO epitaxial films in this study were grown by pulsed-laser deposition (PLD) on single crystal (0001) Al_2O_3 substrate, using a ZnO: $P_{0.02}$ target and a KrF excimer laser ablation source. The laser repetition rate and laser pulse energy density were 1 Hz and 3 J-cm^{-2}, respectively. The films were grown at 400 °C in an oxygen pressure of 20 mTorr. The samples were annealed in the PLD chamber at temperatures ranging from 425 to 600 °C in O_2 ambient (100 mTorr) for 60 min. The resulting film thickness ranged from 350 nm to 500 nm. Four-point van der Pauw Hall measurements were performed to obtain the carrier concentration and mobility in the films. The carrier concentrations ranged from 7.5×10^{15} to 1.5×10^{20} cm^{-3}, with corresponding mobilities in the range 16-6 cm^2/Vs, as shown in Figure 5-28.

The films were implanted with 250 keV Mn$^+$ ions to a dose of 3×10^{16} cm^{-2} with the samples held at ~300 °C to avoid amphorization and subsequently annealed at 600°C for
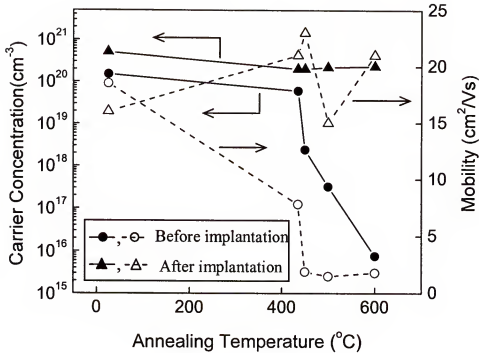
Fig. 5-28.Carrier concentration and electron mobility in n-type, P-doped ZnO films after annealing at different temperatures and after the same films were then implanted with Mn and annealed at a fixed temperature of 600 °C.

1 min in air in a Heatpulse 610T system. The transport properties were again obtained from Hall measurements and are also shown in Figure 5-28.The carrier concentration was in the range 2-5 $\times 10^{20}$ in each case with electron mobilities of 15-23 cm^2/Vs.The high electron concentration could arise from residual implant damage or formation of Mn-related donor complexes. It is clear that the transport properties are dominated by these effects since in each case the carrier concentration is significantly larger than in the samples prior to implantation.

The magnetic properties were obtained using a commercially available RF-Superconducting Quantum Interface Device (SQUID) (Quantum Design MPMS). None of the films showed any evidence for second phase formation from x-ray diffraction
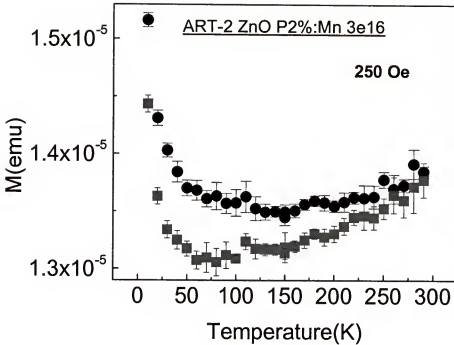
Fig. 5-29 Temperature-dependence of field-cooled (FC, circles) and zero field-cooled (ZFC, squares) magnetization in Mn-implanted ZnO subsequently annealed at 600°C.

measurements. In each case, the Mn-implanted samples showed differences in field –

cooled (FC) and zero-field cooled (ZFC) magnetization out to at least room temperature.

An example is shown in Figure 5-29 for the sample that was not annealed prior to

implantation. The difference between the two plots advantageously eliminates para- and

diamagnetic contributions and indicates the presence of hysteresis if the difference is

nonzero. This is particularly advantageous for thin-film samples where the amount of

ferromagnetic material in unoptimized samples may be small. Although ferromagnetism

is the usual explanation for hysteresis, spin glass effects, cooperative interactions between

superparamagnetic clusters, or superparamagnetism below a blocking temperature can

also be the cause. The field-cooled magnetization shows a positive curvature with a pronounced upturn at low temperatures. These rather unconventional shapes in the temperature-dependent magnetization were first seen in (Ga,Mn)As and seem to be the rule rather than the exception in most DMS materials [131]. Possible explanations for this behavior can be found in theoretical treatments that consider the effect of randomness and disorder on percolating ferromagnetic clusters [132-134].

Figure 5-30 shows the hysteresis in 300K magnetization versus field plots for three different samples after Mn implantation and annealing at 600°C.There is a remarkable change in both the saturation magnetization and coercivity for these samples implanted under identical conditions, even though the final electrical properties are almost the same. This is a strong indication that carrier concentration alone is not the only parameter that influences the magnetic characteristics of the ZnO:Mn. This is consistent with the work of Theodoropoulou et al [135],who found that ferromagnetism in ZnO thin films deposited by reactive magnetron sputtering was strongly dependent on parameters such as growth temperature ,O_2 partial pressure and type of substrate(only films deposited on Al_2O_3 substrates were ferromagnetic).Non-optimized growth conditions produced weakly paramagnetic behavior [135].

Figure 5-31 shows the dependence of room temperature saturation magnetization, M_S, and coercivity, H_C, on the initial post-growth annealing temperature of the ZnO films. The highest M_S values were obtained for the sample annealed initially at 600°C, which is likely to have the best crystalline quality and which had the lowest electron concentration. This may lead to a more even distribution of substitutional Mn^{2+} minimizing antiferromagnetic coupling [135]. In the ab-initio calculations hole doping stabilizes the
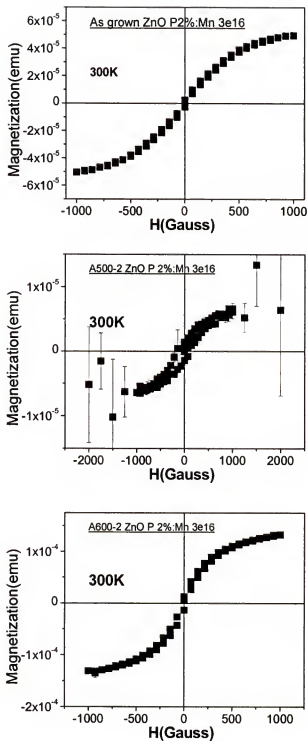
Fig. 5-30 Magnetization versus field at 300K for different films of ZnO implanted with Mn and subsequently annealed at 600°C. The sample at top was not annealed after growth, the one at center was annealed at 500°C and the one at bottom was annealed at 600C after growth.
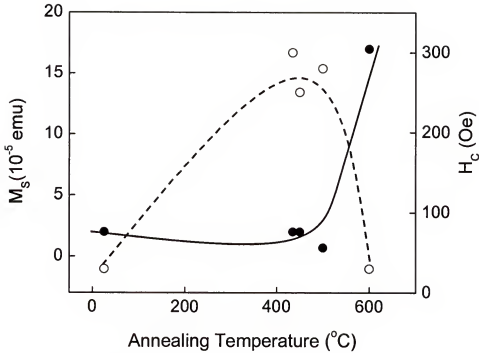
Fig. 5-31 Saturation magnetization (closed circles) and coercivity (open circles) of ZnO films annealed at various temperatures after growth and then implanted with Mn and subsequently annealed at 600°C.

ferromagnetic state in Mn-doped ZnO and the spin glass state becomes more energetic favorable as the n-type doping increases.

In conclusion, high dose Mn implantation into ZnO thin films grown on sapphire substrates produces ferromagnetism for all n-type doping levels investigated. The saturation magnetization is a strong function of the initial electrical properties of the films prior to implantation and explains some of the variation in magnetic properties reported in the literature for films grown by different methods on different substrates.

GROWTH AND CHARATERIZATION OF ZnO THIN FILM GROWN BY MOLECULAR BEAM EPITAXY

6.1 Introduction

Selection of the oxygen source and oxidant flux during growth plays an important role in determining the properties of ZnO, including crystallinity, electrical, and optical properties. Epitaxial ZnO thin films have been grown by numerous methods, including chemical vapor deposition (CVD), RF sputtering, pulsed laser deposition (PLD), and molecular beam epitaxy (MBE) [136-139]. For MBE growth of ZnO, the more common source of oxygen used in film growth is atomic oxygen, employing a plasma discharge source. However, for the growth of many oxides, ozone has proven useful as well. In atomic layer deposition, aluminum oxide thin films on patterned poly-Si (100) substrates were grown using ozone as an oxygen source yielding high quality film [140]. Ozone has been used as an oxygen source for the growth of $YBa_2Cu_3O_{7-x}$ thin films using molecular beam epitaxy.

The luminescence of ZnO consists of a near-band edge emission and a deep-level emission. A strong near-band edge emission is important for UV optoelectronic devices such as LEDs and LDs. Therefore, many efforts have been focused on the mechanism of near band emission, consisting of free exciton, donor- or acceptor-bound exciton, and its phonon replicas. However, the mechanism of deep-level emission has not been clearly explained. To explain the green emission, various models have been suggested.

Vanheusden reported that the green emission is the recombination of V_O electrons with photoexcited holes in the valence band by combining electron paramagnetic resonance, optical absorption, and photoluminescence spectroscopy [122]. S. A. Studenikin suggested that a green PL in ZnO is due to an electron-hole recombination involving a donor-acceptor complex, which most likely consists of an oxygen vacancy and a zinc vacancy [124]. H.-J. Egelhaaf reported that the green luminescence of polycrystalline ZnO, investigated by diffuse reflection, steady state and time-resolved photoluminescence, and photoconductivity, is assigned to a donor (related to oxygen vacancy)-acceptor (Zn vacancy)-type transition [141]. D.C. Reynolds, D.C. Look, and B. Jogai suggested that the green luminescence emission is a phonon-assisted transition between two shallow donors and a deep acceptor [142]. P.S. Xu. suggested that the green emission comes from donor levels Zn_i to acceptor levels V_{Zn} [143]. B. Lin suggested that green luminescence corresponds to the electron transition from the bottom of the conduction band to the antisite defect O_{Zn} level [144]. The green emission is observed from oxygen deficient ZnO samples prepared by reduction annealing in forming gas(N_2:H_2=95:5). Orange emission from oxygen rich film is obtained by oxidative annealing in oxygen [129]. X.L.Xu et. al reported that the violet, green, and yellow emission are attributed to the radiative recombination of delocalized electrons close to the conduction band with deeply trapped holes in V_{Zn}^-, V_o^+, and O_i^- centers, respectively[145].

In this chapter, the origins of the deep-level emission of ZnO grown by molecular beam epitaxy, using RF plasma for atomic oxygen, are investigated. In particular, the deep-level emission is shifted from green to yellow with reducing Zn pressure during the growth. Photoluminescence and Hall measurement are employed to study a correlation

between deep-level/near band-edge emission and carrier density. With these results, we suggest that the green in deep-level emission is related to donors-deep acceptor (Zn vacancy, V_{Zn}^-) and the yellow to donors-deep acceptor (oxygen vacancy, O_i^-). The growth of ZnO thin film via molecular beam epitaxy is also investigated using ozone as the oxygen source. The growth properties of ZnO thin films are studied as a function of Zn flux, ozone flux, and growth temperature.

6.2 Experimental

The growth experiments were performed using a conventional MBE system as shown in Figure 6-1. The background base pressure of the growth chamber was $\sim 5 \times 10^{-8}$ mbar. Effects of oxygen sources on the growth of ZnO were investigated by using two different oxygen sources. One is an ozone/oxygen mixture and the other atomic oxygen. The nitrogen-free plasma discharge ozone generator yielded an O_3/O_2 ratio on the order of 1%–3%. No effort was made to separate the molecular oxygen from the ozone. An RF plasma atomic source was used to generate the atomic oxygen source. The flux of Zn was provided by Knudsen effusion cells using high purity Zn metal (99.9999%) as the source. Zn and oxygen source pressures were determined via a nude ionization gauge that was placed at the substrate position prior to growth. The beam pressures of O_3/O_2 mixture and atomic oxygen was varied between 5×10^{-6} and 5×10^{-4} mbar, and controlled by a leak valve between the ozone generator and the chamber. The Zn pressure was varied between 5×10^{-7} and 5×10^{-6} mbar. C-plane Al_2O_3 wafers were used as substrates. Prior to film growth, the (0001) Al_2O_3 substrates were cleaned with trichloroethylene, acetone, and methanol. Typical growth temperature for ZnO on c-plane Al_2O_3 ranges from
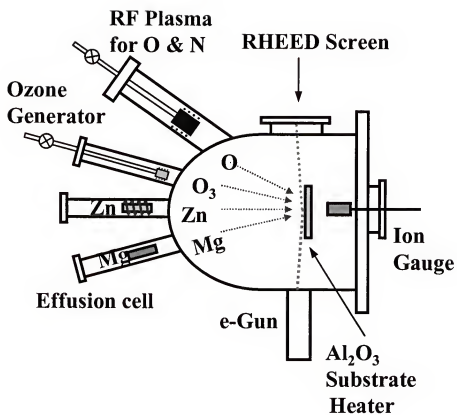
Fig. 6-1 Schematic diagram of Molecular Beam Epitaxy.

Tg = 200 to 500 °C using Zn vapor and one of the oxygen sources. After growth, the samples were cooled to room temperature while maintaining the growth pressure. Surface profilometry across a film step was used to determine film thickness.

<div align="center">6.3 Result & Discussion</div>

6.3.1 Growth and Characterization of ZnO Grown with Atomic Oxygen.

6.3.1.1 Growth and Electrical Properties.

The growth rate of epitaxial ZnO films was studied as a function of RF power. Figure 6-2 shows the growth rate of ZnO thin films grown on c-plane Al_2O_3 as a function of RF power at a growth temperature of 400°C for an oxygen pressure of 5×10^{-5} mbar, and a Zn pressure of 1×10^{-6} mbar. The growth rate increases with RF power up to 400W and
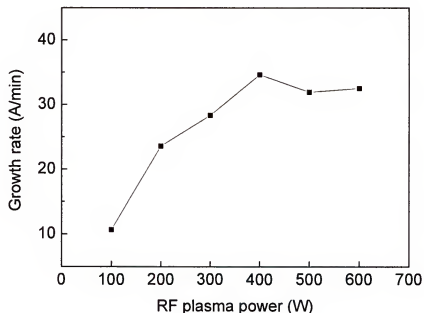

Figure 6-2 Growth rate of epitaxial ZnO films grown on c-plane Al_2O_3 as a function of RF power at 400°C growth temperature for an oxygen pressure of 5×10^{-5} mbar and a Zn pressure of 1×10^{-6} mbar.

then saturates at a value of approximately 32 Å/mim, even though a higher RF plasma power generates more reactive atomic oxygen at the same oxygen pressure that can lead to a higher growth rate. The saturation growth rate indicates that, above an RF power of 400W, the growth rate is controlled not by oxygen but by Zn pressure. Therefore, the growth rate becomes saturated at the condition of constant Zn pressure above an RF power of 400W.

Figure 6-3 shows scanning electron microscopy images of ZnO for different RF powers at 400°C with an oxygen pressure of 5×10^{-5} mbar and a Zn pressure of 1×10^{-6} mbar. Above an RF power of 400W, the surface of ZnO is smoother but has multiple pore defects. Carrier density and resistivity in Figure 6-4 do not vary much with an RF power above 300W. Based on the SEM images, carrier density, and resistivity, an RF power of 300W is selected for the growth ZnO film.

Growth and electrical properties of ZnO was investigated as a function of Zn pressures at 500°C with an oxygen pressure of 5×10^{-5} mbar. Figure 6-5 shows that the growth rate increases with an increase of Zn pressure. Growth rate is dominated not by oxygen pressure, but by Zn pressure in this growth condition. Figure 6-6 shows a resistivity and carrier concentration of ZnO films grown as a function of Zn pressures at 500°C with oxygen pressure of 5×10^{-5} mbar. The resistivity decreases and the carrier concentration increases as Zn pressure increases. In ZnO growth, there are a several intrinsic defects, such as Zn interstitial (Zn_i), oxygen vacancy (V_o), Zn vacancy (V_{Zn}), and oxygen interstitial (O_i). Naturally, vacancies (V_O) and Zn interstitials (Zn_i) are dominant defects in undoped ZnO. The creation of intrinsic n-type defects, such as oxygen

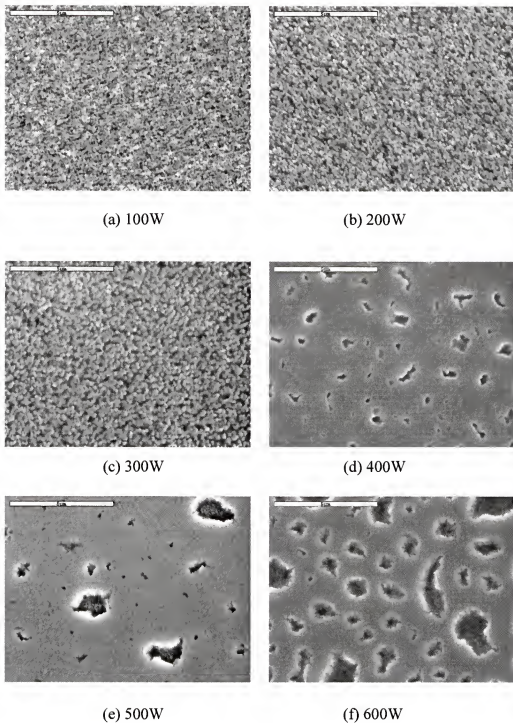(a) 100W

(b) 200W

(c) 300W

(d) 400W

(e) 500W

(f) 600W

Figure 6-3 Scanning electron microscopy images of ZnO for different RF powers at 400°C with an oxygen pressure of 5×10^{-5} mbar and a Zn pressure of 1×10^{-6} mbar, (a) 100W, (b) 200W, (c) 300W, (d) 400W, (e) 500W, and (f) 600W.

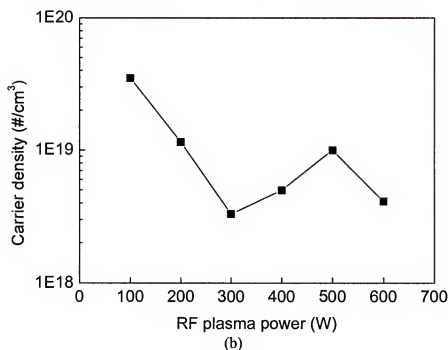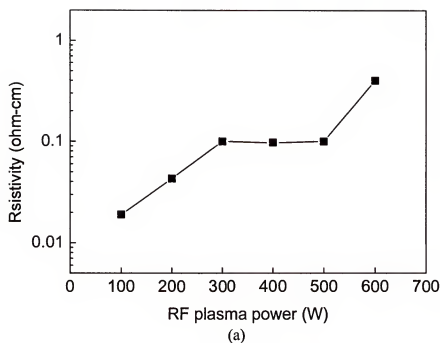Fig 6-4 Carrier density (a) and resistivity (b) of ZnO at 400°C with an oxygen pressure of 5×10^{-5} mbar and a Zn pressure of 1×10^{-6} mbar with RF powers of 300W.

Figure 6-5 Growth rate of ZnO grown as a function of Zn pressures at 500°C with oxygen pressure of 5×10^{-5} mbar.

(a)

(b

Figure 6-6 (a) Resistivity and (b) carrier concentration of ZnO film grown as a function of Zn pressures at 500°C with oxygen pressure of 5×10^{-5} mbar.

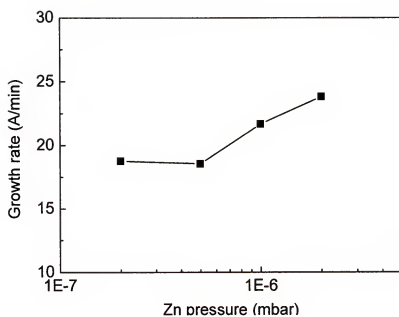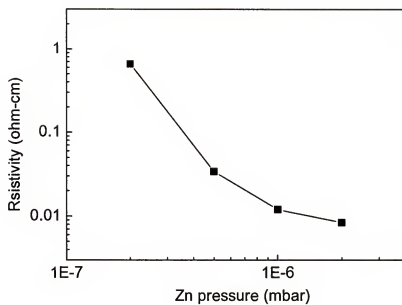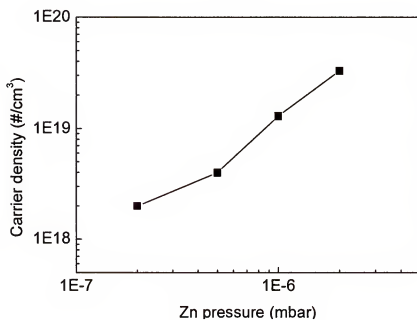vacancies (V_O) and Zn interstitials (Zn_i), is thermodynamically more favorable than that of intrinsic p-type defects such as Zn vacancies (V_{Zn}) and O interstitials (O_i) [146]. Electron-irradiation experiments show that Zn interstitials (Zn_i) are the best candidate for dominant shallow donors [147]. First-principle calculations using a full potential linear muffin-tin orbital (FP-LMTO) indicates that Zn interstitial (Zn_i) is the dominant donor in ZnO [148]. The Oxygen vacancy (V_o) has been identified in electron paramagnetic resonance (EPR) studies as a deep donor [149]. Therefore, the increase of Zn interstitials (Zn_i) in ZnO with Zn pressure mainly increases the resistivity and carrier density.

6.3.1.2. Optical Properties.

Optical properties of ZnO films were investigated by photoluminescence measurement using He-Cd laser as an excitation source (325nm). Figure 6-7 shows photoluminescence spectra, measured at room temperature and 10 K, for ZnO grown at 450°C with a Zn pressures of 3×10^{-6} mbar and oxygen pressure of 5×10^{-5} mbar. Photoluminescence spectra display a strong near band-edge (NBE) emission and a weak deep-level (DL) emission. The low-temperature PL spectra are dominated by a strong near band emission of 3.36 eV and 3.374 eV that are assigned to the donor-bound exciton (D^o,X) and free exciton (X_A), respectively, as shown in Figure 6-7 (a) and (b) [150,151]. This emission has a series of phonon replicas (D^o,X)-LO and (D^o,X)-2 LO at 3.288 eV and 3.214eV, respectively. The bound excitons are decomposed by thermal energy with an increase in temperature, and the emission from the free exciton, shifted to 3.30 eV, is dominated at a room temperature photoluminescence as shown in Figure 6-7 (a).
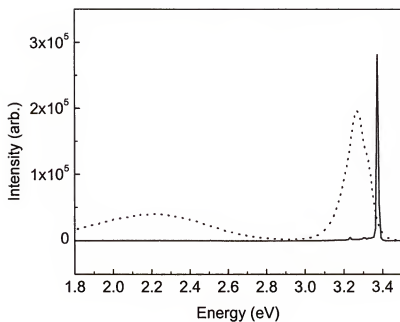
(a)
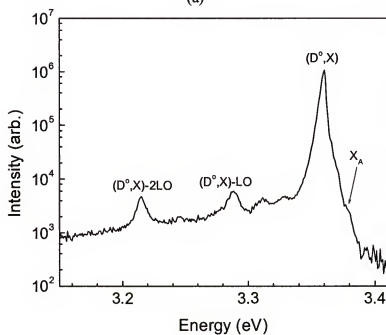
(b)

Figure 6-7 Photoluminescence spectra for ZnO grown at 450°C with a Zn pressures of 3×10^{-6} mbar and oxygen pressure of 5×10^{-5} mbar measured at (a) room temperature and (b)10 K .

Figure 6-8 shows the room-temperature photoluminescence spectra of ZnO grown at 500°C with an oxygen pressure of 5×10^{-5} mbar as a function of Zn pressure. The near band-edge emission decreases and the deep-level emission increases as Zn pressure decreases during the growth of ZnO. Figure 6-9 shows the ratio of a deep-level emission (DL) to a near band-edge emission (NBE) for ZnO grown at 500°C with an oxygen pressure of 5×10^{-5} mbar as a function of Zn pressure. The ratio decreases as the Zn pressure increases. The decrease of near band-edge emission (NBE) is followed by the increase of deep-level emission. In ZnO growth using molecular beam epitaxy with reactive atomic oxygen, the ratio of oxygen to zinc is larger than 10 because the maximum Zn pressure is 3×10^{-6} mbar and the oxygen pressure is kept at a value of 5×10^{-5} mbar. At the growth temperature, the sticking coefficient of Zn will be much lower than 1 because Zn is a high vapor pressure material. The increase in growth rate of ZnO with an increase of Zn pressure, as shown in Figure 6-5, suggests that the growth condition is oxygen-rich. During the growth of ZnO with an oxygen-rich condition, the possible changes of defects with the Zn pressure could be described as the following:

$$[Zn_i] \propto P_{Zn} \quad (\, Zn(g) = Zn_i \,)$$

$$[V_O] \propto P_{Zn} \quad (\, Zn(g) = Zn_{Zn} + V_O \,)$$

$$[O_i] \propto P_{Zn}^{-1} \quad (\, Zn(g) + O_i = Zn_{Zn} + O_O \,)$$

$$[V_{Zn}] \propto P_{Zn}^{-1} \quad (\, Zn(g) + V_{Zn} = Zn_{Zn} \,)$$

An increase of the Zn pressure results in an increase of Zn interstitials (Zn_i) and oxygen vacancies (V_O) and a decrease of Zinc vacancies (V_{Zn}) and oxygen vacancies (O_i), also proven by the hall measurement data shown in Figure 6-6, even though the generation
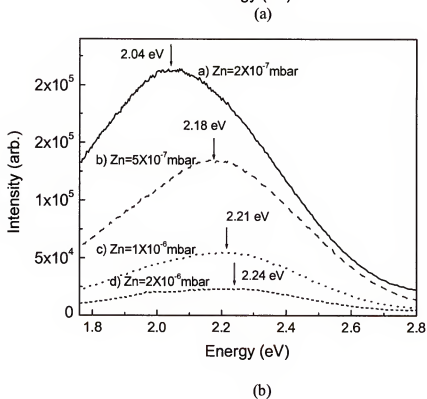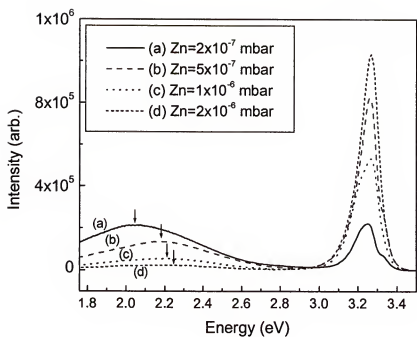
Figure 6-8 Room-temperature photoluminescence spectra of ZnO grown at 500°C with an oxygen pressure of 5×10^{-5} mbar as a function of Zn pressures.
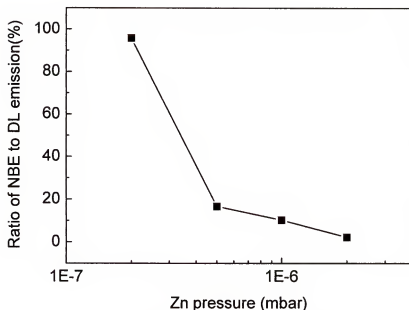
Figure 6-9 Ratio of a deep-level emission (DL) to a near band-edge emission (NBE) for ZnO grown at 500°C with an oxygen pressure of 5×10^{-5} mbar as a function of Zn pressures.

rate of defects may be different due to different enthalpy formation energies [146]. According to the theoretical calculation using the local density approximation, formation enthalpies of native Zn interstitial (Zn_i) and oxygen vacancy (V_O) are lower than that of Zn vacancy (V_{Zn}) and oxygen interstitial (O_i), for both Zn-rich and O-rich conditions [146]. If the deep level emission is related to a radiative transition from the conduction band to an oxygen vacancy (V_O^+) [145] or from an oxygen vacancy (Vo^+) to the valence band [123], the deep level emission should increase with an increase in oxygen vacancies (V_O^+). However, the results show that the deep level emission decreases with an increase of oxygen vacancy (V_O^+). If the deep level emission is related to a radiative transition from donors to acceptors [124, 141~143], the decrease of the acceptors can explain the decrease of the deep level emission with an increase of Zn pressure as shown in Figure 6-

8. Therefore, the near band edge emission that is related to the free exciton and the donor-bounded exciton increases with the increase of donors (Zn_i, V_O). The deep level emission that is related to a radiative transition from donors (Zn_i, V_O) to acceptors (V_{Zn}, O_i) is determined by the concentration of acceptors. The competition of radiative transitions between from donors to acceptors and from free exciton (and/or donor-bound exciton) to valence band determines the photoluminescence spectrum of ZnO.

In order to investigate a relationship between deep-level emission and the crystallinity of ZnO, four-circle x-ray diffraction is measured. Figure 6- 10 shows the rocking curve through the (002) plane of ZnO grown at 500°C with an oxygen pressure of 5×10^{-5} mbar as a function of Zn pressure. The variation of the full width half maxim (FWHM) of ZnO with Zn pressure is small. Figure 6-11 shows the ϕ-scan and pole figure through the (10$\bar{1}$1) plane of ZnO grown at 500°C with a Zn pressures of 2×10^{-6} mbar and oxygen pressure of 5×10^{-5} mbar, indicating an epitaxial thin film of ZnO on c-plane Al_2O_3. Therefore, in this growth condition of ZnO grown by MBE using atomic oxygen source, it seems that crystallinity is not much related to the deep-level emission.

As Zn pressure decreases during the growth of ZnO, deep-level emission peak position shifts from green (2.24 eV) to yellow (2.04 eV) with an increase of the intensity of deep-level emission as shown in Figure 6-9 (b). A typical green emission peak of ZnO has been observed at 2.4 eV [122, 124, 152]. Oxygen defect V_o^+ as a donor and Zn defect V_{Zn}^- as an acceptor are located at 190 meV and 2.5 eV below the conduction band edge, respectively [153]. The green emission is reported from electron-hole recombination of transitions from donors (related to Zn_i or V_o^+) to deep acceptors (V_{Zn}^+) [124, 141-143].

Previous work reported that yellow emission can be attributed to the radiative recombination of a delocalized electron close to the conduction band with a deeply trapped hole in the O_i^- center [154,155]. In the growth condition of ZnO by MBE with constant oxygen pressure, the concentration of Zn vacancies (V_{Zn}) and oxygen interstitials (O_i) increase with a decrease of Zn pressure. The different rates of radiative transition between from donors to Zn vacancy (V_{Zn}) and from donors to oxygen interstitial (O_i), due to the difference in the concentrations of Zn vacancy (V_{Zn}) and oxygen interstitial (O_i), generate the shift of deep level emission. From the yellow shifts of deep level emission, it appears that the concentration of oxygen interstitials (O_i) becomes larger than that of Zn vacancies (V_{Zn}) with a decrease of Zn pressure during the growth of ZnO.
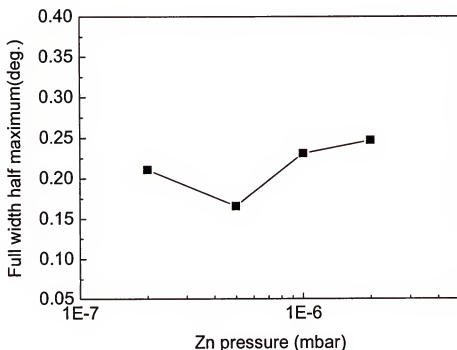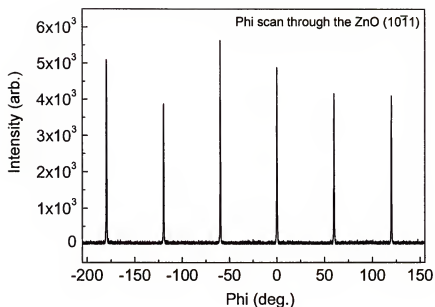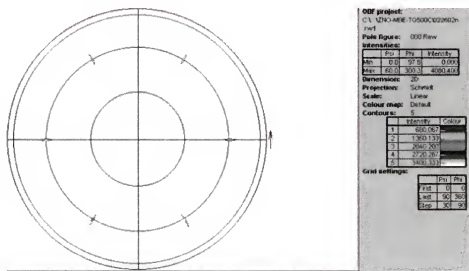

Figure 6- 10 Rocking curve through (002) plane of ZnO grown at 500°C with an oxygen pressure of 5×10^{-5} mbar as a function of Zn pressure.

(a)

(b)

Figure 6-11 (a) φ scan and (b) pole figure through (10$\bar{1}$1) plane of ZnO grown at 500°C with a Zn pressures of 2×10^{-6} mbar and oxygen pressure of 5×10^{-5} mbar.

Figure 6-12 shows the room-temperature photoluminescence spectrum of ZnO grown at 450°C with a Zn pressure of 3×10^{-6} mbar and oxygen pressure of 5×10^{-5} mbar and that of ZnO annealed at 600°C with oxygen pressure of 100 Torr. During the annealing treatment of ZnO with oxygen atmosphere, the possible changes of defects with the oxygen pressure could be described as the following:

$[Zn_i] \propto P_{O_2}^{-1/2}$ ($Zn_i + \frac{1}{2} O_2(g) = Zn_{Zn} + O_O$)

$[O_i] \propto P_{O_2}^{1/2}$ ($\frac{1}{2} O_2(g) = O_i$)

$[V_{Zn}] \propto P_{O_2}^{1/2}$ ($\frac{1}{2} O^2(g) = V_{Zn} + O_O$)

$[V_O] \propto P_{O_2}^{-1/2}$ ($V_O + \frac{1}{2} O_2(g) = O_O$)

The annealing treatment of ZnO in an oxygen atmosphere increases the concentration of Zn vacancies (V_{Zn}) and oxygen interstitials (O_i) according to the above relationship between the concentration of defects and oxygen pressure. Also, the reduction of the carrier concentration from 9×10^{18} to 3×10^{17} after annealing indicates that donors (related to Zn_i and Vo) decrease and acceptors (related to V_{Zn} or O_i) increase. The intensity of the near band-edge emission decreases without peak shift after annealing in an oxygen atmosphere. The ratio of the deep-level emission to the near band emission is changed from 0.20 to 0.26. However, the deep level emission peak shifts from 2.21 eV to 2.07 eV as shown in Figure 6-12 (b). The yellow shift of deep level emission suggests that the concentration of oxygen interstitials (O_i) become larger than that of Zn vacancies (V_{Zn}) after annealing in oxygen atmosphere.
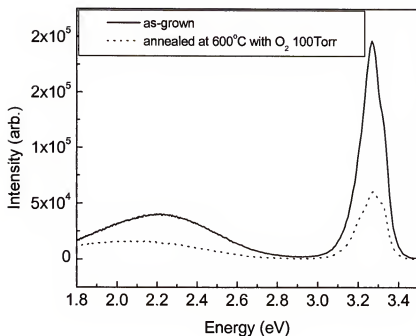
(a)
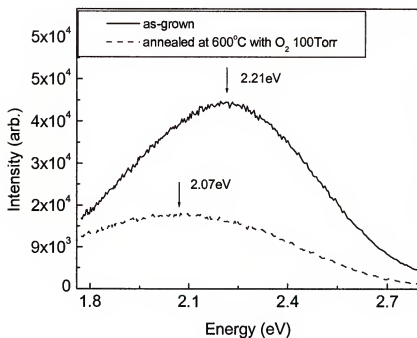
(b)

Figure 6-12 Room-temperature photoluminescence spectra for (a) ZnO grown at 450°C with a Zn pressures of 3×10^{-6} mbar and oxygen pressure of 5×10^{-5} mbar and (b) that of ZnO annealed at 600°C with oxygen pressure of 100 Torr.

6.3.2 Growth of ZnO Thin Film on c-plane Al_2O_3 by Molecular Beam Epitaxy Using Ozone as Oxygen Source

The growth rate of epitaxial ZnO films was studied as a function of O_3/O_2 flux and substrate temperature. Figure 6-13 shows the growth rate of ZnO thin films grown on c-plane Al_2O_3 as a function of growth temperature for a Zn pressure of 2×10^{-6} mbar and O_3/O_2 pressure of 5×10^{-4} mbar. The rate was approximately 500Å per hour for temperatures up to 350°C. Note that the O_3/O_2 flux rate was relatively high as will be discussed later. For growth temperature greater than 350°C, the growth rate was dramatically decreased. In fact, ZnO films did not nucleate on the Al2O3 crystalline surface for growth temperatures above 450°C. An increase in growth temperature causes a decrease of the sticking coefficient of Zn on the Al_2O_3 substrate which, subsequently, causes a decrease in the growth rate, even though the reactivity between Zn and oxygen source increase with growth temperature. Note that there was no nucleation and growth of ZnO film on the sapphire substrate when only O_2 was used as the oxygen source. The dissociation energy of oxygen molecules (O_2) of 5.2 eV is much higher than that for ozone. In fact, ozone decomposes exothermically, with a heat of decomposition around -163 KJ/mol (1.69 eV/molecule)[156]. At temperatures sufficiently high for reaction of O_2 with Zn metal, the vapor pressure of Zn is too high to yield a surface reaction on Al_2O_3.

The dependence of ZnO growth rate on Zn and oxygen flux was also investigated. Figure 6-14 shows the x-ray diffraction patterns for films deposited at 350°C under various Zn and O_3/O_2 flux rates. As shown in the figure, the growth of ZnO was not be observed for a Zn pressure less than 2×10^{-7} mbar at a growth temperature of 350°C. The highest (0002) XRD peak intensity for ZnO was observed with a Zn pressure of 2×10^{-6}
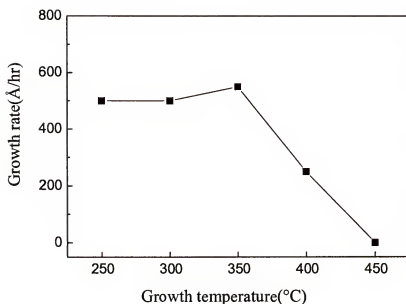
Fig. 6-13 Growth rate of ZnO grown on c-plane Al$_2$O$_3$ as a function of growth temperature with a Zn pressure of 2×10^{-6} mbar mbar and O$_3$/O$_2$ pressure of 5×10^{-4} mbar.

mbar and O$_3$/O$_2$ pressure of 5×10^{-4} mbar. The film formed under these conditions was c-axis oriented on the c-plane sapphire surface. In addition, the crystallinity of ZnO films grown at different temperatures was also examined. Figure 6-15 shows the XRD patterns of ZnO films deposited on the c-plane Al$_2$O$_3$ at different growth temperature with Zn pressure of 2×10^{-6} and O$_3$/O$_2$ pressure of 5×10^{-4} mbar. The intensity of the (0002) peak increases with growth temperature up to 350°C, and then decreases for higher temperature. The intensity of (0002) peak disappears at growth temperature of 450°C.

The crystallinity of the films is further investigated by four-circle x-ray diffraction. The rocking curve through the (0002) plane of ZnO film grown at Zn pressure of 2×10^{-7} mbar and O$_3$/O$_2$ pressure of 5×10^{-4} mbar at 350°C shown in Fig. 6-16 (a). The full width
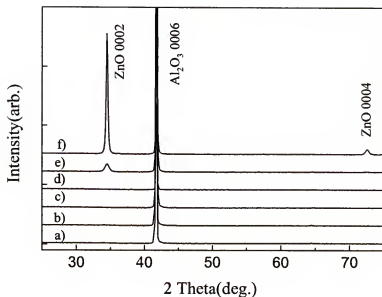
Fig. 6-14 XRD patterns of ZnO grown on sapphire (001) at 350°C growth temperature as a function of Zn and O_3/O_2 pressures a) Zn of 2×10^{-7} mbar and O_3/O_2 of 5×10^{-6} mbar, b) Zn of 2×10^{-7} mbar and O_3/O_2 of 5×10^{-5} mbar, c) Zn of 5×10^{-7} mbar and O_3/O_2 of 5×10^{-4} mbar, d) Zn of 2×10^{-6} mbar and O_3/O_2 of 5×10^{-6} mbar, e) Zn of 2×10^{-6} mbar and O_3/O_2 of 5×10^{-5} mbar, f) Zn of 5×10^{-6} mbar and O_3/O_2 of 5×10^{-4} mbar.
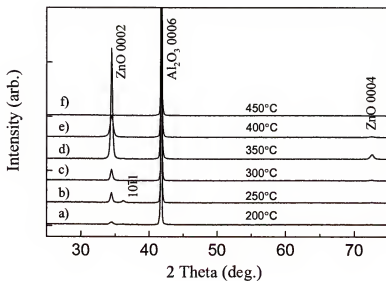
Fig. 6-15 XRD pattern of ZnO grown on sapphire (001) with a Zn pressure of 2×10^{-6} mbar and O_3/O_2 pressure of 5×10^{-4} mbar as a function of growth temperature a) 200°C, b) 250°C, c) 300°C, d) 350°C, e) 400°C, and f) 450°C.

half maximum (FWHM) was measured to be 0.95°.Only the c-axis ZnO peaks are evident

in the plot of θ-2θ scan along the surface normal for the ZnO film. High-resolution θ-2θ

scan through the (0002) plane indicate that the 2θ FWHM is 0.26°. A high resolution scan

through the (0002) peak yields a c-axis lattice parameter of 5.1948Å, which is slightly

smaller than the bulk value. φ scans through the ZnO (10$\bar{1}$1) plane in Figure 6-16 (b)

show in-plane alignment with Δφ = 1.6°. Pole figure shows sixfold symmetry of ZnO

(10$\bar{1}$1) plane, too. There is a 30° rotation between the in-plane ZnO and Al$_2$O$_3$ direction

due to the 18% of lattice mismatch between film and substrate.

The surface morphology of the ZnO film was measured using atomic force

microscopy (AFM) measurements. AFM measurement was performed in air via a

Nanoscope III. All samples were scanned over a 1 × 1 μm^2 area. In Figure 6-17, the AFM

images for ZnO films grown on sapphire at various temperatures are shown, A Zn

pressure of 2 × 10^{-6} mbar and O$_3$/O$_2$ pressure of 5 × 10^{-4} mbar were employed during

growth. As the temperature increase from 200°C, roughness increases, the surface

reflecting an increase in ZnO grain size for growth temperatures up to 350°C. At 450°C

growth temperature, the nucleation of ZnO decrease rapidly, with little or no ZnO Film

growth occurring. This is consistent with the XRD and growth rate behavior discussed

earlier.

In addition to growth kinetics and crystallinity, the optical properties of these

MBE-grown ZnO films using ozone were characterized using photoluminescence at room

temperature. Photoluminescence spectra for the ZnO film grown on Sapphire with a Zn
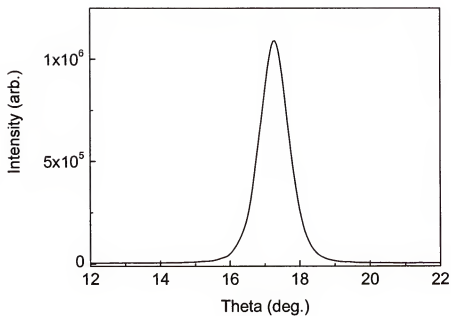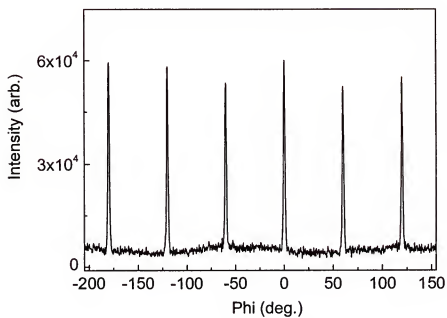
Fig. 6-16 (a) Rocking Curve through (0002) and (b) φ scans for (10$\bar{1}$1) plane of ZnO grown on c-plane Al$_2$O$_3$.

a) RMS=8.44nm
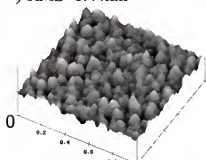
b) RMS=10.26nm

Tg= 200°C
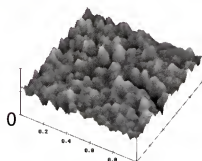
Tg= 250°C

c) RMS=17.25nm
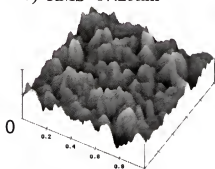
d) RMS=19.06nm

Tg= 300°C
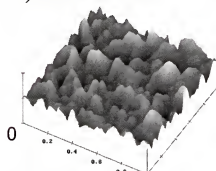
Tg= 350°C

e) RMS=6.45nm
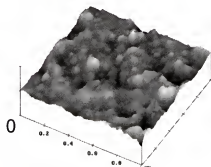
f) RMS=2.62nm

Tg= 400°C
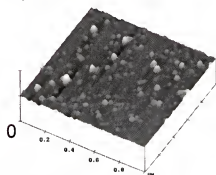
Tg= 450°C

Fig. 6-17 AFM images of ZnO grown on sapphire with a Zn pressure of 2×10^{-6} mbar and O_3/O_2 pressure of 5×10^{-4} mbar as a function of growth temperature a) 200°C, b) 250°C, c) 300°C, d) 350°C, e) 400°C, and f) 450°C.

pressure of 2×10^{-6} mbar and ozone pressure of 5×10^{-4} mbar at a growth temperature of 350°C was measured using a He-Cd laser (325nm). The power density was 1W/cm^2. A 0.3 m scanning grating monochromator with a Peltier-cooled GaAs photomultiplier was utilized. Figure 6-18 shows the spectrum indicating a near band-edge emission at 3.30 eV for the film. Note also the existence of the broadband orange-red emission at 1.9 eV and blue emission at 2.73 eV. The blue and orange-red emission is indicative of defects yielding states in the gap.

The transport properties of these films were characterized sing Hall measurements. Figure 6-19 shows carrier concentration and resistivity of ZnO grown on Sapphire with a
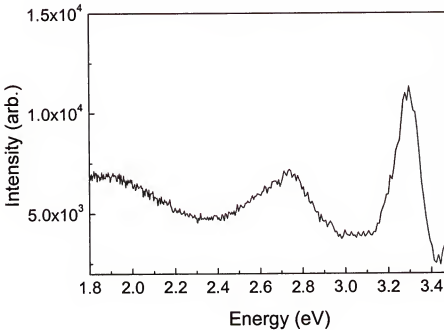
Fig. 6-18 Photoluminescence spectrum at room temperature of ZnO grown on Sapphire with a Zn pressure of 2×10^{-6} mbar and O$_3$/O$_2$ pressure of 5×10^{-4} mbar at 350°C growth temperature.

Zn pressure of 2×10^{-6} mbar and Ozone pressure of 5×10^{-4} mbar as a function of growth temperature. The current density was high in all samples, ranging from 2×10^{19} cm^{-3} to 2×10^{20} cm^{-3}. Carrier concentration increased and resistivity decreased with the growth temperature. ZnO grown on sapphire using ozone (O_3/O_2) is highly conductive and n-type.
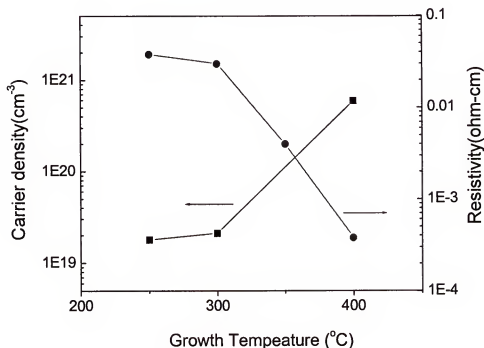
Fig. 6-19 Carrier concentration and resistivity of ZnO grown on Sapphire as a function of growth temperature with a Zn pressure of 2×10^{-6} mbar and O_3/O_2 pressure of 5×10^{-4} mbar.

CHAPTER 7
SUMMARY AND CONCLUSION

In this dissertation, the structure and properties of ZnO based nanowires and thin films were examined.

Single crystal ZnO nanowire growth was achieved using catalyst-driven molecular beam epitaxy. The nanowire growth was realized via selective nucleation on Ag films or islands deposited on a SiO_2-terminated Si substrate surface. Growth occurred at substrate temperatures on the order of 300–500 °C. The nanowires were uniform cylinders, exhibiting diameters of 15–40 nm and lengths in excess of 1 μm. With this approach, nanowire placement can be predefined via location of metal catalyst islands or particles. This, coupled with the relatively low growth temperatures needed, suggests that ZnO nanowires could be integrated on device platforms for numerous applications, including chemical sensors and nanoelectronics.

Growth and characterization of (Zn, Mg)O nanowires were studied as a function of Zn and Mg flux via molecular beam epitaxy. Nanowires were grown on Ag-coated Si substrates. As the Mg pressure increases, three different types of nanowires were observed. At a lower Mg pressure of 2×10^{-7} mbar, the radial heterostructured nanowires consist of a single crystal, Zn-rich $Zn_{1-x}Mg_xO$ (x < 0.02) core having a hexagonal wurtzite structure encased by an epitaxial $Zn_{1-y}Mg_yO$ (y >>0.02) sheath having the same hexagonal wurtzite structure. At a higher Mg pressure of 4×10^{-7} mbar, the radial

148

heterostructured nanowires consist of single crystal ZnO with a hexagonal wurzite structure surrounded by a (Mg,Zn)O sheath with a cubic rock salt structure. At much higher Mg pressure of 8×10^{-7} mbar, the nanowires are only MgO having cubic rock salt structure. Zn exists in MgO nanowire as a solid solution while the cubic rock salt structure is maintained. The growth orientation of MgO is in <100> direction. The cored structure forms spontaneously under constant flux due to a bimodal growth mechanism in which the core forms via bulk-like vapor-liquid-solid growth, while the outer sheath grows as a heteroepitaxial layer.

The effect of phosphorus doping on transport properties in ZnO films was examined. Phosphorus doping yields enhanced n-type behavior in as-deposited films, indicating the formation of shallow donor states. Annealing in 100 mTorr of oxygen led to the conversion of heavily n-type behavior in as-deposited films to semi-insulating behavior. For the annealed film, these results may reflect phosphorus substitution on the O site. Additional spectroscopic measurements will be needed in order to better delineate the nature and location of the deep level.

The characteristics of device structures that employ phosphorus-doped (Zn,Mg)O have been examined in a effort to delineate the carrier type behavior in this material. Platinum-coated Si was used as the substrate, with Pt serving as the bottom electrode in the device structures. For the M-I-S diode structures, the P-doped (Zn,Mg)O annealing step is followed by the deposition of a gate oxide. In this case, the gate oxide selected was $(Ce,Tb)MgAl_{11}O_{19}$. For the p-n junction devices, an undoped ZnO film was deposited on the P-doped (Zn,Mg)O film at a temperature of 400 ˚C in an oxygen ambient of 20 mTorr. The capacitance-voltage properties of metal/insulator/P-doped

(Zn,Mg)O diode structures were measured and found to exhibit a polarity consistent with the P-doped (Zn,Mg)O layer being p-type. In addition, thin-film junctions comprising n-type ZnO and P-doped (Zn,Mg)O display asymmetric I-V characteristics that are consistent with the formation of a p-n junction at the interface. Although Hall measurements of the P-doped (Zn,Mg)O thin films yielded an indeterminate Hall sign due to a small carrier mobility, these results are consistent with previous reports that phosphorus can yield an acceptor state and p-type behavior in ZnO materials.

The photo-response of ZnO doped with phosphorus was investigated. A correlation between near band-edge emission and carrier density is observed. This is similar to results found for ZnO in which the carrier density is increased with annealing in a reducing ambient. Upon annealing in an oxidizing environment, the near band-edge emission decreases for both the undoped and phosphorus doped ZnO films. This attributed to radiative transitions involving acceptor levels deep in the gap. The phosphorus doping, combined with annealing, leads to an enhanced photoconductivity response.

Phosphorus doped ZnO films grown by pulsed laser deposition on c-plane Al_2O_3 substrates were annealed at temperatures up to 600 °C to produce n-type carrier concentrations in the range 7.5 x10^{15}-1.5x10^{20} cm^{-3}. After high dose (3x10^{16} cm^{-2}) Mn implantation and subsequent annealing at 600 °C, all the films show n-type carrier concentrations in the range 2-5 x10^{20} cm^{-3} and room temperature hysteresis in magnetization loops. The saturation magnetization and coercivity of the implanted single-phase films were both strong functions of the initial anneal temperature, suggesting that

carrier concentration alone cannot account for the magnetic properties of ZnO:Mn and factors such as crystalline quality and residual defects play a role.

The growth rate of epitaxial ZnO films was studied as a function of RF power. For ZnO thin films, grown on c-plane Al_2O_3 at 400°C and at an oxygen pressure of 5×10^{-5} mbar and a Zn pressure of 1×10^{-6} mbar, the growth rate increases with RF power up to 400W and then saturates at a value of approximately 32 Å/nm. According to SEM images, carrier density, and resistivity, RF power of 300W is selected for the growth of ZnO film. The resistivity decreases and the carrier concentration increases as Zn pressure increases with an oxygen pressure of 5×10^{-5} mbar. The increase of Zn interstitials (Zn_i) in ZnO with Zn pressure, mainly increases the resistivity and carrier density.

Photoluminescence spectra display a strong near band-edge (NBE) emission and a weak deep-level (DL) emission. The room-temperature photoluminescence spectra were studied for ZnO grown at 500°C with an oxygen pressure of 5×10^{-5} mbar as a function of Zn pressures. The near band-edge emission decreases and the deep-level emission increases as Zn pressure decreases during the growth of ZnO. The deep level emission peak shifts from green (2.24 eV) to yellow (2.04 eV) with a decrease of Zn pressure, while the near band-edge emission peak position is constant. It seems that the green in deep-level emission is related to a donor-deep acceptor(Zn vacancy, V_{Zn}^-) transition and the yellow to a donor-deep acceptor(oxygen vacancy, O_i^-) transition. From the yellow shifts of deep level emission, it appears that the concentration of oxygen interstitials (O_i^-) becomes larger than that of Zn vacancies (V_{Zn}^-) with a decrease of Zn pressure during the growth of ZnO. In order to investigate a relationship between deep-level emission and the crystallinity of ZnO, four-circle x-ray diffraction is measured. In the case of ZnO grown

by MBE using atomic oxygen source, it seems that crystallinity is not much related to the deep-level emission.

The growth of ZnO thin film on c-plane Al_2O_3 via molecular beam epitaxy using ozone as an oxygen source was investigated. Epitaxial growth required high Zn and O_3/O_2 flux rates, with a limited temperature range for film growth. The ZnO films grown using ozone (O_3/O_2) were highly conductive and n-type.

REFERENCES

1. Z. K. Tang, G. K. L. Wong, P. Yu, M. Kawasaki, A. Ohtomo, H. Koinuma, and Y. Segawa, Appl. Phys. Lett. **72**, 3270 (1998).

2. D. M. Bagnall, Y. F. Chen, Z. Zhu, T. Tao, S. Koyama, M. Y. Shen, and T. Goto, Appl. Phys. Lett. **70**, 2230 (1997).

3. S. Major, S. Kumar, M. Bhatnagar, and K. L. Chopra, Appl. Phys. Lett. **49**, 394 (1986).

4. S. Masuda, K. Kitamura, Y. Okumura, S. Miyatake, H. Tabata and T. Kawai, J. Appl. Phys. **93**, 1624 (2003).

5. P. F. Carcia, R. S. McLean, M. H. Reilly, and G. Nunes Jr., Appl. Phys. Lett. **82**, 1117 (2003).

6. K. Minegishi, Y. Koiwai, Y. Kikuchi, K. Yano, M. Kasuga and A. Shimizu, Jpn. J. Appl. Phys. **36**, L1453 (1997).

7. X. Wang, S. Yang, J. Wang, M. Li, X. Jiang, G. Du, X. Liu and R. P. H. Chang, J. of Cryst Growth **226**, 123 (2001).

8. K. Nakahara, H. Takasu and P. Fons, Appl. Phys. Lett. **79**, 4139 (2001).

9. K. Iwata, P. Fons, A. Yamada, K. Matsubara and S. Niki, J. Cryst. Growth **209**, 526 (2000).

10. D. C. Look, D. C. Reynolds, C. W. Litton, R. L. Jones, D. B. Eason, and G. Cantwell, Appl. Phys. Lett. **81**, 1830 (2002).

11. M. Joseph, H. Tabata, H. Saeki, K. Ueda, and T. Kawai, Physica B **302-303**, 140 (2001).

12. Frans C.M. Van De Pol, Ceramic Bulletin **69**, 1959 (1990).

13. H. Nishiyama, N. Saito, H. Chou, K. Sato and Y. Inoue, Surface Science **433-435**, 525-528 (1999).

14. Y. P. Wang, W. I. Lee, and T. Y. Tseng, Appl. Phys. Lett. **69**, 1807 (1996).

15. W. P. Kang, and C. K. Kim, Sensors and Actuators B **13-14**, 682 (1993).

16. F. Paraguay D., M. Miki-Yoshida, J. Morales, J. Solis and W. Estrada L. Thin Solid Films **373**, 137 (2000).

17. C. R. Wuethrich, C. A. P. Muller, G. R. Fox and H. G. Limberger, Sensors and Actuators A **66**, 114 (1998).

18. Http://www.semiconductors.co.uk/propiivi5410.htm

19. S. C. Binari and H. B. Dietrich, "III-V Nitride Electronic Devices," in *Optoelectronic Properties of Semiconductors and Superlattices*: *Vol. 2. GaN and Related Materials*, M.O. Manashreh, series ed., and Stephen J. Pearton, ed., Gordon and Breach Publishers, Amsterdam, The Netherlands, 513 (1997).

20. H. Hosono, H. Ohta, K. Hayashi, M. Orita, and M. Hirano, J. of crystal growth 237-239, 496 (2002)

21. C. Y. Kwong, A. B. Djurisic, P.C. Chui, L. S. M. Lam and W. K. Applied physics. A **77**, 555 (2003)

22. R.G. Gordon, MRS Bulletin **25**, 52 (2000)

23. K. Nakahara, H. Takasu, P. Fons, K. Iwata, A. Yamada, K. Matsubara, R. Hunger and S. Niki, J. of Crystal Growth **227-228**, 923 (2001).

24. H. Sankur and J. T. Cheung, J. Vacuum Sci. Technol. A **1 [4]**, 1806 (1983).

25. Y. Yan, S. B. Zhang, and S. T. Pantelides, Phys. Rev. Lett. **6**, 5723 (2001).

26. K. Iwata, P. Fons, S. Niki, A. Yamada, K Matsubaru, K. Nakahara, and H. Tkasu, Phys. Stat. Sol. (a) **180**, 287 (2000).

27. T. Minami, MRS Bulletin **25**, 38 (2000).

28. F. Capasso, Science **235**, 172 (1987).

29. E. R. Segnit and A. E. Holland, J. Am.Ceram. Soc. **48[1]**, 412 (1965).

30. A. Ohtomo, M. Kawasaki, T. Koida, K. Masubuchi, H. Koinuma, Y. Sakurai, Y. Yoshida, T. Yasuda, and Y. Segawa, Appl. Phys. Lett. **72**, 2466 (1998).

31. S. Choopun, R. D. Vispute, W. Yang, R. P. Sharma, and T. Venkatesan, Appl. Phys. Lett. **80**, 1529 (1998).

32. G. Timp, *Nanotechnology*, Springer, New York (1998).

33. H. Z. Zhang, Y. C. Kong, Y. Z. Wang, X. Du, Z. G. Bai, J. J. Wang, D. P. Yu, Y. Ding, Q. L. Hang, and S. Q. Feng, Solid State Commun. **109**, 677 (1999).

34. M. J. Zheng, L. D. Zhang, G. H. Li, X. Y. Zhang, and X. F. Wang, Appl. Phys. Lett. **79**, 839 (2001).

35. N. I Kovtyukhova, B. R. Martin, J. K. N. Mbindyo, P. A. Smith, B. Razavi, T. S. Mayer, and T. E. Mallouk, J. Phys. Chem. B **105**, 8762 (2001).

36. Z. W. Pan, Z. R. Dai, and Z. L. Wang, Science **291**, 1947 (2001).

37. T. Hirata, N. Satake, G.-H. Jeong, T. Kato, R. Hatakeyama, K. Motomiya, and K. Tohji, Appl. Phys. Lett. **83**, 1119 (2003).

38. J. Gavillet, A. Loiseau, C. Journet, F. Willaime, F. Ducastelle, and J.-C. Charlier, Phys. Rev. Lett. **87**,275504 (2001).

39. G. T. Kim, J. Muster, V. Krstic, J. G. Park, Y. W. Park, S. Roth, and M. Burghard, Appl. Phys. Lett. **76**, 1875 (2000).

40. N. J. Stone and H. Ahmed, Appl. Phys. Lett. **73**, 2134 (1998).

41. Y. Cui, Q. Wei, H. Park, and C. M. Lieber, Science **293**, 1289 (2001).

42. M. H. Huang, S. Mao, H. Feick, H. Yan, Y. Wu, H. Kind, E. Weber, R. Russo, and P. Yang, Science **292**, 1897 (2001).

43. Y. Wu and P. Yang, Chem. Mater. **12**, 605 (2000).

44. A. M. Morales and C. M. Lieber, Science **279**, 208 (1998).

45. W. S. Shi, Y. F. Zheng, N. Wang, C. S. Lee, and S. T. Lee, J. Vac. Sci. Technol. B **19**, 1115 (2001).

46. R. Landauer, J. Rev. De. **1**, 223 (1957).

47. J. A. Torres and J. I. Sanez, Phys. Rev. Lett. **77**, 2245 (1996).

48. K. schwab, E. A. Henriksen, J. M. Worlock, and M. L. Roukes, Nature **404**, 974 (2000).

49. R. S. Wagner and W.C. Ellis, Appl. Phys. Lett. **4**. 889 (1964).

50. X. Duan, and C. M. Lieber, Adv. Mater. **12**, 298 (2000).

51. M. H. Huang, Y. Wu, H. Feick, N. Tran, E. Weber, and P. Yang, Adv. Mater. **13**, 113 (2001).

52. S. Bhunia, T. Kawamura, Y. Watanabe, S. Fujikawa and K. Tokushima, Appl. Phys. Lett. **83**, 3371 (2003).

53. M. Gudiksen, L. J. Lauhon, J. Wang, D. C. Smith and C. M. Lieber, Nature **417**, 617 (2002).

54. A. Thess, R. Lee, P. Nikolaev, H. Dai, P. Petit, J. Robert, C. Xu, Y. Lee, S. Kim, A. G. Rinzler, D.T. Colbert, G. E. Scuseria, D. Tománek, J. E. Fischer, and R. E. Smalley, Science **273**, 483 (1996).

55. C. Journet, W. K. Maser, P. Bernier, A. Loiseau, M. Chapelle, S. Lefrant, P. Deniard, R. Lee and J. E. Fisher, Nature **388**, 756 (1997).

56. Y. C. Kong, D. P. Yu, B. Zhang, W. Fang, and S. Q. Feng, Appl. Phys. Lett. **78**, 407 (2001).

57. J. Y. Li, X. L. Chen, H. Li, M. He and Z. Y. Qiao, J. of Crystal Growth **233**, 5 (2001).

58. S. Y. Li, C.Y. Lee and T. Y. Tseng, J. of Crystal Growth **247**, 357 (2003).

59. Y. Li, G. W. Meng, L. D. Zhang, and F. Phillip, Appl. Phys. Lett. **76**, 2011 (2000).

60. J. C. Hulteen and C. R. Martin, J. Mater. Chem. **7**, 1075 (1997).

61. S. Y. Li, C.Y. Lee and T.Y. Tseng, J. of Crystal Growth **247**, 357 (2003).

62. C. J. Lee, T. J. Lee, S. C. Lyu, Y. Zhang, H. Ruh and H. J. Lee, Appl. Phys. Lett. **81**, 3648 (2002).

63. P. Fons, K. Iwata, A. Yamada, K. Matsubara, S. Niki, K. Nakahara, T. Tanabe, and H. Takasu, Appl. Phys. Lett. **77**, 1801 (2000).

64. H. Tee Ng, B. Chen, J. Li, J. Han, M. Meyyappan, J. Wu, S. X. Li, and E. E. Haller , Appl. Phys. Lett. **82**, 2023 (2003).

65. Z. W. Pan, Z. R. Dai, and Z. L. Wang, Science **291**, 1947 (2001).

66. J. H. Chang, M. W. Cho, H. M. Wang, H. Wenisch, T. Hanada, T. Yao, K. Sato, and O. Oda, Appl. Phys. Lett. **77**, 1256 (2000).

67. S. J. Pearton, *Processing of Wide Band Gap Semiconductors*, William Andrew Publishing, New York (2000).

68. A. Zunger, Appl. Phys. Lett. **83**, 57 (2003).

69. T. Yamamoto and H. Katayama-Yoshida, Jpn. J. Appl. Phys. **38**, L166 (1999).

70. T. Yamamoto, Thin solid Films, Available online 3 October (2002).

71. B. Zhang, S.-H. Wei, and A. Zunger, Phys. Rev. Lett. **84**, 1232 (2000).

72. G. Heiland, E. Mollwo, and F. Stöckmann, in Solid State Physics, edited by F. Seitz and D. Turnbull, **8**, 91 (Academic, New York, 1959).

73. K. Vanheusden, C. H. Seager, W. L. Warren, D. R. Tallant, and J. A. Voigt, Appl. Phys. Lett. **68**, 403 (1996).

74. D. C. Look, J. W. Hemsky, and J. R. Sizelove, Phys. Rev. Lett. **82**, 2552 (1999).

75. J. Chevallier, Mater. Sci. Eng. B **71**, 62 (1998).

76. Chris G. Van de Walle, Phys. Rev. Lett. **85**, 1012 (2000).

77. Y. R. Ryu, S. Zhu, D. C. Look, J. M. Wrobel, H. M. Jeong and H. W. White, J. of Crystal Growth **216**, 330 (2000).

78. Y.-D. Ko, J. Jung, K. H. Bang, M. C. Park, K. S. Huh, J. M. Myoung and I. G. Yun, Applied Surface Science **202**, 266 (2002).

79. Y. Yan, S. B. Zhang, S. T. Pantelides, Phys. Rev. Lett. **6**, 5723 (2001).

80. K. Sakurai, D. Iwata, S. Fujita, and S. Fujita, Jpn. J. Appl. Phys. Part 1 **38**, 2606 (1999).

81. M. A. L. Johnson, S. Fujita, W. H. Rowland, Jr., W. C. Hughes, J. W. Cook, Jr., and J. F. Schetzina, J. Electron. Mater. **25**, 855 (1996).

82. Y. C. Kong, D. P. Yu, B. Zhang, W. Fang, and S. Q. Feng, Appl. Phys. Lett. **78**, 407 (2001).

83. K. Vanheusden, W. L. Warren, C. H. Seager, D. K. Tallant, J. A. Voigt, and B. E. Gnade, J. Appl. Phys. **79**, 7983 (1996).

84. S. T. Lee, N. Wang, and C. S. Lee, Mater. Sci. Eng., A **286**, 16 (2000).

85. C. H. Liang, G. W. Meng, G. Z. Wang, Y. W. Wang, L. D. Zhang, and S. Y. Zhang, Appl. Phys. Lett. **78**, 3202 (2001).

86. W. P. Vellinga and J. Th. M. E. Hossen, Acta. Mater. **45**, 933 (1997).

87. L. J. Lauhon, M. S. Gudiksen, D. Wang, and C. M. Lieber, Nature **420**, 57 (2002).

88. J. F. Sarver, F. L. Katnack, and F. A. Hummel, J. Electrochem. Soc. **106**, 960 (1959).

89. D. C. Reynolds, C. W. Litton, and T. C. Collins, Phys. Rev. **140**, A1726 (1965).

90. M. Haupt, A. Ladenburger, R. Sauer, K. Thonke, R. Glass, W. Roos, J. P. Spatz, H. Rauscher, S. Riethmüller, and M. Möller, J. Appl. Phys. **93**, 6252 (2003).

91. V. S. Dneprovskii, E. A. Zhukov, N. Yu. Markova, E. A. Mulyarov, K. A. Chernoutsan, and O. A. Shalygina, Phys. of the Solid State **42**, 544 (2000).

92. A. Ohtomo, M. Kawasaki, I. Ohkubo, H. Koinuma, T. Yasuda, and Y. Segawa, Appl. Phys. Lett. **75**, 980 (1999).

93. M. S. Gudiksen, J. Wang, and C. M. Lieber, J. Phys. Chem. B **106**, 2036 (2002).

94. E. M. Wong and P. C. Searson, Appl. Phys. Lett. **74**, 2939 (1999).

95. Y. W. Heo, V. Varadarajan, M. Kaufman, K. Kim, D. P. Norton, F. Ren, and P. H. Fleming, Appl. Phys. Lett. **81**, 3046 (2002).

96. A. K. Sharma, J. Narayan, J. F. Muth, C. W. Teng, C. Jin, A. Kvit, R. M. Kolbas, and O. W. Holland, Appl. Phys. Lett. **75**, 3327 (1999).

97. A. Ohtomo, M. Kawasaki, T. Koida, K. Masubuchi, H. Koinuma, Y. Sakurai, Y. Yoshida, T. Yasuda, and Y. Segawa, Appl. Phys. Lett. **72**, 2466 (1998).

98. D. C. Look, D. C. Reynolds, C. W. Litton, R. L. Jones, D. B. Eason, and G. Cantwell, Appl. Phys. Lett. **81**, 1830 (2002).

99. T. Aoki, Y. Hatanaka, and D. C. Look, Appl. Phys. Lett. **76**, 3257 (2000).

100. C. H. Park, S. B. Zhang, Su-Huai Wei, Phys. Rev. B **66**, 073202 (2002).

101. R. Franke, T. Chasse, P. Streubel, A. Meisel: J. Electron Spectrosc. Relat. Phenom. **56**, 381 (1991).

102. R. Gresch, W. Mueller-Warmuth, H. Dutz: J. Non-Cryst. Solids **34**, 127 (1970).

103. K. Ip, M. E. Overberg, Y. W. Heo, D. P. Norton, S. J. Pearton, S. O. Kucheyev, C. Jagadish, J. S. Williams, R. G. Wilson, and J. M. Zavada, Appl. Phys. Lett. **81**, 3996 (2002).

104. A. B. M. Almamun Ashrafi, I. Suemune, H. Kumano, and S. Tanaka, Jpn. J. Appl. Phys. 41, L1281 (2002).

105. E. H. Nicollian and J. R. Brews, "MOS (Metal Oxide Semiconductor) Physics and Technology," (J. Wiley and Sons, New York, 1982).

106. J. M. Shah, Y.-L. Li, Th. Gessmann, and E. F. Schubert, J. Appl. Phys. 94, 2627 (2003).

107. R. L. Hoffman, J. F. Wager, M. K. Jayaraj, and J. Tate, J. Appl. Phys. 90, 5763 (2001).

108. V. A. Dmitriev, MRS Internet J. Nitride Semicond. Res. 1, 29 (1996).

109. H. C. Casey, Jr., J. Muth, S. Krishnankutty, and J. M. Zavada, Appl. Phys. Lett. 68, 2867 (1996).

110. P. Perlin, M. Osinski, P. G. Eliseev, V. A. Smagley, J. Mu, M. Banas, and P. Sortori, Appl. Phys. Lett. 69, 1680 (1996).

111. A. Tiwari, C. Jin, D. Kumar, J. Narayan, Appl. Phys. Lett., 83, 1773 (2003).

112. H. Ohta, M. Hirano, K. Nakahara, H. Murata, T. Anabe, M. Kamiya, T. Kamiya, and H. Hosono, Appl. Phys. Lett. 83, 1029 (2003).

113. D.-K. Hwang, K.-H. Bang, M.-C. Jeong, and J.-M. Myoung, J. Crystal Growth 254, 449 (2003).

114. H. Ohta, H. Mizoguchi, M. Hirano, S. Narushima, T. Kamiya, and H. Hosono, Appl. Phys. Lett. 82, 823 (2003).

115. H. Hosono, H. Ohta, K. Hayashi, M. Orita, and M. Hirano, J. Crystal Growth 237-239, 496 (2002).

116. A. N. Gruzintsev, V. T. Volkov, I. I. Khodos, T. V. NiKiforava, and M. N. Koval'schuk, Russian Microelectronics **31**, 200 (2002) .

117. D. H. Zhang and D. E. Brodie, Thin Solid Films **238**, 95 (1994).

118. O. Agyeman, C. Zu, W. Shi, Z. Zheng, and M. Suzuki, Jpn. J. Appl. Phys. **41**, 666 (2002).

119. N. Ohashi, T. Ishigaki, N. Okada, T. Sekiguchi, I. Sakaguchi, and H. Haneda, Appl. Phys. Lett. **80**, 2869 (2002).

120. W. S. Shi, O. Agyeman, and C. N. Xu, J. Appl. Phys. **91**, 5640 (2002).

121. F. H. Leiter, H. R. Alves, A. Hofstaetter, D. H. Hofman, and B. K. Meyer, Phys. Stat. Sol. B **226**, R4 (2001).

122. X. L. Wu, G. G. Siu, C. L. Fu, and H. C. Ong, Appl. Phys. Lett. **78**, 2285 (2001).

123. K. Vanheusden, C. H. Seager, W. L. Warren, D. R. Tallant, and J. A. Voigt, Appl. Phys. Lett. **68**, 403 (1996).

124. S. A. Studenikin and M. Cocivera, J. phys. Appl. **91**, 5060 (2002).

125. A. Ortiz, C. Falcony, J. Hernandez, m. Garcia, and J. C. Alonso, Thin Solid Films **293**, 103 (1997).

126. A. N. Georgobiani, T. V. Butkhuzi, O. V. Aleksandrov, and T.G. Khulordava, Sov. Phy. Lebedov Inst. Rept. **9**, 53 (1984).

127. Y. Takahashi, M. Kanamori, A. Kondon, H. Minours, and Y. Ohya, Jpn. J. Appl. Phys. **33**, 6611 (1994)

128. P. Sharma, m. Abhai, and K. Sreenivas, Appl. Phys. **84**, 553 (2002).

129. S. A. Studenikin, N. Golego, and M. Cocivera, J. Appl. Phys. **84**, 5001 (1998).

130. J. W. Tomm, B. Ulrich, X. G. Qiu, Y. Segawa, A. Ohtomo, M. Kawasaki, and H. Koinuma, J. Appl. Phys. **87**, 1844 (2000)

131. H. Ohno, A. Shen, F. Matsukura, A. Oiwa, A. Endo, S. Katsumoto, and Y. Iye, Appl. Phys. Lett. **69**, 363-5 (1996).

132. M. Berciu and R. N. Bhatt, Phys. Rev. Lett. **87**, 107203.1-4 (2001).

133. M. Mayr, G. Alvarez, and E. Dagotto, Phys. Rev. B **65**, 241202 (2002).

134. S. Das Sarma, E. H. Hwang, and A. Kaminski, Phys. Rev. B **67**, 155201-155201-16 (2003).

135. N.Theodoropoulou,G.P.Berera,V.Misra,P.LeCalir,J.Philip,J.S.Moodera,B.Satapi and T.Som (to be published).

136. K. Haga, M. Kamidaira, Y. Kashiwaba, T. Sekiguchi and H. Watanabe, J. of Crystal Growth **214**, 77 (2000).

137. R. Ondo-Ndong, G. Ferblantier, M. Al Kalfioui, A. Boyer and A. Foucaran, J. of Crystal Growth **255**, 130 (2003).

138. Y. W. Heo, S. J. Park, K. Ip, S. J. Pearton, and D. P. Norton, Appl. Phys. Lett. **83**, 1128 (2003).

139. K. Sakurai, M. Kanehiro, K. Nakahara, T. Tanabe, S. Fujita and S. Fujita, J. of Crystal Growth, **214-215**, 92 (2000).

140. J. B. Kim, K. Chakrabarti, J. H. Lee, K.-Y. Oh and C. Lee, Materials Chemistry and Physics **78**, 733 (2003).

141. H.-J. Egelhaaf, D. Oelkrug, J. of Crytal Growth **161**, 190 (1996).

142. D. C. Reynolds, D.C. Look, and B. Jogai, J. Appl. Phys. **89**, 6189 (2001).

143. P. S. Xu, Y.M. Sun, C. S. Shi, G. F. Q. Xu, and H. B. Pan, Nuclear instruments and Methods in Physics Research B **199**, 286 (2003).

144. B. Lin, Z. Fu, and Y. Jia, Appl. Phys. Lett. **79**, 943 (2001).

145. X. L. Wu, G.G. Siu, C.L. Fu, and H.C. Ong, Appl. Phys. Lett. **78**, 2285 (2001).

146. S. B. Zhang, S.-H. Wei, and A. Zunger, Physical Review B **63**, 075205 (2001).

147. D. C. Look, Materials Science and Engineering B **80**, 383 (2201).

148. S. Yuming, X. Pengshou, S. Chaoshu, X. Faqiang, P. Haibin and L. Erdong, J. of Electron Spectroscopy and Related Phenomena, **114-116**, 1123 (2001).

149. P. Kasai, Phts, Rev. **130**, 989 (1963).

150. D. M. Bagnall, Y. F. Chen, M. Y. Shen, Z. Zhu, T. Goto, and T. Yao, J. of Crystal Growth, **184/185**, 605 (1998)

151. D. C. Reynolds, D. C. Look, and B. Jogai, C. W. Litton, T. C. Collins, W. Harsch and G. Cantwell, Phys.Rev. B **57**, 12151 (1998).

152. Y. Chen, D. M. Bagnall, H. J. Koh, K. T. Park, K. Hiraga, Z. Zhu, and T. Yao, J. Appl. Phys. **84**, 3912 (1998).

153. W. Gopel, J. Vac.Sci. Technol. **16**, 1229 (1979).

154. X. L. Wu, G.G. Siu, C.L. Fu, and H.C. Ong, Appl. Phys. Lett. **78**, 2285 (2001).

155. M. Liu, A. H. Kitai and P. Mascher, J. of Luminescence **54**, 35 (1992).

156. A. Mills, S.-K. Lee and A. Lepre, J. of Photochemistry and Photobiology A **155**, 199 (2003).

BIOGRAPHICAL SKETCH

Young-Woo Heo was born in the Republic of Korea on July 18, 1968. He received his Bachelor of Engineering in inorganic materials engineering and Graduate Summa-cum-laude in the College of Engineering from Kyungpook National University in Taegu, Korea in 1994. He attended Kyungpook National University in 1994 to his graduation with Mater of Engineering in inorganic materials engineering in February of 1996. His research area for master's degree was focused on microstructures and electrical properties of semiconducting $BaTiO_3$ ceramics by boron containing Liquid-phase Sintering.

After receiving the degree of master, he had a 4 and half year working experience in the development of phosphors for Plasma Display Panel as a researcher in LG Chemical Research Park Ltd.. In August of 2000, he entered at University of Florida in the department of materials science and engineering to pursue his Ph. D. He is researching in the growth and characterization of ZnO based nanowires and thin films under the supervision of Dr. David P. Norton.
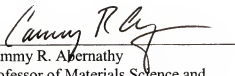
He is author of 20 articles in journals, conference proceedings, including 7 in Applied Physics Letters. He is being considered for inclusion in the upcoming 59th Edition of Who's Who in America, which is scheduled for publication in October 2004.

I certify that I have read this study and that in my opinion it conforms to acceptable standards of scholarly presentation and is fully adequate, in scope and quality, as a dissertation for the degree of Doctor of Philosophy.

David P. Norton, Chairman
Professor of Materials Science and
    Engineering

I certify that I have read this study and that in my opinion it conforms to acceptable standards of scholarly presentation and is fully adequate, in scope and quality, as a dissertation for the degree of Doctor of Philosophy.

Cammy R. Abernathy
Professor of Materials Science and
    Engineering

I certify that I have read this study and that in my opinion it conforms to acceptable standards of scholarly presentation and is fully adequate, in scope and quality, as a dissertation for the degree of Doctor of Philosophy.
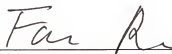
Paul Holloway
Distinguished Professor of Materials
    Science and Engineering

I certify that I have read this study and that in my opinion it conforms to acceptable standards of scholarly presentation and is fully adequate, in scope and quality, as a dissertation for the degree of Doctor of Philosophy.

Michael Kaufman
Professor of Materials Science and
    Engineering

I certify that I have read this study and that in my opinion it conforms to acceptable standards of scholarly presentation and is fully adequate, in scope and quality, as a dissertation for the degree of Doctor of Philosophy.

Fan Ren
Professor of Chemical Engineering

This dissertation was submitted to the Graduate Faculty of the College of Engineering and to the Graduate School and was accepted as partial fulfillment of the requirements for the degree of Doctor of Philosophy.

December 2003

Pramod P. Khargonekar
Dean, College of Engineering

Winfred M. Phillips
Dean, Graduate School